

NASA TECHNICAL
MEMORANDUM

Report No. 53850

CASE FILE
COPY
N69-38125
~~177-31787~~

OPTICAL PROBING OF SUPERSONIC AERODYNAMIC
TURBULENCE WITH STATISTICAL CORRELATION
PHASE I: FEASIBILITY

By B. H. Funk, Jr. and H. A. Cikanek, Jr.

June 9, 1969

NASA

*George C. Marshall Space Flight Center
Marshall Space Flight Center, Alabama*

TECHNICAL REPORT STANDARD TITLE PAGE

1. REPORT NO. NASA TM X-53850		2. GOVERNMENT ACCESSION NO.		3. RECIPIENT'S CATALOG NO.	
4. TITLE AND SUBTITLE OPTICAL PROBING OF SUPERSONIC AERODYNAMIC TURBULENCE WITH STATISTICAL CORRELATION. PHASE I: FEASIBILITY.				5. REPORT DATE June 9, 1969	
				6. PERFORMING ORGANIZATION CODE	
7. AUTHOR(S) B. H. Funk, Jr.* and H. A. Cikanek, Jr.**				8. PERFORMING ORGANIZATION REPORT #	
9. PERFORMING ORGANIZATION NAME AND ADDRESS * NASA/MSFC, Aero-Astroynamics Laboratory Marshall Space Flight Center, Alabama 35812 ** Northrop Corporation, Huntsville, Alabama				10. WORK UNIT NO.	
				11. CONTRACT OR GRANT NO.	
				13. TYPE OF REPORT & PERIOD COVERED	
12. SPONSORING AGENCY NAME AND ADDRESS				14. SPONSORING AGENCY CODE	
15. SUPPLEMENTARY NOTES					
16. ABSTRACT <p>The feasibility of measuring statistical properties of supersonic aerodynamic turbulence by statistical correlation of signals remotely retrieved by optical probing without the use of tracers is investigated. Theoretical analyses and qualitative experimental results are presented concerning the application of laser quasi-schlieren and laser shadow-correlation remote-sensing systems. Cross-correlation measurements made on-line with parallel and crossed beams are shown and discussed. A "one-shot" statistical correlation concept is introduced and experimentally verified that allows the time-history of the decay of turbulent structures to be computed from a single composite signal and displayed on an oscilloscope while data are being retrieved.</p>					
17. KEY WORDS			18. DISTRIBUTION STATEMENT		
19. SECURITY CLASSIF. (of this report) UNCLASSIFIED		20. SECURITY CLASSIF. (of this page) UNCLASSIFIED		21. NO. OF PAGES 152	22. PRICE

ACKNOWLEDGEMENTS

The authors appreciate the administrative support of Dr. E. D. Geissler, Director of the Aero-Astroynamics Laboratory, and Mr. W. K. Dahm, Chief of the Aerophysics Division. We are grateful to Mr. W. K. Dahm and Dr. F. R. Krause for their technical suggestions and for providing the freedom of approach which was important to this feasibility investigation.

We thank Mr. Richard Felix, Chief of the Experimental Aerodynamics Branch, for allowing us to reactivate and operate the 7"-Bisonic Wind Tunnel and Mr. E. H. Simon for his instruction in the operation and maintenance of this facility. Also, we particularly appreciate the assistance of Messrs. J. Heaman, W. Neighbors, and H. T. Bush with the instrumentation problems.

We especially acknowledge Mr. H. W. Belew, Chief of the Mechanical Design Office, Mr. J. B. Fields, and Mr. R. J. Love for their prompt and efficient design and fabrication of the laser and detector stands, and the two-dimensional wedge model.

We thank Messrs. D. O. Cope, W. O. Long, and G. Kennemer of the Experimental Aerophysics Branch for the multitude of problems they helped solve. Also, we thank Mr. L. Shutzenhofer of the Unsteady Aerophysics Branch for the use of the thin-plate model.

TABLE OF CONTENTS

	<u>Page</u>
SUMMARY	1
I. INTRODUCTION	3
II. BACKGROUND	5
III. DISCUSSION	15
3.1 Remote Sensing by Optical Correlation with Parallel Laser Beams.....	15
3.1.1 Theoretical Description of a Laser Quasi-Schlieren System.....	15
3.1.2 Cross-Correlation of Signals.....	22
3.2 The "One-Shot" Autocorrelation.....	26
3.2.1 The Concept.....	26
3.2.2 Multiple Signals.....	28
3.2.3 Peak Identification.....	31
3.2.4 Interpretation of the Zero Time Lag Peak.....	40
3.2.5 Time Delays and Zoning of the "One-Shot" Autocorrelogram	44
3.2.6 Noise Analysis.....	49
3.3 The "One-Shot" Cross-Correlation.....	51
3.3.1 Statement of the Concept.....	57
3.3.2 Mathematical Development.....	59
3.3.3 Experimental Verification.....	63
3.3.4 Noise Analysis.....	66
3.4 Cross-Beam Discussion.....	74
3.4.1 General Discussion.....	74
3.4.2 Effect of the Boundary Layer on the Test Section Windows	76
3.4.3 Investigation of the Boundary Layer Interaction Zone....	79
3.4.4 Cross-Beam Measurement in Turbulent Wake.....	84
3.4.5 Experimental Results Using a Shadow-Correlation Method..	86
IV. CONCLUSIONS	93
APPENDIX A. DESCRIPTION OF THE BISONIC WIND TUNNEL FACILITY, MODELS, AND INSTRUMENTATION	97
APPENDIX B. COMMENTS ON THE EXPERIMENTAL NOISE STUDY IN MSFC'S 14-INCH TRISONIC WIND TUNNEL (TEST # TWT 395)	127
APPENDIX C. UNKNOWN ANOMALIES IN DATA ACQUISITION SYSTEM	131

DEFINITION OF SYMBOLS

<u>Symbol</u>	<u>Definition</u>
A	cross-correlation area of laser beam
$A(\tau)$ $l \rightarrow m$	"one-shot" autocorrelation
D	detector, photodiode, or diameter of laser beam
d	distance of schlieren knife (razor) edge from outerwall
f	random time history, electronic signal containing random data
F(t)	composite time history
I	absolute instantaneous current output of photodetector power supply (i.e., $I = \bar{I} + i$)
i	instantaneous fluctuating component of I
j	unit increment (usually a unit vector, \hat{j})
L	laser, width of test section ($L = 2\ell$)
ℓ	half-width of the test section ($\ell = L/2$)
M	Mach number
m	number of time histories in a composite time history
N.E.P.	noise equivalent power
n	local index of refraction; "noise-to-signal" ratio
P	number of peaks on "one-shot" auto- or cross-correlation
p	pressure
p-p	peak-to-peak
R	cross-correlation of the fluctuating portion of the signal
$R(\tau)$ $l \rightarrow m$	"one-shot" cross-correlation

DEFINITION OF SYMBOLS (Cont'd)

<u>Symbol</u>	<u>Definition</u>
RC	resistance-capacitance time constant
r	distance from knife-edge to photodiode
s	sensitivity of sensing mode
\vec{s}	Poynting vector (i.e., a vector tangent to the path of the beam with magnitude equal to beam power)
T	total integration time
TEM	transverse electromagnetic mode
t	time
U	speed of disturbances in the axial or x-direction
v	volts
α	Gladstone-Dale constant
β	local instantaneous angular deviation of laser beam measured from a horizontal reference line perpendicular to flow direction
γ	computation time ratio
δ	boundary layer thickness
Δ	increment; beam displacement at knife-edge
μ	micron = 10^{-6}
ξ	beam separation in the flow direction
ρ	density
τ	time delay

SUBSCRIPTS

A,B	upstream and downstream photodetector locations, respectively
a	"one-shot" autocorrelation

DEFINITION OF SYMBOLS (Cont'd)

<u>Symbol</u>	<u>Definition</u>
c	"one-shot" cross-correlation
d	detector or measured at the detector
k	unit increment (i.e., $k = 1, 2, \dots, m$)
m	maximum
n	noise; the nth point in a series of points
p	any particular instant time
p-p	peak-to-peak
s	signal
w	shear layer width; wall
o	initial condition or stagnation condition
1,2	upstream and downstream beam locations, respectively
(∞)	free-stream condition

SUPERSCRIPTS

()'	fluctuating component, minutes of angle
$\overline{(\)}$	time average, vector quantity
(\wedge)	unit vector
< >	expectation value

LIST OF ILLUSTRATIONS

<u>Figure</u>	<u>Title</u>	<u>Page</u>
2-1	Schlieren of Base Flow Field Produced by Wedge Model - Mach 2 Nozzle.....	6
2-2	On-Line Signal from Single Laser Beam Passed Through the Flow Shown in Figure 2-1: (A) Top: Beam at Position 2; (B) Bottom: Beam at Position 1.....	7
2-3	Shadowgraph of Flow Field Generated by the Thin Plate Model Installed in the 7 x 7" BWT With The Mach 2 Nozzle.....	9
2-4	A(Top): Cross-Correlogram from Turbulent Boundary Layer (M = 2.0). B(Bottom): Cross-Correlogram in Free Shear Layer of 2-D Wedge (M = 2.0).....	10
2-5	A(Top): Autocorrelation of Signal One. B(Bottom): Autocorrelation of Signal Two.....	12
2-6	A(Top): Cross-Correlogram from Measurement Made in Wake of Plate. B(Bottom): Cross-Correlogram from Measurement Made in Wake of Plate with One Inch Less Beam Separation than Fig. 2-6A.....	13
3-1	Parallel Beam Arrangement for Remote Acquisition of 7 Inch BWT Data.....	16
3-2	Effect of Knife-Edge on the Deflected Beam.....	20
3-3	The "One-Shot" Autocorrelation for Determination of Convection Speed in Two-Dimensional Turbulence.....	27
3-4	Multiple Pass Parallel Beam Arrangement for the "One-Shot" Autocorrelation.....	29
3-5	A(Top): Schematic of Multiple Beam Arrangement with Separate Detectors. B(Bottom): A "One-Shot" Autocorrelogram with Four Beams.....	30
3-6	A(Top): Autocorrelation of Signal Two vs Time Delay. B(Bottom): Autocorrelation of Signals One and Two vs Time Delay.....	33

LIST OF ILLUSTRATIONS (Continued)

<u>Figure</u>	<u>Title</u>	<u>Page</u>
3-7	Parallel Beam Arrangement with Three Laser Beams - Both Optical and Electrical Addition of Signals are Used.....	37
3-8	"One-Shot" Autocorrelations as Obtained with a Three-Parallel-Beam Arrangement as Shown in Figure 3-7.....	38
3-9	The "One-Shot" Autocorrelation of a Three Time History Composite Showing Decay Envelopes of Turbulent Structure.....	41
3-10	The "One-Shot" Autocorrelation Showing Decay Envelope Using Three Detectors.....	42
3-11	A(Top): "One-Shot" Autocorrelation of Two Signals Added. B(Bottom): Cross-Correlation of Signal One with Two.....	45
3-12	"One-Shot" Autocorrelation with Induced Time Delay	47
3-13	The "One-Shot" Autocorrelation Technique for Determination of Wind Speed and Direction. Top: Schematic. Bottom: Expected Output.....	48
3-14	Noise-to-Signal Ratio of a Composite versus Number of Time Histories Added.....	54
3-15	Increase in Integration Time for a Composite Time History versus Number of Time Histories in Composite.....	56
3-16	Ratio of Computation Time (γ_a) versus Number of Time Histories in Composite (m).....	58
3-17	"One-Shot" Correlation Profiles Measured in a Supersonic Turbulent Boundary Layer.....	64
3-18	"One-Shot" Cross-Correlogram with Three Time Histories in the Composite. Sign of Second Signal Was Negative.....	65

LIST OF ILLUSTRATIONS (Continued)

<u>Figure</u>	<u>Title</u>	<u>Page</u>
3-19	Integration Time Ratio Versus m for a "One-Shot" Cross-Correlation.....	69
3-20	"One-Shot" Auto- and Cross-Correlation Integration Time Comparison.....	73
3-21	Computation Time Comparison of "One-Shot" Cross-Correlation with m Number of Individual Cross-Correlations.....	75
3-22	Schematic of Flow in Test Section (Plain View)....	77
3-23	A(Top): Cross-Correlation of Separated Parallel Beams, 1.03 Inches above Plate. B(Bottom): Cross-Correlation of Separated Parallel Beams, 0.05 Inches above Plate.....	78
3-24	Cross-Correlation Measurements of the Influence of The Interaction Zone Upon Parallel Beam Correlations. A. (Left): Positive Time Lag Range. B. (Right): Negative Time Lag Range.....	80
3-25	A(Top): Schematic of Beam Geometry. B(Bottom): Positive Time Lag Range of Cross-Correlogram Showing Contribution of Interaction Zone.....	82
3-26	A(Top): Schematic of Beam Geometry. B(Bottom): Negative Time Lag Range of Cross-Correlogram for Beam Geometry Shown in Schematic.....	83
3-27	A(Top): Positive Time Lag Range of Cross-Correlogram for Beam Geometry Shown at Top of Fig. 3-26. B(Bottom): Negative Time Lag Range for Same Beam Geometry as in (A).....	85
3-28	A(Top): Schematic of Cross-Beam Geometry. B(Bottom): Cross-Correlogram of Local Signal in The Supersonic Turbulent Wake of the Thin Plate Model.....	87
3-29	Schematic of a Laser Shadow-Correlation System (Side View).....	89

LIST OF ILLUSTRATIONS (Continued)

<u>Figure</u>	<u>Title</u>	<u>Page</u>
3-30	A(Top): Schematic of Beam Geometry. B(Bottom): Shadow-Correlogram of Positive Time Lag Range for Beam Geometry Shown in Schematic (Top).....	90
3-31	A(Top): Schematic of Parallel Beam Geometry (Plain View). B(Bottom): Shadow Cross-Correlogram for Parallel Beam Geometry Shown in Schematic (Top)	92
A-1	MSFC's 7 x 7 Inch BWT, Showing Details of the Test Section and Inlet Diffuser.....	108
A-2	Schematic Drawing of MSFC's 7 x 7" Bionic Wind Tunnel Facility.....	109
A-3	Drawing of the 7 x 7 Inch Bionic Wind Tunnel Showing Major Dimensions.....	110
A-4	Oblique View of the Turbulence Generating Thin Plate Model Installed in the 7 x 7 Inch BWT.....	111
A-5	7 x 7 Inch Bionic Wind Tunnel Control Console.....	112
A-6	Drawing of the Thin Plate Model.....	113
A-7	The Turbulence Generating Thin Plate Model Installed in the 7 x 7 Inch BWT Test Section with a Mach 2 Nozzle.....	114
A-8	Two-Dimensional Turbulence Generating Thin Plate Model.....	115
A-9	Approximate One-Dimensional Flow Field Parameters of the Plate Model Installed in the 7 x 7 Inch Tunnel.....	116
A-10	Two-Dimensional Wedge Model.....	117
A-11	Typical Wiring Diagram for Parallel Beam Remote Sensing Instrument.....	118
A-12	Remote Sensing Instrumentation Installed in MSFC's 7 x 7 Inch Bionic Wind Tunnel.....	119

LIST OF ILLUSTRATIONS (Continued)

<u>Figure</u>	<u>Title</u>	<u>Page</u>
A-13	Remote Sensing Instrumentation "On Line".....	120
A-14	Photodetectors Mounted on Traversing and Elevating Mechanism.....	121
A-15	Photodetector and Mirror Arrangement Used for Cross-Beam Measurement.....	122
A-16	Typical Noise Voltage as a Function of Frequency For the D.C. Power Supply-Photodiode Combination Used in These Tests.....	123
A-17	Laser Source Installed.....	124
A-18	Lasers Mounted for Turbulent Flow Measurements in the BWT by the Cross-Beam Method.....	125
B-1	Cross Beam Test in MSFC's 14" Trisonic Wind Tunnel.....	129

OPTICAL PROBING OF SUPERSONIC AERODYNAMIC TURBULENCE
WITH STATISTICAL CORRELATION

PHASE I: FEASIBILITY

SUMMARY

The theory and qualitative experimental results assessing the feasibility of measuring the statistical properties of supersonic turbulence by statistically correlating signals retrieved remotely with a laser quasi-schlieren system are presented. Also, some data retrieved with a laser shadow-correlation system are shown. Cross-correlograms and auto-correlograms computed on-line show that both of these systems can be used to retrieve flow-related signals sufficient for computing accurate and reproducible "peaks" of correlation. Additive tracers were not introduced because the schlieren and shadow sensing modes were used.

A statistical method for obtaining "one-shot" measurements of the decay history of turbulent structures in a stationary frame of reference is introduced, and results of practical applications of two types of these techniques are shown. The "one-shot" methods represent the only means by which the turbulence decay history can be computed from the same statistical sample of data (i.e., the information can be computed from a single composite signal retrieved during one run of the facility). Theoretical analyses show that these "one-shot" techniques will also yield results in three-dimensional turbulent flow regimes with only minor modification of the beam arrangement (and in some cases with the insertion of time delays between signals) provided signal-to-noise ratios of the raw data time histories are not prohibitive.

The application of parallel-beam geometry was used to increase the signal-to-noise ratio over that of crossed-beam geometry since only qualitative results were sought. Although the crossed-beam geometry should be used for quantitative measurements, the potential use of parallel beams for retrieving quantitative results from a restricted class of flows should be investigated.

Electronically induced time delays are used as a means for (1) zoning the "one-shot" auto- and cross-correlograms, (2) avoiding "peak" overlapping, and (3) identifying the "peak."

With respect to the objectives of this investigation, the qualitative results presented in this report clearly indicate that optical remote probing of supersonic aerodynamic turbulent flows is feasible, without the use of tracers (using statistical correlation). Further, correlation "peaks" computed from signals retrieved with either parallel- or crossed-beams during this investigation were flow-related, very reproducible and readily identifiable.

No discussion of spectra is presented and no attempt is made to experimentally establish what flow properties are measured. These should be the objects of a systematic test directed toward obtaining quantitative results.

I. INTRODUCTION

The majority of fluid flows encountered by the aerodynamicist are turbulent. Because of the complex nature of turbulence, the approach in the subsonic regime has been through the application of statistical methods to data obtained by solid probes inserted into the fluid. However, in supersonic and hypersonic flows, these probes adversely influence the structure of the turbulence. One way to circumvent this difficulty would be to develop a reliable remote sensing tool for measuring the statistical properties of turbulence which would neither affect the flow field nor be adversely affected by it. The laser quasi-schlieren and laser shadow-correlation systems may, perhaps, represent the first generation of such a tool.

The specific purpose of this publication is two-fold: (1) to present the theory and qualitative experimental results verifying the feasibility of optical remote sensing in supersonic turbulent flows employing the statistical correlation technique, and (2) to introduce and document the initial concept, theory, and reduction to practice of a statistical method which permits a "one-shot" measurement of the decay history of turbulent structures from one composite* time history of flow information.

The remote sensing tool used for this investigation employs two laser beams of light ($\lambda = 6328\text{\AA}$) which are retrieved by photodetectors after being influenced by the turbulent field. The time histories of these electrical ac-coupled (fluctuating about a zero mean) signals are amplified and filtered, and statistical correlation methods are used to retrieve the desired flow information (e.g., speed profiles, eddy lifetimes, turbulent length scales, and spectra).

The statistical "one-shot" autocorrelation technique constitutes methods whereby multiple time histories of random data are combined to form a single composite time history and an autocorrelogram is computed from the composite in such a way that a maximum amount of statistical flow information is retrieved with a minimum amount of time, equipment, and cost. The two basic types of "one-shot" correlations are referred to herein as the "one-shot" autocorrelation and the "one-shot" cross-correlation. Theoretical discussions, experimental results, and practical ramifications of these concepts are delineated in the main body of the report.

*The word "composite" is used in this report to imply a time history of random data composed of the algebraic sum of two or more random time histories of data.

The experimental objective of this work was to obtain accurate, reproducible, and readily identifiable correlation peaks with signals remotely retrieved from a supersonic turbulent flow which could be related to the most probable transit time of the disturbances. Previous attempts to obtain correlations in the supersonic regime have been hampered by (1) unknown anomalies in the data acquisition system (see Appendix C), and (2) the influence of facility-induced noise upon the optical system.

The influence of facility-induced noise was reduced by utilization of the 7-inch Bionic Wind Tunnel at MSFC, which operates at a very low noise level. This facility is described in detail in Appendix A.

In addition to reducing the facility-induced noise, the power signal-to-noise ratio of the raw data was increased approximately an order of magnitude by placing the laser beams parallel in the "two-dimensional" turbulent boundary layer on a thin-plate model. The laser beams were parallel to one another in the horizontal plane and normal to the flow direction, thereby increasing the correlated signals between the beams. This correlation technique is analyzed theoretically in section 3.1.

Strong evidence that local information can be successfully retrieved from supersonic turbulent flows by using crossed beams is described in section 3.4.4. Also, the "cross-beam" method was used to investigate the effects the window boundary layers and interaction zones had upon the correlations computed from signals retrieved with parallel beams. It was found that, for the particular model design and thus the flow field, the boundary layers on the test section windows had no significant influence upon the correlograms. However, the interaction of the window and model boundary layers apparently dominated the measurements when the schlieren sensing mode was used in combination with parallel-beam geometry. Nevertheless, this does not affect the conclusions of this investigation because the interaction zones near the windows are supersonic and turbulent. Also, the use of the laser shadow-correlation system reduced the contribution by the interaction zones approximately an order of magnitude. By crossing the beams in the vertical plane, these contributions to the correlograms can be avoided, as shown in section 3.4.4 and 3.4.5.

The correlograms computed during this feasibility investigation represent our first encouraging measurements made in a supersonic turbulent flow with or without tracers and conclude the first phase of the wind tunnel "cross-beam" program. This has been conducted as an MSFC in-house research program with existing equipment and support.

II. BACKGROUND

In November 1968, a test was initiated to determine the feasibility of retrieving signals by optical remote sensing of supersonic turbulent flows for obtaining accurate and reproducible flow-related statistical correlations. The major problem in attempting to retrieve signals by this remote sensing technique has been the low signal-to-noise ratio. One of the major contributors to noise has been the facility-induced (mechanical and acoustical) excitation of the optical system and even of the flow field itself. Since the larger, more advanced type of wind tunnel and air jet facilities being used in previous tests produced high noise levels, identifiable flow-related correlations could not be obtained in the supersonic regime. Because of the relatively small amount of noise produced by the Bisons Wind Tunnel (BWT) facility at Marshall, this facility was selected for this investigation to alleviate the noise problem.

The feasibility test in the BWT was planned in two parts, the objective of part one being to isolate the optical system from facility-induced noise. The possibility for successful isolation looked very promising during the initial investigations. It is difficult to accurately estimate the signal-to-noise ratios obtained in previous facilities since facility-induced noise levels were always larger than flow-related signals, and also because it could not be determined that the correlations of signals were flow-related.

In December 1968, a ratio of flow signal to noise of approximately ten was achieved in the BWT. A single laser beam was passed through the region of interaction of the shock wave and the free shear layer at position 1 perpendicular to the flow (figure 2-1). The resulting signal is shown in figure 2-2B. The laser beam was moved to position 2 in the re-circulatory region of the base. The signal at position 2 is shown in figure 2-2A. All settings on instrumentation were the same for both runs. The experiment was repeated several times with the same results, thus implying that the increase in "signal" was flow-related.* The test objective of part one was achieved.

The test objective of part two of the feasibility test was to obtain reproducible and readily identifiable correlation peaks related to the propagation of disturbances in the "two-dimensional" supersonic turbulent

* Position 1 in figure 2-1 was suspected to be one of considerable activity, because shadowgraphs of such shock wave shear layer interaction regions indicate this.

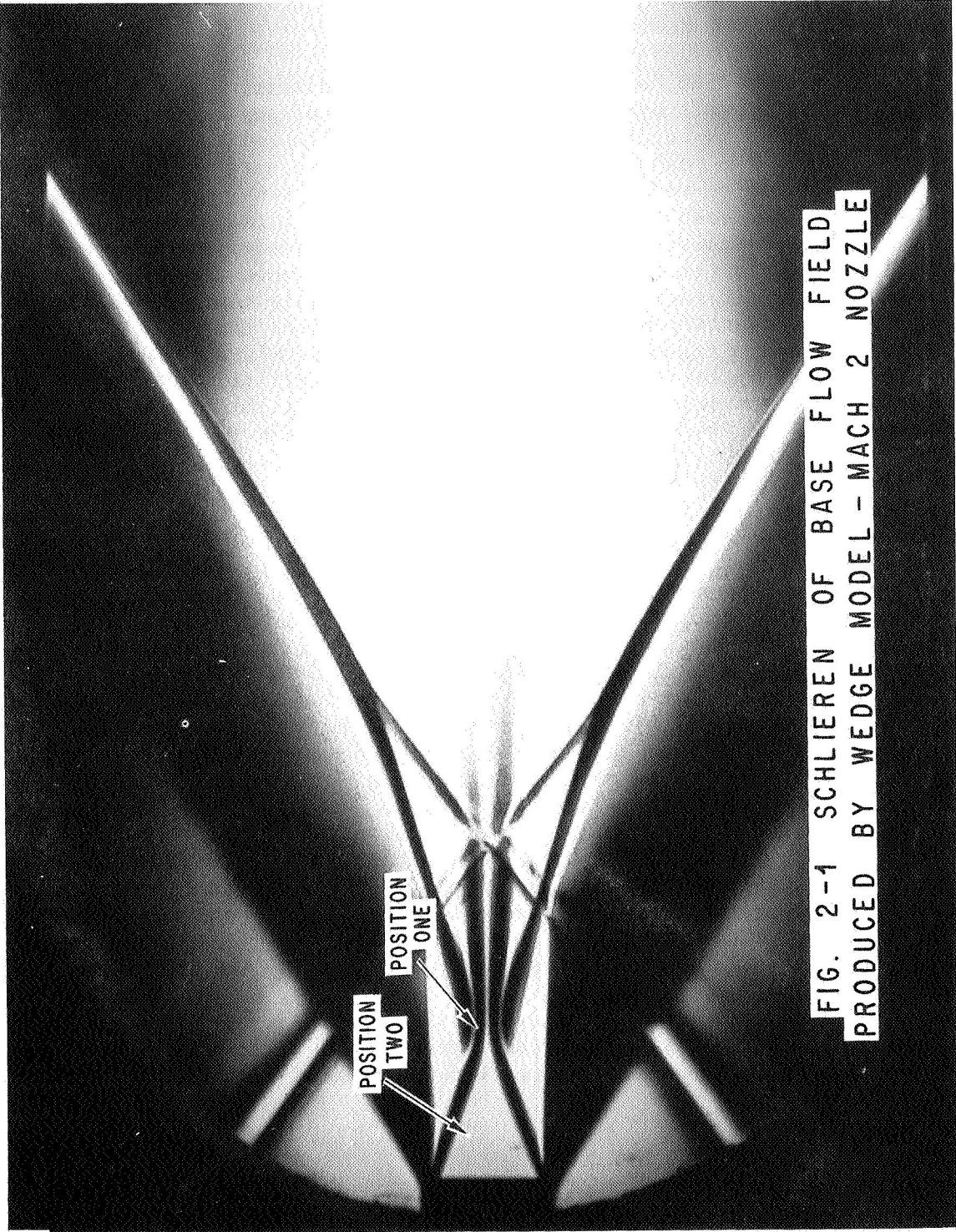


FIG. 2-1 SCHLIEREN OF BASE FLOW FIELD
PRODUCED BY WEDGE MODEL - MACH 2 NOZZLE

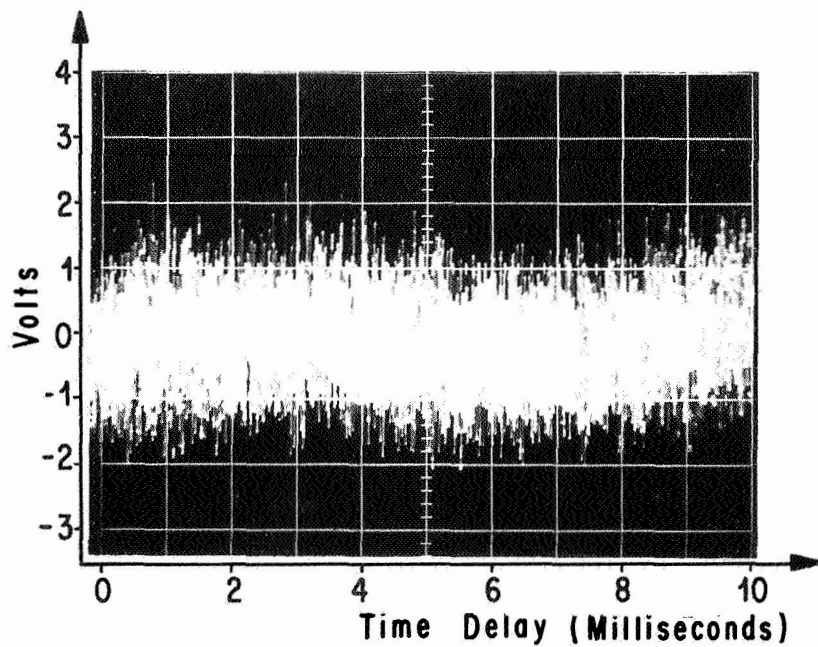
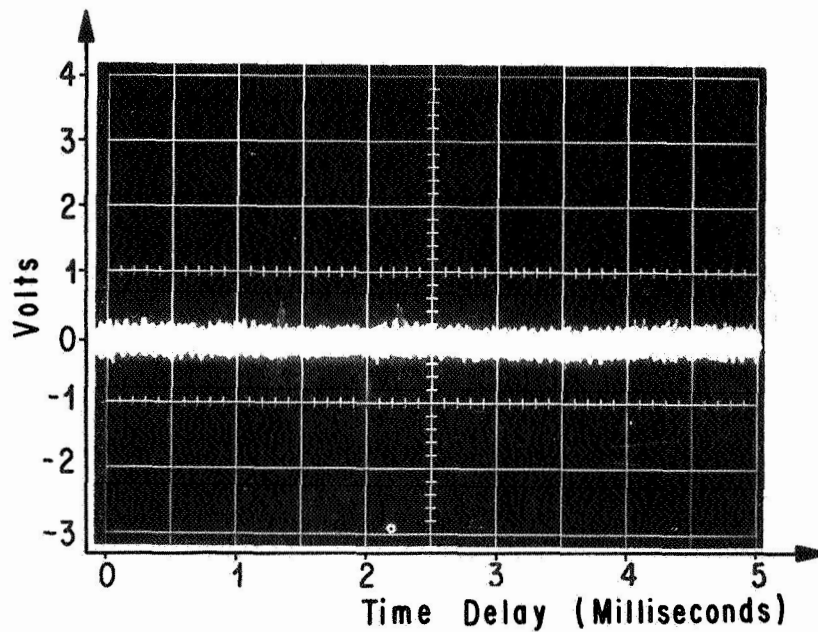


FIG. 2-2 ON-LINE SIGNAL FROM SINGLE LASER BEAM PASSED THROUGH THE FLOW SHOWN IN FIGURE 2-1

- (A) TOP: BEAM AT POSITION 2
- (B) BOTTOM: BEAM AT POSITION 1

boundary layer on a thin plate. An attempt to cross-correlate the signals from two parallel laser beams in the BWT was made during a demonstration on January 22, 1969. The laser beams were separated by 4.5 inches and approximately 1/8 inch above the surface of the plate (see figure 2-3). The signals from the two beams were amplified and cross-correlated in an analog correlator. The resulting cross-correlation, as a function of time delay, was displayed on a scope (figure 2-4A). The maximum correlation occurred at approximately 260 microseconds, which corresponds to a propagation speed of about 1440 fps.* The free-stream speed was approximately 1660 fps. Because of the nature of the run, a great deal of care in locating the beams in the flow was not taken. Therefore, the measurement revealed only that the peak occurred approximately at the expected time delay.

Later investigations clearly showed that this correlation, though relatively weak compared to those computed later, was related to the propagation of turbulence in the boundary layer on the plate and in the interaction zone of the plate and window boundary layers. Further, a considerable amount of water vapor was present which extinguished the laser beams by scattering (schlieren effects were also present). Nevertheless, this very crude measurement represented the first encouraging result from our attempts to retrieve signals from supersonic turbulent flows.

In November 1968 during part one of the feasibility test, an attempt had been made to cross-correlate the signals from one laser beam which had been split with a beam splitter into two beams of equal power (a second laser was not available at that time). The purpose of this run was to determine if there were correlated harmonic signals present in the flow like those obtained during the preceding test in the 14-inch Trisonic Wind Tunnel (see Appendix B). The two beams were passed through the free shear layer of the wedge shown in figure 2-1. The correlation at zero time lag (see figure 2-4B) was due partially to the correlated laser noise. The large peak at about 100 microseconds gives a speed of 1080 fps for the beam separation of 1.3 inches. The available supporting equipment and the test objective of part one would not allow the pursuit of this interesting result. Also, the facility-induced noise had not been fully investigated. Thus, no significant level of confidence could be put in the probability that the correlation or any portion of it was

*The peak of the correlogram will be used to determine the speed of the disturbances. This is not necessarily correct because of the dependence of the correlation function on both space and time. In this report, qualitative results are sought, and therefore this simplification should be justified.

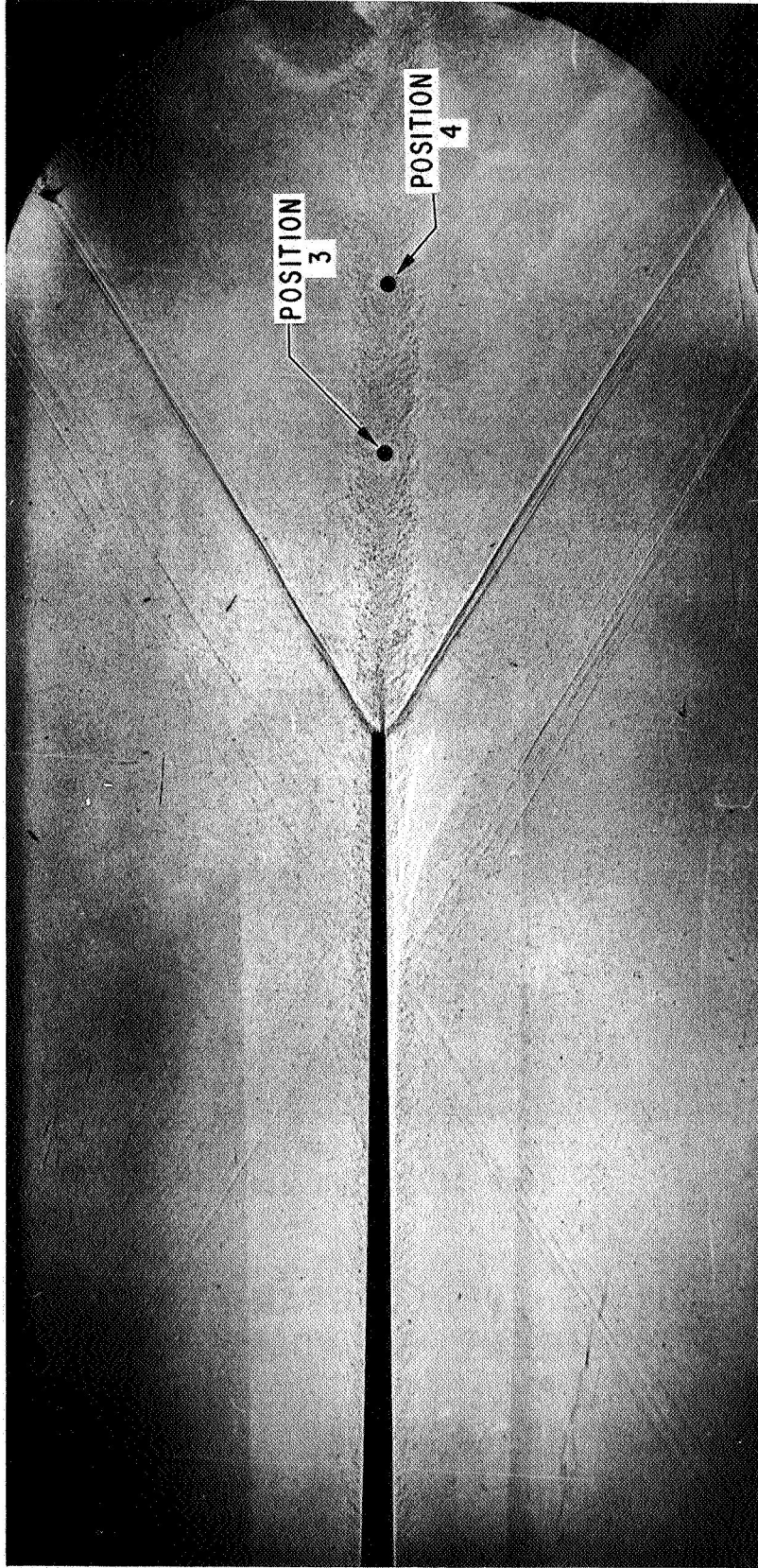


FIG. 2-3 SHADOWGRAPH OF FLOW FIELD
GENERATED BY THE THIN PLATE MODEL
INSTALLED IN THE 7 X 7" BWT WITH
THE MACH 2 NOZZLE

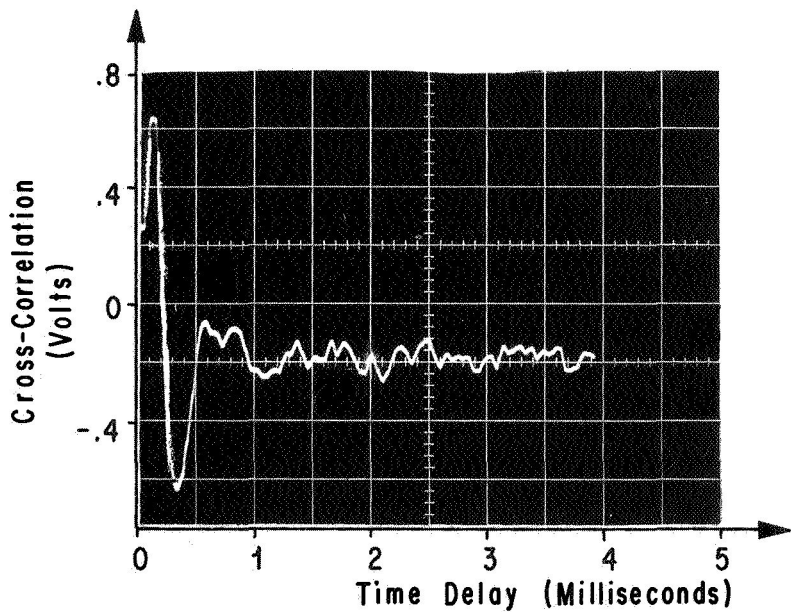
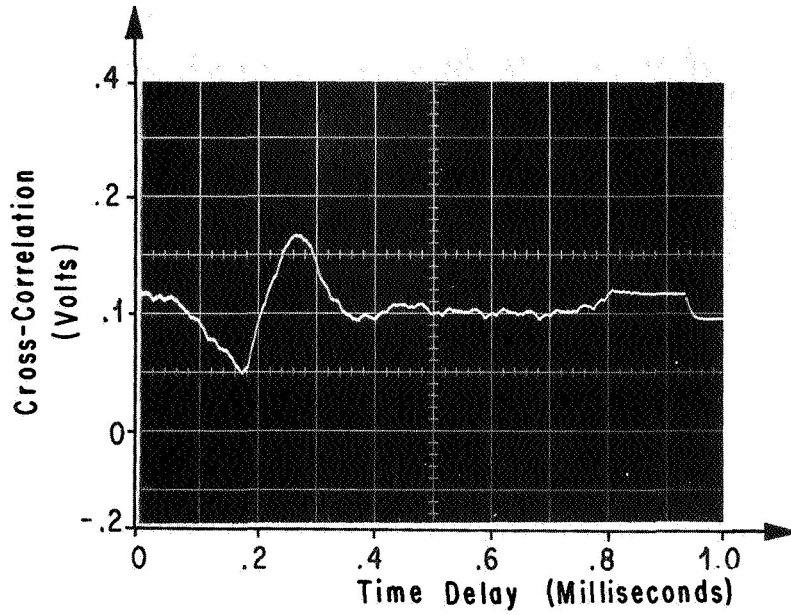


FIG. 2-4. A(TOP): CROSS-CORRELOGRAM FROM
 TURBULENT BOUNDARY LAYER
 ($M = 2.0$)
 B(BOTTOM): CROSS-CORRELOGRAM IN FREE
 SHEAR LAYER OF 2-D WEDGE
 ($M = 2.0$)

actually flow-related. In retrospect, it seems reasonable to suspect that there was a significant flow-related contribution to the correlogram. The indirect influence of this particular run upon the test results is, perhaps, of interest and will be discussed later.

After the cross-correlation was obtained in phase two (see figure 2-4A), it was necessary to determine the origin of the signals from which it was computed. It was evident from the shape of the subsequent cross-correlograms of the individual beams (figure 2-5) that there was little or no periodicity present in the signals. Furthermore, because of the near-zero value of these cross-correlations at zero time delay and the absence of correlated periodic noise, it could be deduced that the correlated facility-induced noise was very small. Finally, the shape of the autocorrelograms indicated that the correlated signals were of the wide band variety [4]. Two additional conditions had to be met in order to establish the fact that the correlations were truly flow-related: (1) The peak had to occur at a time delay which corresponded to the approximate expected speed of the disturbances,

$$\bar{U} = \frac{\xi}{\tau_m} ,$$

and (2) condition (1) had to hold as the beam separation (ξ) was varied.

The first runs to check these necessary conditions were made with the upstream beam (beam 1) and the downstream beam (beam 2) located in the wake of the model at positions 3 and 4, respectively (figure 2-3). The resulting cross-correlogram of the signals is shown in figure 2-6A. The beam separation and the time delay corresponding to maximum positive correlation gave a speed of 1415 fps, which was at least reasonably close to what was to be expected (free-stream speed was approximately 1660 fps). Then, beam 2 was moved upstream such that the beam separation (ξ) was decreased by one inch. The cross-correlogram for this case is shown in figure 2-6B. The maximum correlation corresponded to a speed of 1409 fps. Also, as would be expected, the strength of the peak correlation increased. The only difference between these runs, other than beam separation, was that the amplitude scale (voltage) on the oscilloscope was changed for the second run to accommodate the increase in amplitude of the correlation peak.

These results, verified by later experimental data discussed in the following sections, provide reasonable experimental evidence supporting the acceptance of the flow-related nature of the correlation peaks.

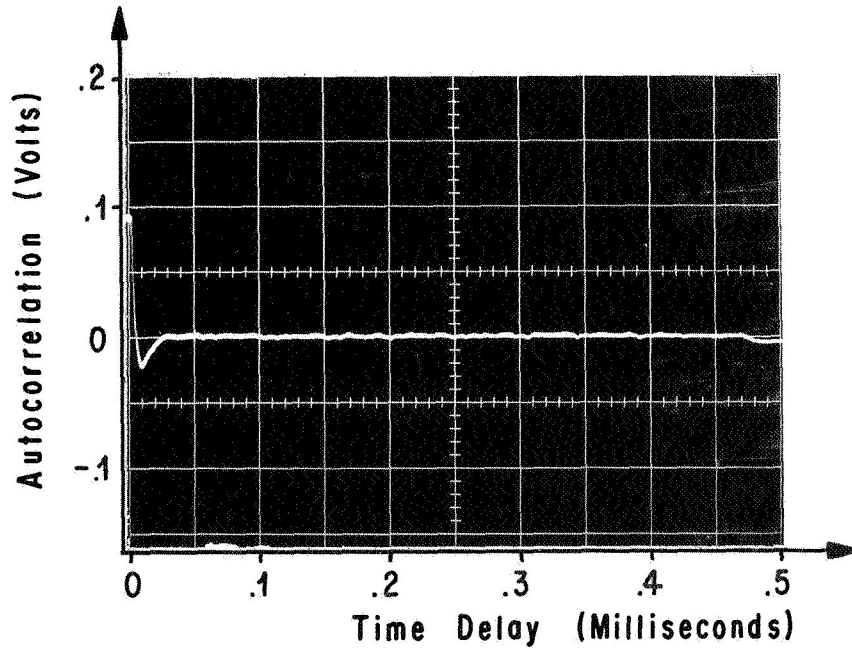
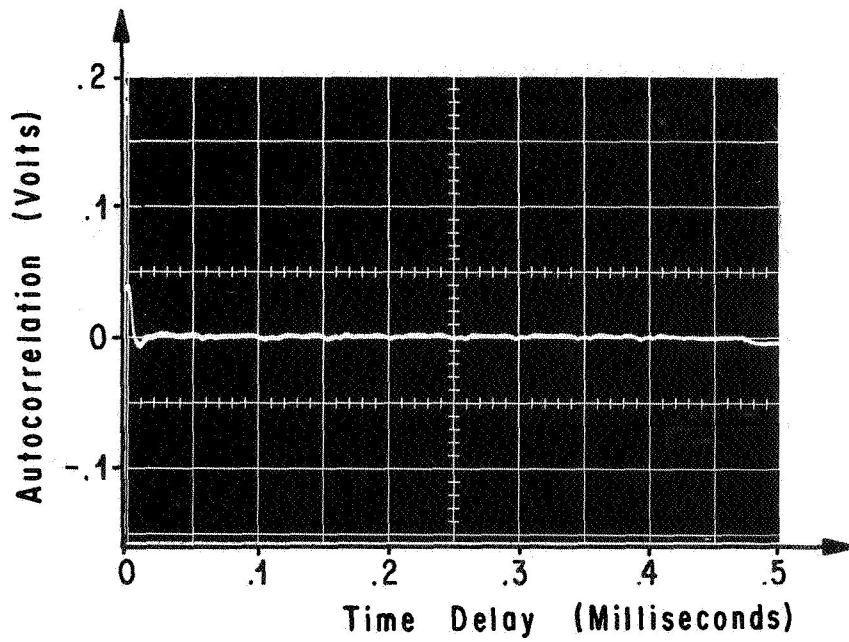


FIG. 2-5. A (TOP): AUTOCORRELATION OF SIGNAL ONE
 B (BOTTOM): AUTOCORRELATION OF SIGNAL TWO

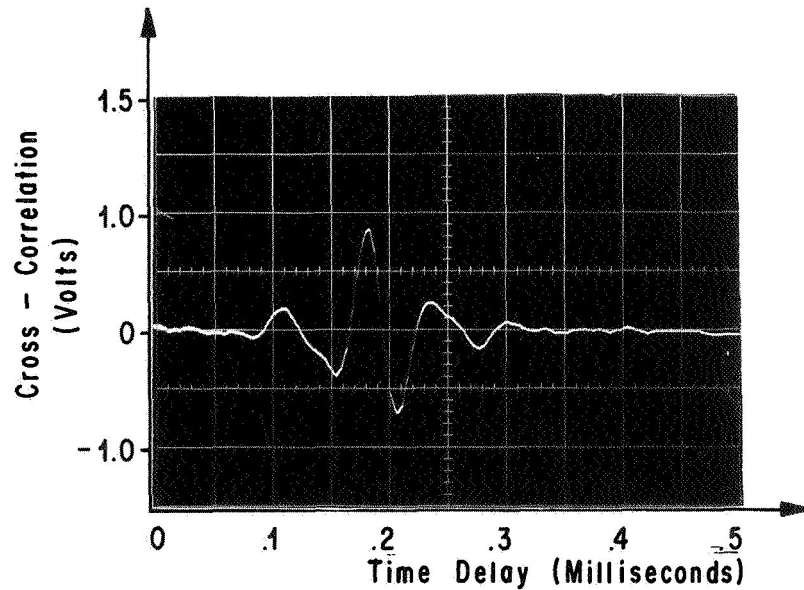
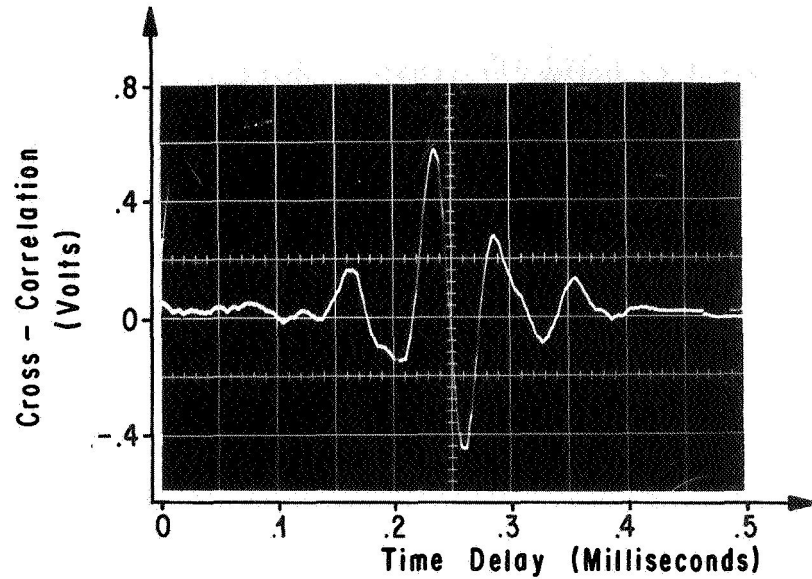


FIG. 2-6. A (TOP): CROSS - CORRELOGRAM
 FROM MEASUREMENT MADE IN WAKE OF PLATE.
 B (BOTTOM): CROSS - CORRELOGRAM
 FROM MEASUREMENT MADE IN WAKE OF PLATE
 WITH ONE INCH LESS BEAM SEPARATION
 THAN FIG. 2-6A.

Several new experimental and theoretical techniques were employed during this investigation which are, perhaps, worthy of note: (1) application of parallel beams for remote probing of a "two-dimensional" turbulent flow, (2) the laser quasi-schlieren and laser shadow-correlation modes of retrieving signals from a supersonic turbulent flow, (3) the "one-shot" auto- and cross-correlation methods for statistical analyses of random time histories, and (4) the theory of induced time delays for peak identification purposes.

Perhaps the most significant product of this feasibility test should be attributed to the attempt to correlate the random fluctuations of two beams of light originating from a common source. In itself, the splitting of a laser beam is, of course, common practice, but not previously applied using the cross-beam method. Nevertheless, the use of parallel beams from a common source leads to the initial "one-shot" autocorrelation concept described in section 3.2.1, and then to the "one-shot" cross-correlation, peak identification by the method of electronically induced time delay and a visual on-line display of the "one-shot" auto- and cross-correlograms. These methods are discussed in later sections.

III. DISCUSSION

3.1 Remote Sensing by Optical Correlation with Parallel Laser Beams

A theory of remote sensing of clear air turbulence using parallel laser beams (or other parallel light sources) in the supersonic regime is discussed, and experimental results are presented.

3.1.1 Theoretical Description of A Laser Quasi-Schlieren System

In figure 3-1 the beams from two lasers, L_1 and L_2 , are directed through the two-dimensional turbulent boundary layer shown in figure 2-3. The flow is supersonic ($M = 2.0$), and the boundary layer is fully developed along the thin plate. The beams, which are parallel to one another and perpendicular to the flow direction, are separated in the flow direction (along the x-axis) in such a manner that the eddies which intersect beam L_1D_1 at time, t , also intersect beam L_2D_2 at a later time, $t + \tau$.

Since the flow is approximately two-dimensional, the time-averaged flow properties should be approximately equal across the test section (i.e., as measured along either laser beam). This does not necessarily require that the instantaneous flow properties across the test section be equal.

The turbulence passing through one of these beams exhibits random fluctuating localized gradients of flow properties, e.g., local density gradient. As the eddies pass through a particular location on the beam, the resulting fluctuations of flow properties produce fluctuations of the local Poynting vector,* \vec{s} , of the laser beam.

If $\beta(y,t)$ represents the local instantaneous angular deviation, as measured from a horizontal reference line perpendicular to the flow direction, then

$$\vec{s} \cdot \hat{j} = |\vec{s}| \cos \beta(y,t), \quad (1)$$

*The Poynting vector is a vector tangent to the path of the beam with magnitude equal to the beam power.

NOTE: The derivation presented here for parallel beams is similar to one presented for cross-beams by Dr. L. Wilson, IITRI, in a memorandum to Dr. F. R. Krause, MSFC, December 26, 1968.

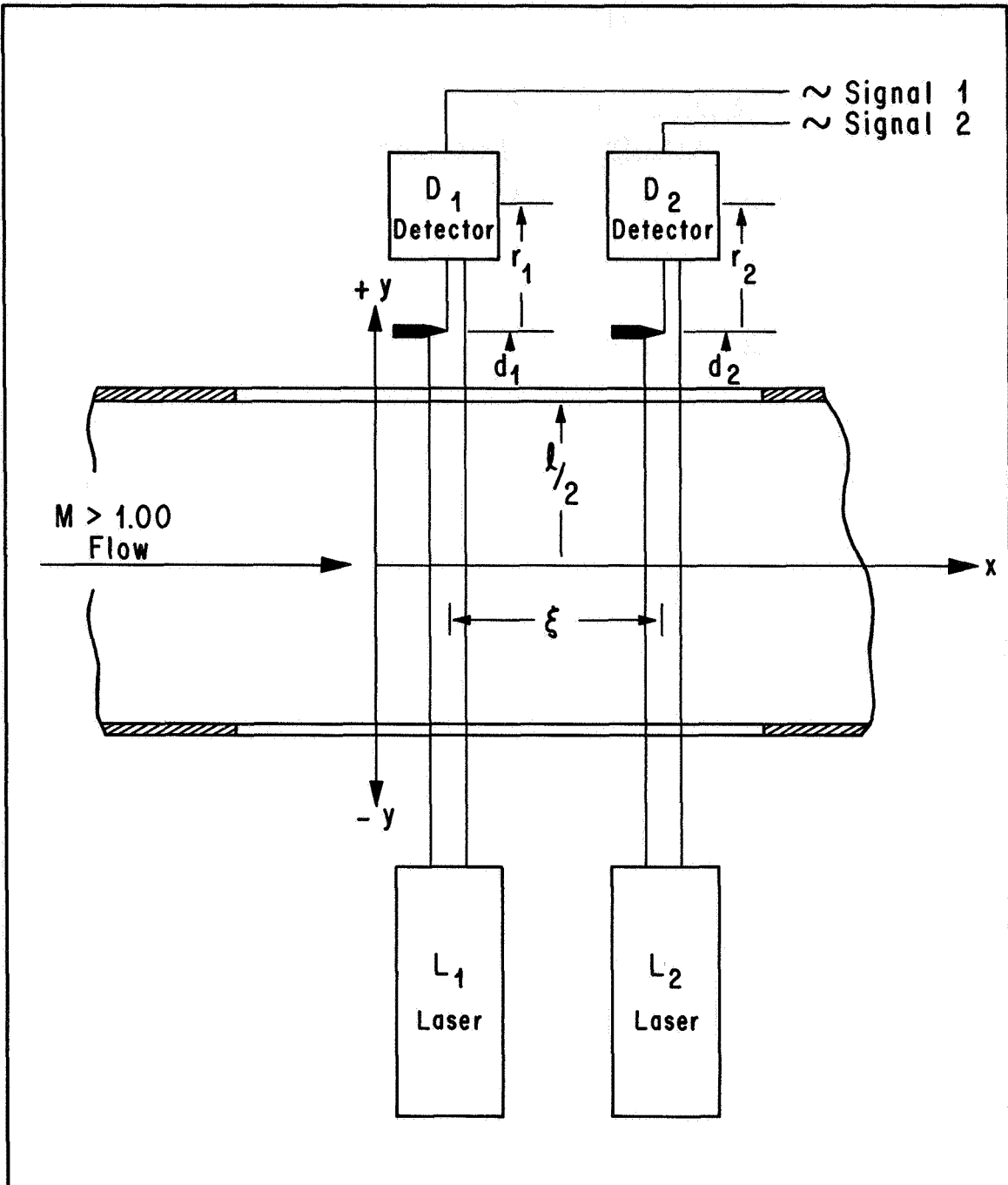


FIG. 3-1. PARALLEL BEAM ARRANGEMENT FOR REMOTE ACQUISITION OF 7 INCH B.W.T. DATA

where \hat{j} is a unit vector along the y-axis. Rearranging equation (1) results in

$$\beta(y,t) = \cos^{-1} \left\{ \frac{\bar{s} \cdot \hat{j}}{|\bar{s}|} \right\}. \quad (2)$$

This fluctuation, $\beta(y,t)$, is caused by a fluctuation of the local index of refraction, $n(x,y,z,t)$, and is related to the local fluctuation in the density gradient normal to the Poynting vector, \bar{s} , for a particular wavelength of light. The local index of refraction, $n(x,y,z,t)$, along the beam is proportional to the local density, $\rho(x,y,z,t)$. Provided the index of refraction is close to unity, as it is for most gases, the empirical Gladstone-Dale equation [1] is applicable. This equation, an empirical relationship between the index of refraction and the density of gas, is of the form

$$\frac{n_1 - 1}{\rho_1} = \frac{n_2 - 1}{\rho_2} = \text{constant} = \alpha \quad (3)$$

so that

$$n_o(y,t) = 1 + \alpha \rho_o(y,t) \quad (4)$$

for any point along the beam.

Let us assume that n and ρ are represented by

$$n(x,y,z,t) = \bar{n}(x,y,z) + n'(x,y,z,t) \quad (5)$$

and

$$\rho(x,y,z,t) = \bar{\rho}(x,y,z) + \rho'(x,y,z,t), \quad (6)$$

where n' and ρ' are the fluctuations about the time-averaged values of n and ρ . Substituting equations (5) and (6) into (4) gives

$$n = \bar{n} + n' = 1 + \alpha \bar{\rho} + \alpha \rho' \quad (7)$$

and

$$n' = \alpha \rho'. \quad (8)$$

It is desired to relate the beam deflection angle, $\beta(y,t)$, to the component of the index of refraction gradient which is perpendicular to the Poynting vector (path of beam). Since the index of refraction for air is very close to unity and since $\beta(y,t)$ will be small,

$$d\beta(y,t) \doteq \frac{1}{n} \frac{\partial n}{\partial x} dy. \quad (9)$$

Equation (9), the derivation of which can be found in most textbook presentations on the schlieren method of flow visualization [2], represents the fundamental relationship upon which the schlieren method is based. Substituting equation (7) into (9) yields

$$d\beta(y,t) \doteq \left\{ \frac{1}{n} \right\} \left\{ \frac{\partial \bar{n}}{\partial x} + \frac{\partial n'}{\partial x} \right\} dy. \quad (10)$$

Since $n - 1 \ll 1$ (n for air is approximately 1.00027), equation (10) can be simplified one step further:

$$d\beta(y,t) \doteq \frac{\partial \bar{n}}{\partial x} dy + \frac{\partial n'}{\partial x} dy. \quad (11)$$

The deflection of the Poynting vector away from the y -axis at a particular location on the beam (η) will be obtained by integrating along the beam from $y = -\ell$ to $y = \eta$:

$$\beta(\eta,t) \doteq \int_{-\ell}^{\eta} \frac{\partial \bar{n}}{\partial x} dy + \int_{-\ell}^{\eta} \frac{\partial n'}{\partial x} dy. \quad (12)$$

The first integral on the right-hand side of equation (12) represents the temporal-average angular beam deflection at η , and the second integral represents the fluctuation of the beam deflection about the temporal average. Thus,

$$\beta(\eta,t) \doteq \bar{\beta}(\eta) + \beta'(\eta,t). \quad (13)$$

Substituting equation (7) into (12) provides a relationship between β and ρ :

$$\beta(\eta, t) = \alpha \int_{-\ell}^{\eta} \frac{\partial \bar{\rho}}{\partial x} dy + \alpha \int_{-\ell}^{\eta} \frac{\partial \rho'}{\partial x} dy. \quad (14)$$

The beam deflections in these relationships are in the xy-plane only. It will be shown later why the deflections in the z-direction can be neglected. Also, another assumption will be introduced: the magnitude of the time-averaged beam deflection, $\bar{\beta}(\ell)$, is such that the knife-edge (which is used to produce the fluctuations in current monitored by the photodiode) allows one-half of the laser beam light to pass into the photodiode when the beam deflection equals $\bar{\beta}(\ell)$. Thus, equation (14) reduces to

$$\beta' = \alpha \int \frac{\partial \rho'}{\partial x} dy. \quad (15)$$

This assumption is convenient and can be applied experimentally. The fluctuations of β' can be related to the fluctuating output signal, $i(t)$, of a photodiode, as shown in figure 3-1.

A view taken along the laser beam (figure 3-2) shows the knife-edge, the eye of the photodiode, and the laser beam cross section. The beam is shown in a deflected position and in its time-averaged position (centered). Let

\bar{I}_d = time-averaged current output of the detector
power supply when knife-edge is removed.

A = cross-sectional area of laser beam.

D = diameter of laser beam.

Δ = beam displacement perpendicular to and measured
from the knife-edge.

ΔA = the change in area of the beam cut by a knife-
edge due to a deflection of the beam off center.

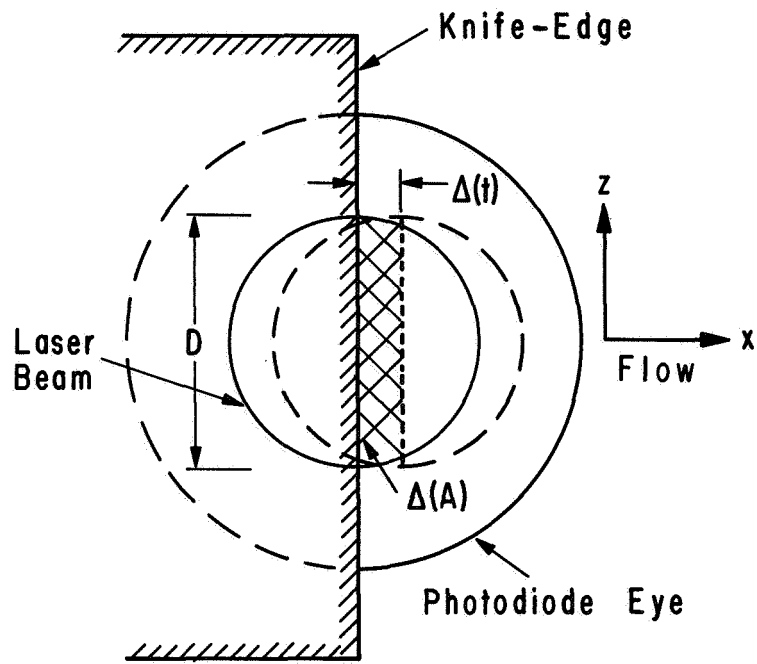


FIG. 3-2. EFFECT OF KNIFE-EDGE
ON THE DEFLECTED BEAM

Then, figure 3-2 shows that

$$\Delta A = \frac{D^2}{4} \left(\sin^{-1} (2\Delta/D) + \frac{2\Delta}{D^2} \sqrt{D^2 - 4\Delta^2} \right). \quad (16)$$

For small Δ ,

$$\Delta A \doteq D\Delta. \quad (17)$$

The photodetector output per unit area of the laser beam is

$$\frac{\bar{I}_d}{A} = \frac{4\bar{I}_d}{\pi D^2}. \quad (18)$$

To obtain the fluctuation of the output voltage (or current) from the photodetector, (i), we now multiply the output per unit area by the decrease (or increase) in beam area cut by the knife-edge due to a beam displacement of Δ :

$$i(t) \doteq \frac{4\bar{I}_d \Delta}{\pi D}, \quad \text{for } (\Delta \ll D). \quad (19)$$

Further, Δ is related to $\beta'(l, t)$:

$$\Delta = d \cdot \beta'(l, t). \quad (20)$$

Substituting equation (20) into (19) gives

$$i(t) = \left(\frac{4d\bar{I}_d}{\pi D} \right) \beta'(l, t). \quad (21)$$

The group of terms in parentheses on the right-hand side of equation (21) is a measure of the sensitivity, s , of the system [3],

$$s = \frac{4d\bar{I}_d}{\pi D}. \quad (22)$$

The sensitivity of the photodiode with respect to beam position was assumed constant, as was the intensity profile across the laser beam diameter. These assumptions, however, may be far from true and should be checked. By placing a lens between the knife-edge and the photodiode, the beam movement on the photodiode can be considerably reduced.

Substituting equation (22) into (21) gives

$$i(x,t) = s \cdot \beta'(x, \ell, t). \quad (23)$$

3.1.2 Cross-Correlation of Signals

Equation (23) holds for both beams, so that

$$i_1(x,t) = s_1 \beta_1'(x, \ell, t) \quad (24)$$

$$i_2(x + \xi, t) = s_2 \cdot \beta_2'(x + \xi, \ell, t). \quad (25)$$

Substituting equation (15) into equations (24) and (25) provides relationships between i and $\partial \rho' / \partial x$,

$$i_1(x,t) = s_1 \alpha \int_{-l}^l \frac{\partial \rho_1'(x, y_1, t)}{\partial x} dy_1 \quad (26)$$

$$i_2(x + \xi, t) = s_2 \alpha \int_{-l}^l \frac{\partial \rho_2'(x + \xi, y_2, t)}{\partial x} dy_2, \quad (27)$$

which hold along a particular eddy "streamline."

The signal, i_2 , from the downstream beam, is delayed by τ seconds and the time-average magnitude of the cross product, $\overline{i_1 \cdot i_2}$, is calculated. This represents the cross-covariance of the signals I_1 and I_2 [$I = 1/2 \overline{I_d} + i(t)$], or the cross-correlation of the fluctuating components, i_1 and i_2 . The cross-correlation of i_1 and i_2 will be used in the following discussion.

The cross-correlation, $R(\xi, \tau)$, is defined as [4]

$$R(\xi, \tau) = \lim_{T \rightarrow \infty} \frac{1}{T} \int_0^T i_1(x, y_1, t) \cdot i_2(x + \xi, y_2, t + \tau) dt, \quad (28)$$

where T is the averaging time. It is assumed that T is large enough so that

$$R(\xi, \tau) = \frac{1}{T} \int_0^T i_1(x, y_1, t) \cdot i_2(x + \xi, y_2, t + \tau) dt \quad (29)$$

is a good assumption. Also, stationarity is assumed (i.e., time-averaged statistical values are independent of time).

In equation (29), $R(\xi, \tau)$ will be maximum when i_2 is delayed by the most probable transit time of the common disturbances ($\tau = \tau_m$) provided the signal-to-noise ratios and averaging time, T , are compatible and will allow the desired peak to rise well out of the correlated noise floor. Otherwise, the correlated noise will influence the shape and maximum position (τ_m) of the peak. Correlated noise can often hide the peak altogether. The latter is likely to occur when the peak height is approximately equal to, or less than, the level of the correlated noise floor.

Substituting equations (26) and (27) into (29) gives

$$R(\xi, \tau) = \frac{1}{T} \int_0^T \left\{ s_1 \alpha \int_{-l}^l \frac{\partial \rho_1'(x, y_1, t)}{\partial x} dy_1 \right\} \left\{ s_2 \alpha \int_{-l}^l \frac{\partial \rho_2'(x + \xi, y_2, t + \tau)}{\partial x} dy_2 \right\} dt. \quad (30)$$

Rearranging the order of integration, we obtain

$$R(\xi, \tau) = s_1 s_2 \alpha^2 \int_{-l}^l \int_{-l}^l \overline{\left\{ \frac{\partial \rho_1'}{\partial x}(x, y_1, t) \cdot \frac{\partial \rho_2'}{\partial x}(x+\xi, y_2, t+\tau) \right\}} dy_1 dy_2, \quad (31)$$

where the bar indicates the time-average of the product inside the braces. Thus, equation (31) provides one interpretation of what the cross-correlation represents.

The cross-correlation of the signals i_1 and i_2 from two parallel beams is equal to a constant ($s_1 s_2 \alpha^2$) multiplied by the double line integral, one taken along each beam, of the two-point-product time-average value of the fluctuating density gradient component in the flow direction.

Another, and, perhaps a better, description is the one which shows the sequence of physical relationships between the parameters being measured experimentally.

Beginning with the on-line analog correlator and moving opposite to the flow of data, the following physical events are taking place (see Appendix A, figure A-11):

- (1) The scope displays the cross-correlation function versus time delay (τ) which is received from the analog correlator.
- (2) The correlator is computing the cross-correlation from the two electrical signals, i_1 and i_2 , originating from the photodiodes.
- (3) The time history of the signals are directly proportional to the angular deflections of the laser beams, respectively:

$$i(t) = s\beta'(l, t).$$

- (4) The angular deflection $\beta'(l, t)$ of each beam is proportional to the fluctuating component of the density gradient in the direction of flow, where the mean is an instantaneous spatial average taken along the laser beam, i.e., from equation (15):

$$\beta'(\ell, t) = \alpha \int_{-\ell}^{\ell} \frac{\partial \rho'(x, y, t)}{\partial x} dy. \quad (15)$$

Multiplying and dividing the right-hand side of equation (15) by the width of the test section ($2\ell = L$) gives

$$\beta'(\ell, t) = 2\ell\alpha \left\{ \frac{1}{2\ell} \int_{-\ell}^{\ell} \frac{\partial \rho'(x, y, t)}{\partial x} dy \right\}. \quad (23)$$

Thus, at any particular instant (t_p),

$$\beta'(\ell, t_p) = 2\ell\alpha \left\{ \frac{\partial \rho'(x, y, t_p)}{\partial x} \right\}_{\text{avg. over } L}. \quad (32)$$

The substitution of $t = t_p$ is made only to emphasize that the average is taken along the beam as if the flow were frozen in time. This is not implying that the beam length average value of $\partial \rho' / \partial x$ does not vary with time; it does. This results from the speed of light being much greater than the flow speed. Thus, the effect is (or can be) of considerable advantage to two-dimensional aerodynamic remote-sensing with statistical correlation. The advantage is a decrease in the integration time required to retrieve correlated statistical information from data in the presence of noise because of the automatic optical integration performed by the laser beam. For the two-dimensional case, the signals $i_1(t)$ and $i_2(t)$ represent the fluctuating component of the density gradient, $(\partial \rho' / \partial x)$, spatially averaged along the respective beams. Therefore, the correlator is operating on data which are representative of "instantaneous" averages of random samples of data. The convergence, therefore, will be faster than for the three-dimensional case where the beams must

be crossed. Further, and much more important, the signal-to-noise ratio is at least an order of magnitude greater for two-dimensional flow fields similar in flow rate and geometrical size. This is not meant to imply that optical remote sensing of three-dimensional flows is not possible.

From the experimental point of view, these comments can be summarized as follows:

- (a) The correlation is representative of the similarity in the two electronic signals, i_1 and i_2 , received by the correlator after they have been influenced by the filters, amplifiers, and all other physical connections between the photo power supply output and the correlator input (see Appendix A, figure A-11). If the correlator is performing properly, this is simply a matter of experimental fact.
- (b) The signals are proportional to the angular deflections of the respective beams about a time-average value.
- (c) The signal represents the fluctuating (beam-average) x-component of the density gradient.

3.2 The "One-Shot" Autocorrelation

3.2.1 The Concept

In figure 3-3, a single laser beam is passed normal to the flow and along the particular station of interest. After passing through the test section, the beam is reflected downstream from mirror M1 to mirror M2. From mirror M2 it is reflected back across the flow at a predetermined location and parallel to the first pass through the flow. A photodetector, D1, receives the beam after its two passes through the test section. The signal is amplified and the analog correlator computes the autocorrelation versus time delay (autocorrelogram), as shown at the bottom of figure 3-3.

The autocorrelogram has two predominant peaks, one at zero time delay, as expected, and the second at a time delay, τ_m , corresponding to the most probable transit time of disturbances between the two positions where the beam passes through the test section. Although the beam

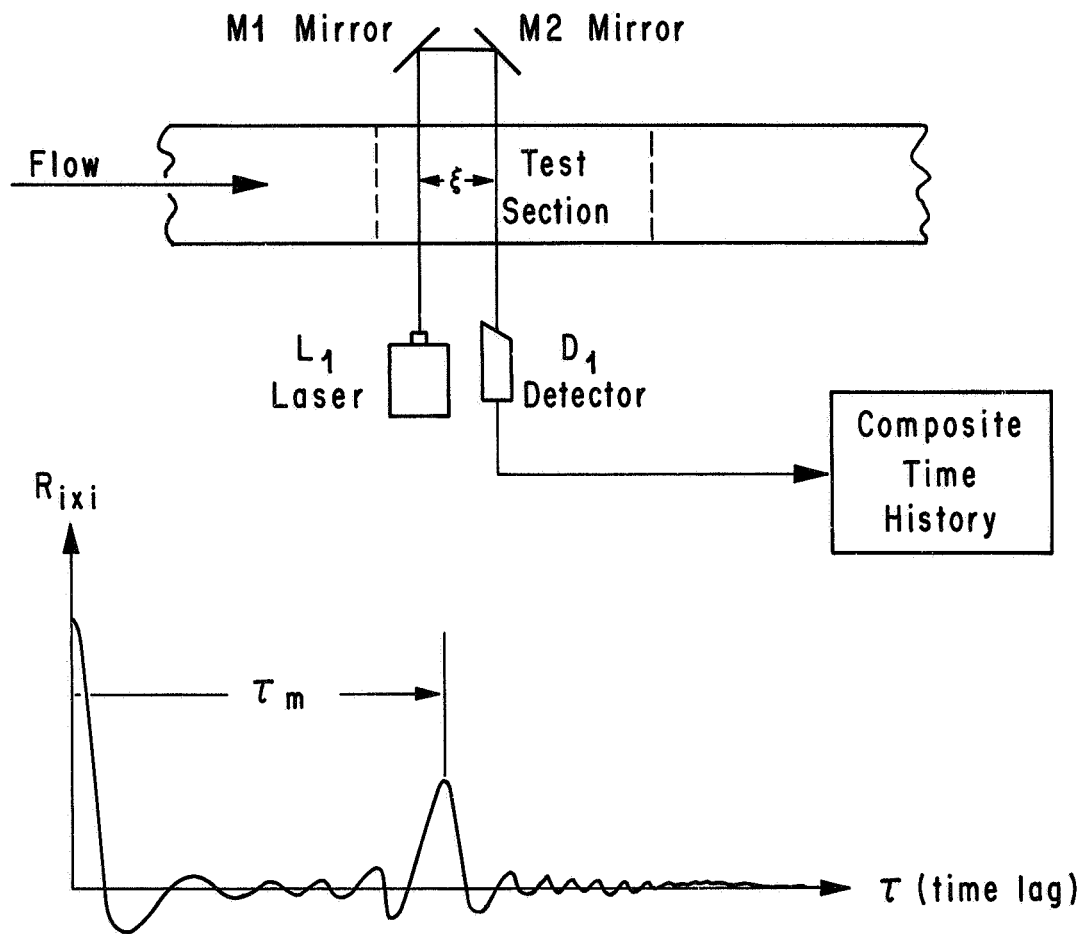


FIG. 3-3. THE "ONE-SHOT" AUTOCORRELATION FOR DETERMINATION OF CONVECTION SPEED IN TWO-DIMENSIONAL TURBULENCE

arrangement is similar to that of the parallel beam case, the desired flow information is contained in a single signal rather than in two separate ones. The second peak occurs at τ_m on the autocorrelogram because the signal received by the photodetector, D1, contains the same (or similar) information twice and at different times. The most probable separation in time corresponds to τ_m .

This statistical technique can be used in analyzing random data such as those produced in turbulent fluid flows. The technique, referred to in this report as the "one-shot" autocorrelation, is described as follows:

- The autocorrelogram of a single composite time history composed of the sum of two or more statistically correlated random signals which sufficiently lag one another will exhibit a correlation "peak" for each possible pair of the signals.

3.2.2 Multiple Signals

The extension of the concept would be to reflect the beam through the flow three or, perhaps, four times, as shown in figure 3-4. Although this technique will work in practice, it is preferable to avoid such a sensitive optical arrangement.

In figure 3-5, an equivalent arrangement is shown. One laser beam is split into four beams of equal intensity and directed through the flow. Each beam has a separate detector that receives the signal. The signals are added and the resulting signal is equivalent to the original single beam case. It is not necessary to use a single light source. Each detector could have an independent light source, or two or more detectors may share light from the same source.

The "one-shot" autocorrelation technique can, in theory, be applied to three-dimensional or two-dimensional flows. The only change required is a rearrangement of the beams so that no two are parallel and so that the effective correlated volume which is common to the beams is small enough to be acceptable. However, a longer integration time will be required for three-dimensional flows, as compared to two-dimensional flows, because of the lower signal-to-noise ratio of the former.

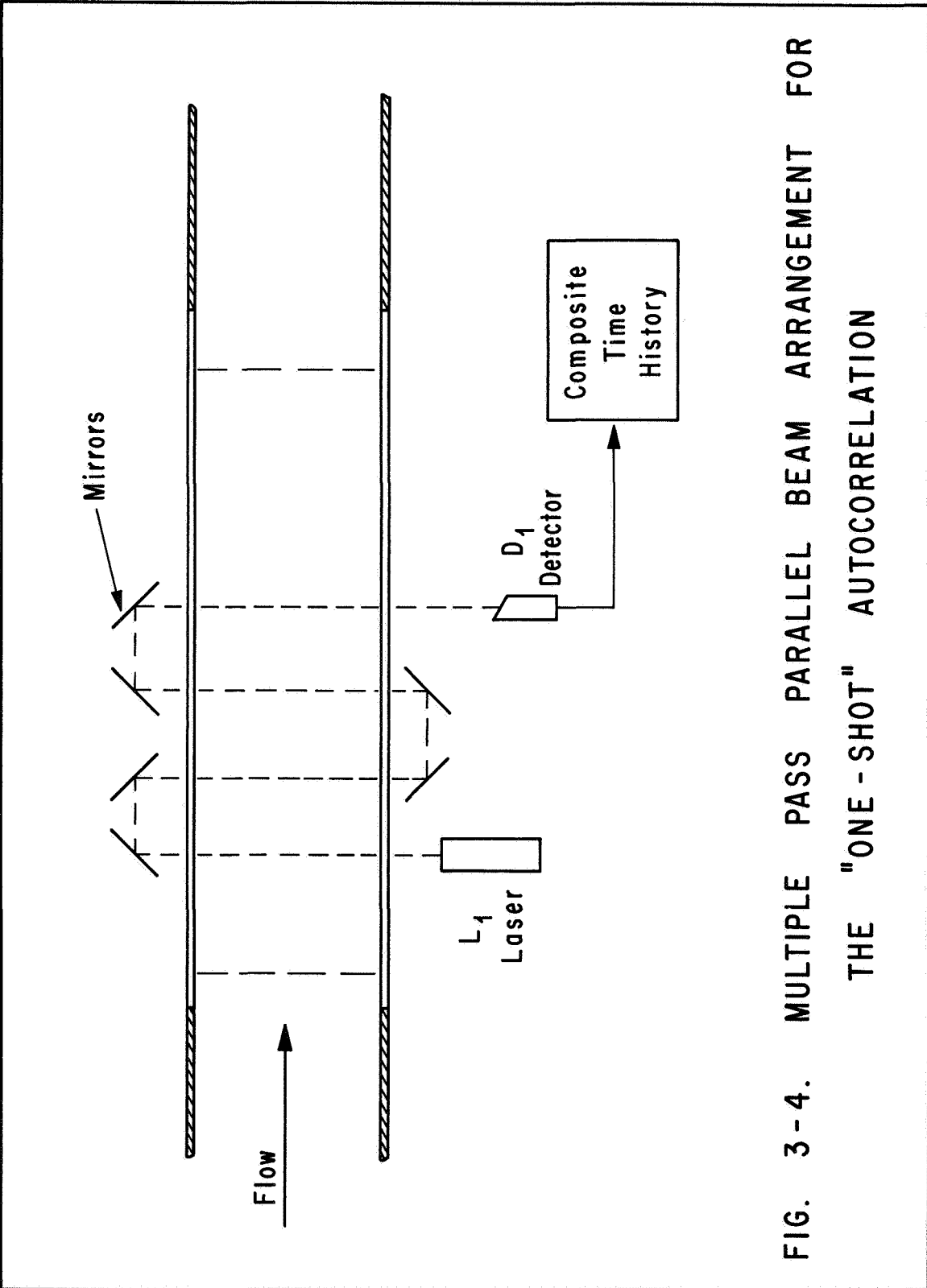
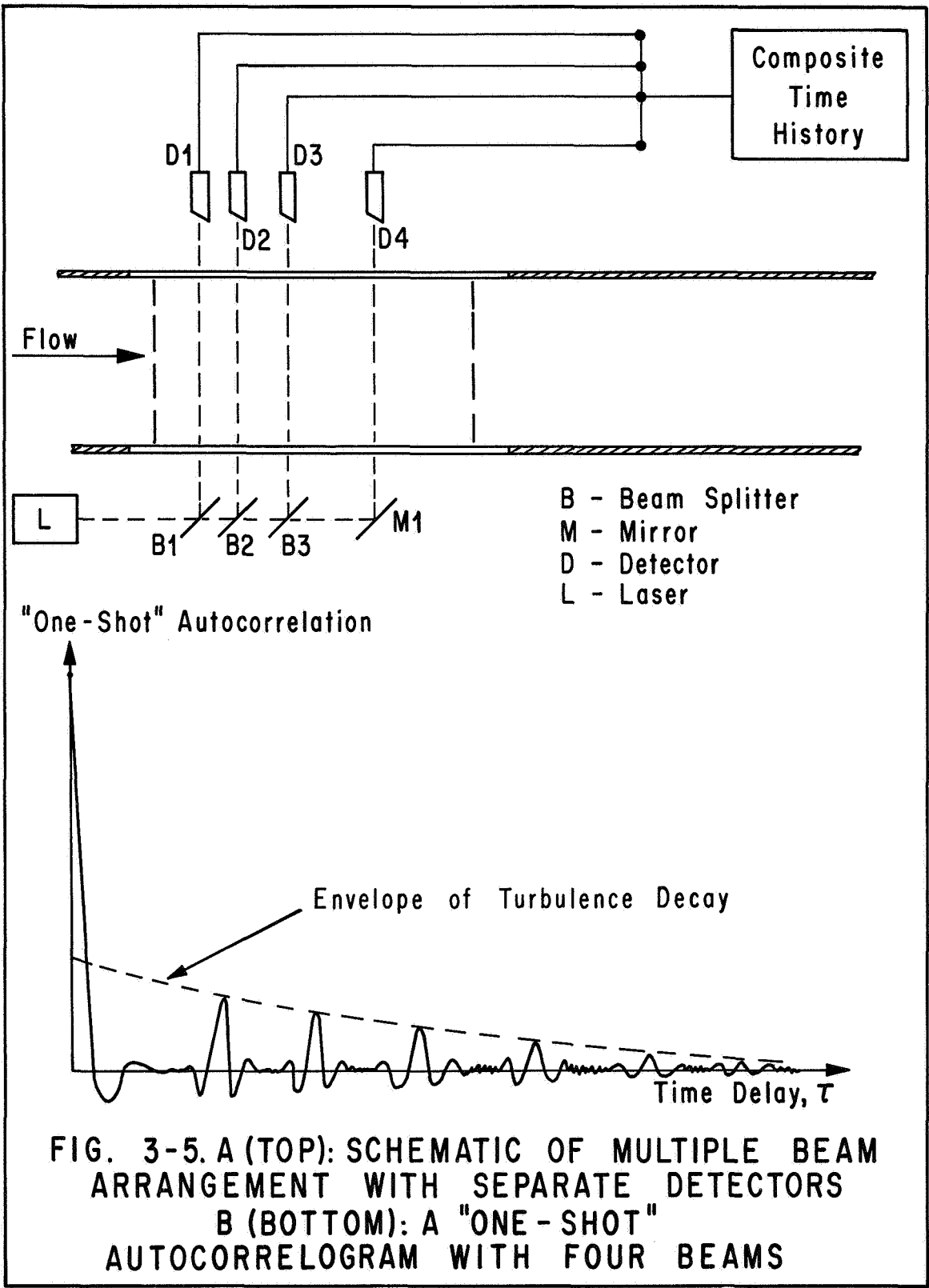


FIG. 3-4. MULTIPLE PASS PARALLEL BEAM ARRANGEMENT FOR THE "ONE-SHOT" AUTOCORRELATION



3.2.3 Peak Identification

Consider a single time history of broad-band random data, $F(t)$, (i.e., distributed over a wide range of frequencies) which is composed of two random time histories $f_1(t)$ and $f_2(t)$ such that

$$F(t) = f_1(t) + f_2(t) \quad (33)$$

and the mean values of the time histories are zero. The autocorrelation of $F(t)$ is

$$A(\tau) \stackrel{\Delta}{=} \lim_{T \rightarrow \infty} \frac{1}{T} \int_0^T [f_1(t) + f_2(t)][f_1(t + \tau) + f_2(t + \tau)] dt \quad (34)$$

$$A(\tau) \stackrel{\Delta}{=} \overline{f_1(t) \cdot f_1(t + \tau)} + \overline{f_1(t) \cdot f_2(t + \tau)} + \overline{f_2(t) \cdot f_1(t + \tau)} + \overline{f_2(t) \cdot f_2(t + \tau)} \quad (35)$$

$$A(\tau) \stackrel{\Delta}{=} A_1(\tau) + R_{12}(\tau) + R_{21}(\tau) + A_2(\tau). \quad (36)$$

In equation (36) letters "A" and "R" represent autocorrelation and cross-correlation, respectively. The subscripts indicate the signals involved in the particular correlation, as well as the order of the cross-correlation operation with regard to the time histories.

Since

$$R_{21}(\tau) = R_{12}(-\tau), \quad (37)$$

Substituting equation (37) into (36) gives

$$A(\tau) \stackrel{\Delta}{=} A_1(\tau) + R_{12}(\tau) + R_{12}(-\tau) + A_2(\tau). \quad (38)$$

If we assume, for the present, that $f_1(t)$ and $f_2(t)$ are statistically independent and thus not correlated, equation (38) reduces to

$$A(\tau) = A_1(\tau) + A_2(\tau). \quad (39)$$

$1 \rightarrow 2$

For this case, the "one-shot" autocorrelogram will have only one large peak* at $\tau = 0$ similar to the autocorrelogram shown in figure 3-6 (top). The magnitude of the peak at $\tau = 0$ is

$$A(0) = A_1(0) + A_2(0). \quad (40)$$

$1 \rightarrow 2$

Beginning again with equation (38), we assume that $f_1(t)$ and $f_2(t)$ are identically equal for all t when $f_2(t)$ is delayed by τ_m seconds and compared to $f_1(t)$, i.e., at

$$\tau = \tau_m \quad (41)$$

$$f_1(t) \equiv f_2(t + \tau_m), \quad \text{for all } t \quad (42)$$

where τ_m is the time lag of maximum correlation. For this case,

$$F(t) = f_1(t) + f_2(t), \quad (43)$$

and substituting equation (42) into equation (35) gives

$$A(\tau_m) = A_1(\tau_m) + R_{12}(\tau_m) + R_{12}(-\tau_m) + A_2(\tau_m). \quad (44)$$

$1 \rightarrow 2$

*The reference to the word "peak" implies the maximum positive peak in a local region on the autocorrelogram. The natural shape of the auto- and cross-correlograms, near the time lag, τ_m , generally exhibits three or more peaks depending upon the frequency range of the correlated portion of the signals.

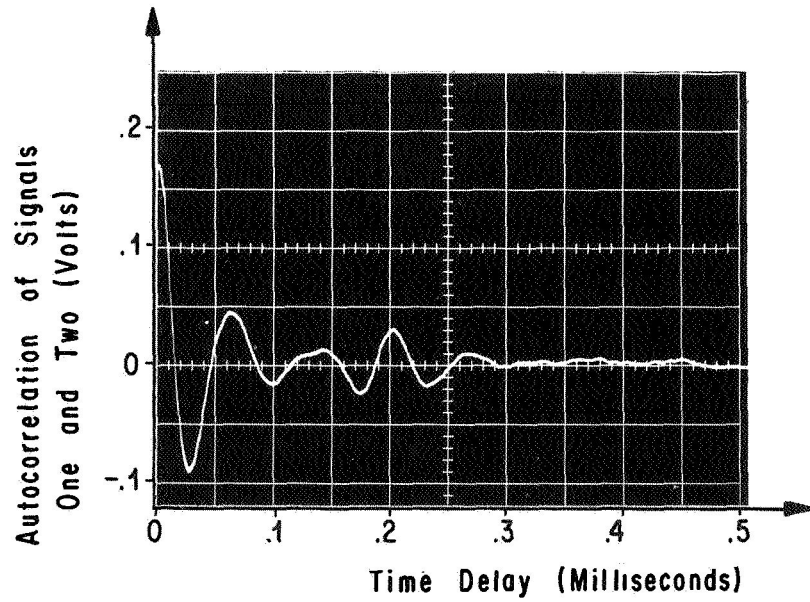
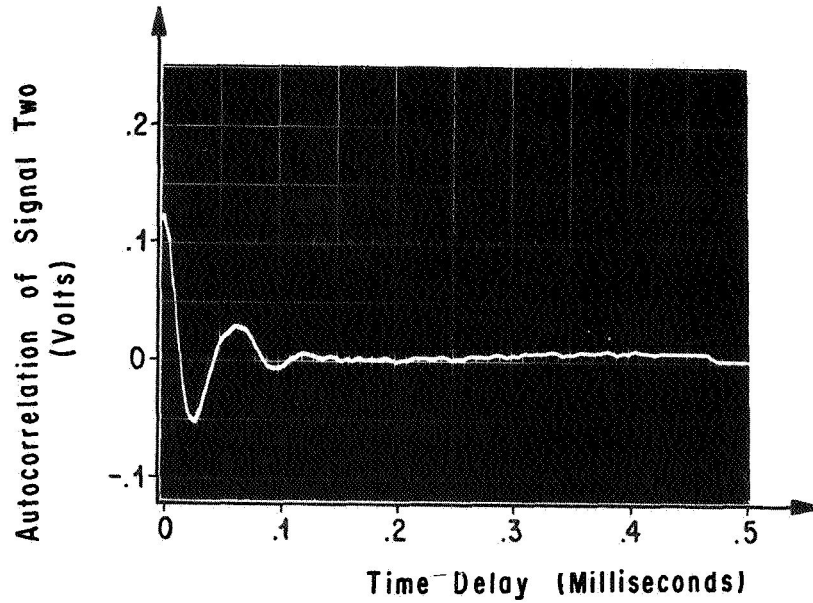


FIG. 3-6 A(TOP): AUTOCORRELATION OF SIGNAL TWO vs. TIME DELAY.
 B(BOTTOM): AUTOCORRELATION OF SIGNALS ONE AND TWO vs TIME DELAY

If we assume that τ_m is positive and large enough to prevent an interference between the peak at τ_m and the zero time lag peak on the autocorrelogram, we can deduce from equation (44) that

$$A(\tau_m) = R_{12}(\tau_m), \quad (45)$$

$$1 \rightarrow 2$$

since

$$A_1(\tau_m) = 0 \quad (45a)$$

$$A_2(\tau_m) = 0 \quad (45b)$$

$$R_{12}(-\tau_m) = 0. \quad (45c)$$

Equation (45) states that, if $f_1(t)$ and $f_2(t)$ are statistically random time histories and have maximum correlation when $f_2(t)$ is delayed in time by τ_m seconds, then the cross-correlation of two signals is equal to the "one-shot" autocorrelation provided that τ_m is sufficiently large. Therefore, there should be no problem in identifying the peak at τ_m because there should be only one (see bottom of figure 3-6). There is, however, a need to look a little deeper into the composition of the "one-shot" autocorrelogram.

Consider the case of the addition of three random signals where

$$F(t) = f_1(t) + f_2(t) + f_3(t). \quad (46)$$

The "one-shot" autocorrelation of $F(t)$ is

$$A(\tau) = A_1(\tau) + A_2(\tau) + A_3(\tau) + R_{12}(\tau) + R_{13}(\tau) + R_{23}(\tau) + R_{21}(\tau) \\ 1 \rightarrow 3 \\ + R_{32}(\tau) + R_{31}(\tau). \quad (47)$$

Using the general form of equation (37), we obtain

$$A(\tau) = A_1(\tau) + A_2(\tau) + A_3(\tau) + R_{12}(\tau) + R_{13}(\tau) + R_{23}(\tau) \\ 1 \rightarrow 3 \\ + R_{12}(-\tau) + R_{23}(-\tau) + R_{13}(-\tau). \quad (48)$$

If it is assumed that all peaks resulting from the cross-correlations in equation (48) lie in the positive time lag range only, the last three cross-correlations in equation (48) drop out.

$$A(\tau) = A_1(\tau) + A_2(\tau) + A_3(\tau) + R_{12}(\tau) + R_{13}(\tau) + R_{23}(\tau). \quad (49)$$

$$1 \rightarrow 3$$

Again, let us assume that the time lags between regions of correlation on the "one-shot" autocorrelogram are large enough to prevent overlapping of peaks. Let τ_{12} be equal to the time lag of maximum correlation between $f_1(t)$ and $f_2(t)$, τ_{13} the time lag of peak correlation between $f_1(t)$ and $f_3(t)$, and τ_{23} the time lag of maximum correlation between $f_2(t)$ and $f_3(t)$. Then, the value of the "one-shot" autocorrelation at the above τ_{ij} 's will be

$$A(\tau_{12}) = R_{12}(\tau_{12}) + R_{23}(\tau_{12}) \quad (50)$$

$$1 \rightarrow 3$$

$$A(\tau_{13}) = R_{13}(\tau_{13}) + R_{23}(\tau_{13}) \quad (51)$$

$$1 \rightarrow 3$$

$$A(\tau_{23}) = R_{23}(\tau_{23}) + R_{12}(\tau_{23}) + R_{13}(\tau_{23}). \quad (52)$$

$$1 \rightarrow 3$$

If we assume that no overlapping of regions of correlation occur, then equations (50), (51), and (52) reduce to

$$A(\tau_{12}) = R_{12}(\tau_{12}) \quad (53)$$

$$1 \rightarrow 3$$

$$A(\tau_{13}) = R_{13}(\tau_{13}) \quad (54)$$

$$1 \rightarrow 3$$

$$A(\tau_{23}) = R_{23}(\tau_{23}). \quad (55)$$

$$1 \rightarrow 3$$

Figure 3-7 shows a three-beam arrangement, where the parallel beams pass over the plate and through the turbulent boundary layer. The free-stream flow speed was approximately 1660 fps. The signals from the two photo-detectors A and B were added, amplified, and filtered. The resulting signal was autocorrelated on-line. The autocorrelogram is shown in figure 3-8 (top). The peak at the zero time lag is characteristic of all autocorrelograms of a wide-band time history. The peak at $\tau = 0.128$ ms is apparently a result of the correlation between beams 1 and 2. It will be shown later that this peak is actually a result of the correlation between beams 1 and 2 summed with that between beams 2 and 3. The peak at $\tau = 0.254$ ms represents the correlation between beams 1 and 3. The beam separations, ξ_{ij} , (i.e., ξ_{12} is the distance between beams (1) and (2), etc.) were

$$\xi_{12} = 2.63'' \quad \text{and} \quad \xi_{13} = 4.95''$$

which give average speeds of

$$\bar{U}_{12} = \frac{\xi_{12}}{12\tau_{12}} = 1710 \text{ fps}$$

and

$$\bar{U}_{13} = \frac{\xi_{13}}{12\tau_{13}} = 1525 \text{ fps.}$$

The beams were approximately 0.2 inch above the plate, near the outer region of the boundary layer. The speed \bar{U}_{12} hardly seems reasonable because the free-stream speed was 1660 fps; the speed \bar{U}_{13} is closer to the expected value. However, there should have been a third peak representing the correlation between the second and third beams, $R_{23}(\tau_{23})$. Dividing the beam separation, ξ_{23} , by the speed, \bar{U}_{13} , should represent a good approximation to the location of the peak (τ_{23}) ($\xi_{23} = \xi_{13} - \xi_{12} = 2.32''$).

$$\tau_{23} = \frac{\xi_{23}}{12\bar{U}_{13}} = 0.127 \text{ ms.}$$

It appears that the "peak" at 0.128 ms is actually a result of the overlapping of two peaks, and thus does not represent the independent location of either. To check the above logic, the first beam was moved 1.00 inch downstream. This reduced the beam separation distances, ξ_{12}

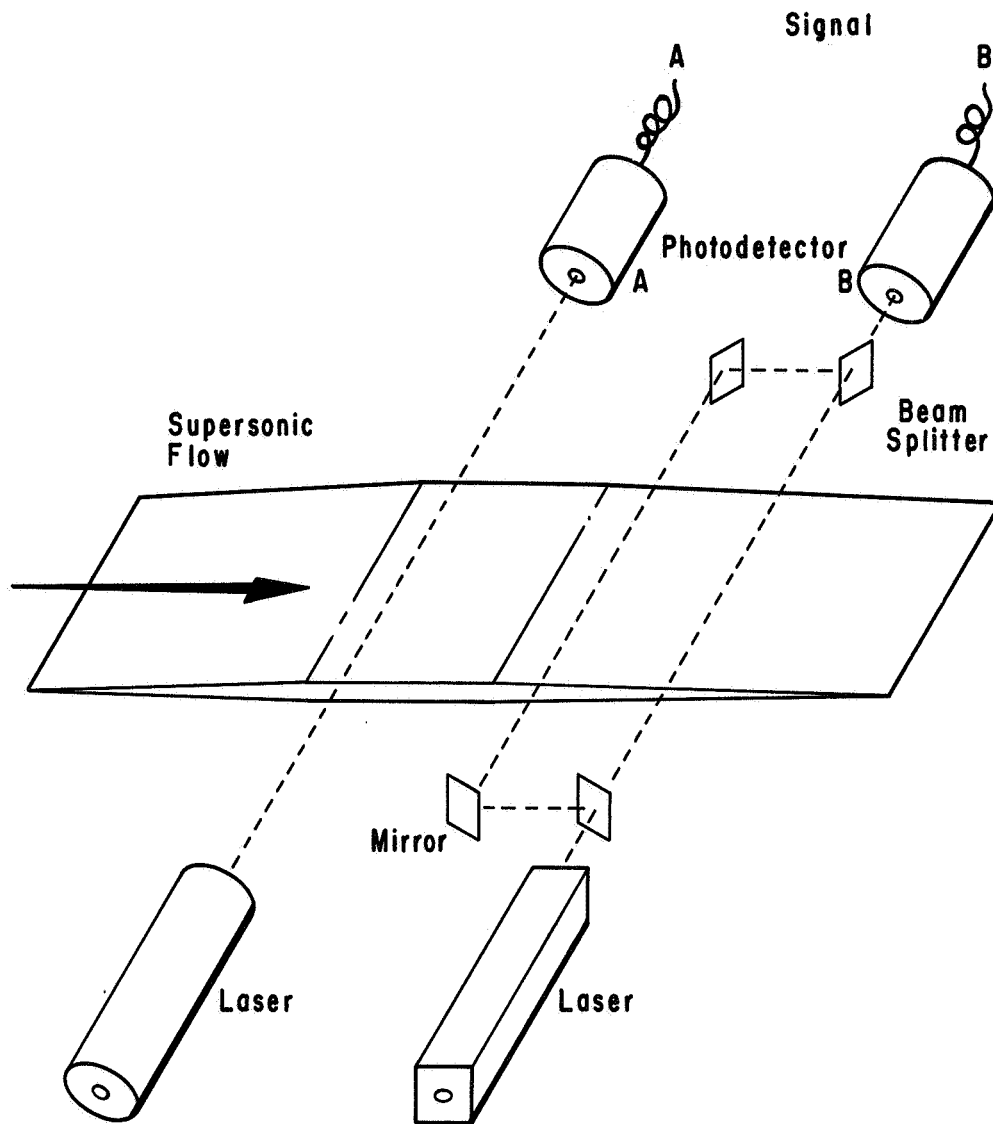


FIG. 3-7. PARALLEL BEAM ARRANGEMENT WITH THREE LASER BEAMS. BOTH, OPTICAL AND ELECTRICAL ADDITION OF SIGNALS ARE USED

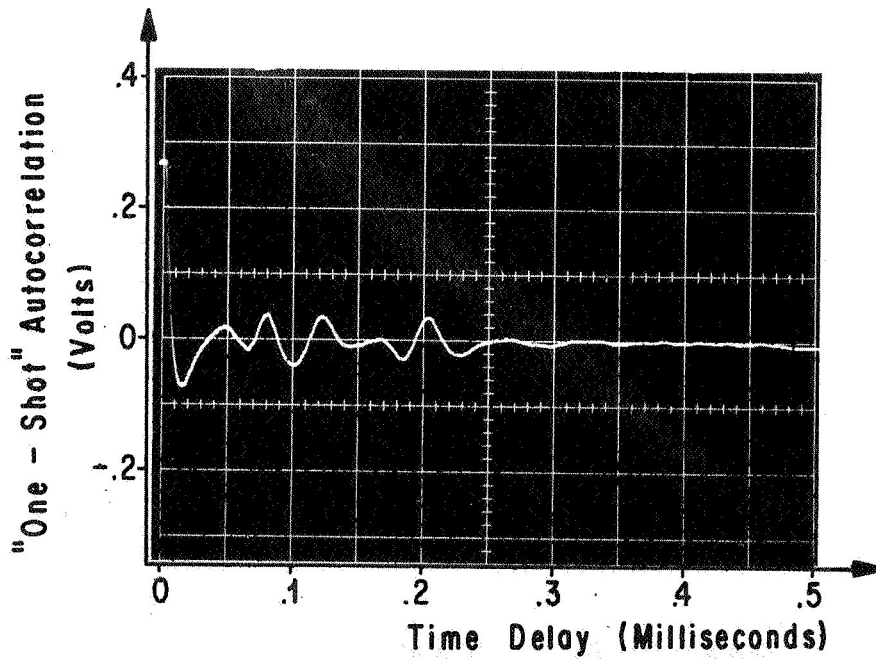
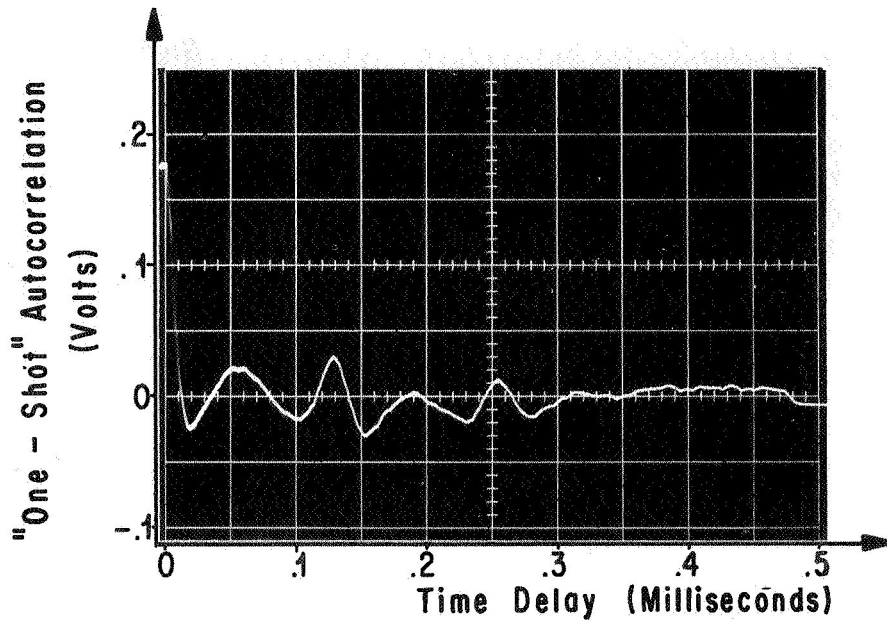


FIG. 3-8.. "ONE-SHOT" AUTOCORRELATIONS AS OBTAINED WITH A THREE PARALLEL BEAM ARRANGEMENT AS SHOWN IN FIGURE 3-7

and ξ_{13} , to 1.63 and 3.95 inches, respectively. However, the separation between the second and third beams, ξ_{23} , was not changed. The "one-shot" autocorrelogram for this beam geometry is shown in figure 3-8 (bottom).

From figure 3-6B, we see

$$\tau_{12} = 0.082 \text{ ms}$$

$$\tau_{13} = 0.203 \text{ ms}$$

$$\tau_{23} = 0.123 \text{ ms.}$$

The corresponding speeds are

$$\bar{U}_{12} = 1660 \text{ fps}$$

$$\bar{U}_{13} = 1521 \text{ fps}$$

$$\bar{U}_{23} = 1570 \text{ fps.}$$

The purpose of this run was to show that the peak at τ_{23} did exist. The value of \bar{U}_{12} should not be considered accurate because the peak at $\tau_{12} = 0.123 \text{ ms}$ is too close to τ_{12} to be considered accurate. There are, however, at least two ways by which peak overlapping can be avoided. These will be discussed in section 3.2.5. It is important that the number of peaks expected to appear for a particular number of beams is known in advance, as well as their expected location on the "one-shot" autocorrelogram.

In general, the number of peaks on the "one-shot" autocorrelogram will be

$$\text{No. of peaks} = 1 + \sum_{k=1}^{m-1} (m - k) \quad (56)$$

provided that none are destroyed by overlapping. The peak at zero time lag has been included in equation (56).

The "one-shot" autocorrelation could be used to study the characteristics of the decay of turbulent structures from data obtained from a single run of a wind tunnel or jet facility. The peaks resulting from

correlations between the first beam and each of the downstream beams give a picture of the "lifetime" of the average eddy in a stationary frame of reference. In addition, the peaks resulting from correlations between the second beam and the downstream beams represent the eddy lifetime a second time, but beginning at a different location (i.e., ξ_2 further downstream). Likewise, the series of peak associated with the third beam and each beam downstream from it provides still another history of the decay. Therefore, the "one-shot" autocorrelogram is composed of at least one decay history (two beams) and, where more than two beams are used, there will be $m - 1$ of such histories, each history beginning a distance downstream from the last equal to the beam separation (see figure 3-9).

If the assumption is made that the decay history is independent of position over the distance between the first and last beams, we see that all of these time histories fall on the curve of the first time history, which begins with the first beam (see figure 3-10). It follows, for this case, that a peak resulting from correlation between two downstream beams provides the same information as the correlation between the first beam and an additional beam having the same beam separation as the two downstream beams.

This characteristic of the "one-shot" autocorrelation is important with respect to the number of beams required to determine the decay history. For example, three beams provide four points on the decay curve, and four beams provide seven.

3.2.4 Interpretation of the Zero Time Lag Peak

The zero time lag value of the decay curve is not represented by the zero time lag value of the "one-shot" autocorrelation. However, this value can be calculated to a good approximation in many cases.

Consider the general case of m number of time histories where $f_i(t)$ represents the i th time history and

$$F(t) = \sum_{i=1}^m f_i(t). \quad (57)$$

The general form of the "one-shot" autocorrelation is

$$A(\tau) = \lim_{l \rightarrow m} \lim_{T \rightarrow \infty} \frac{1}{T} \int_0^T \sum_{i=1}^m f_i(t) \cdot \sum_{j=1}^m f_j(t + \tau) dt. \quad (58)$$

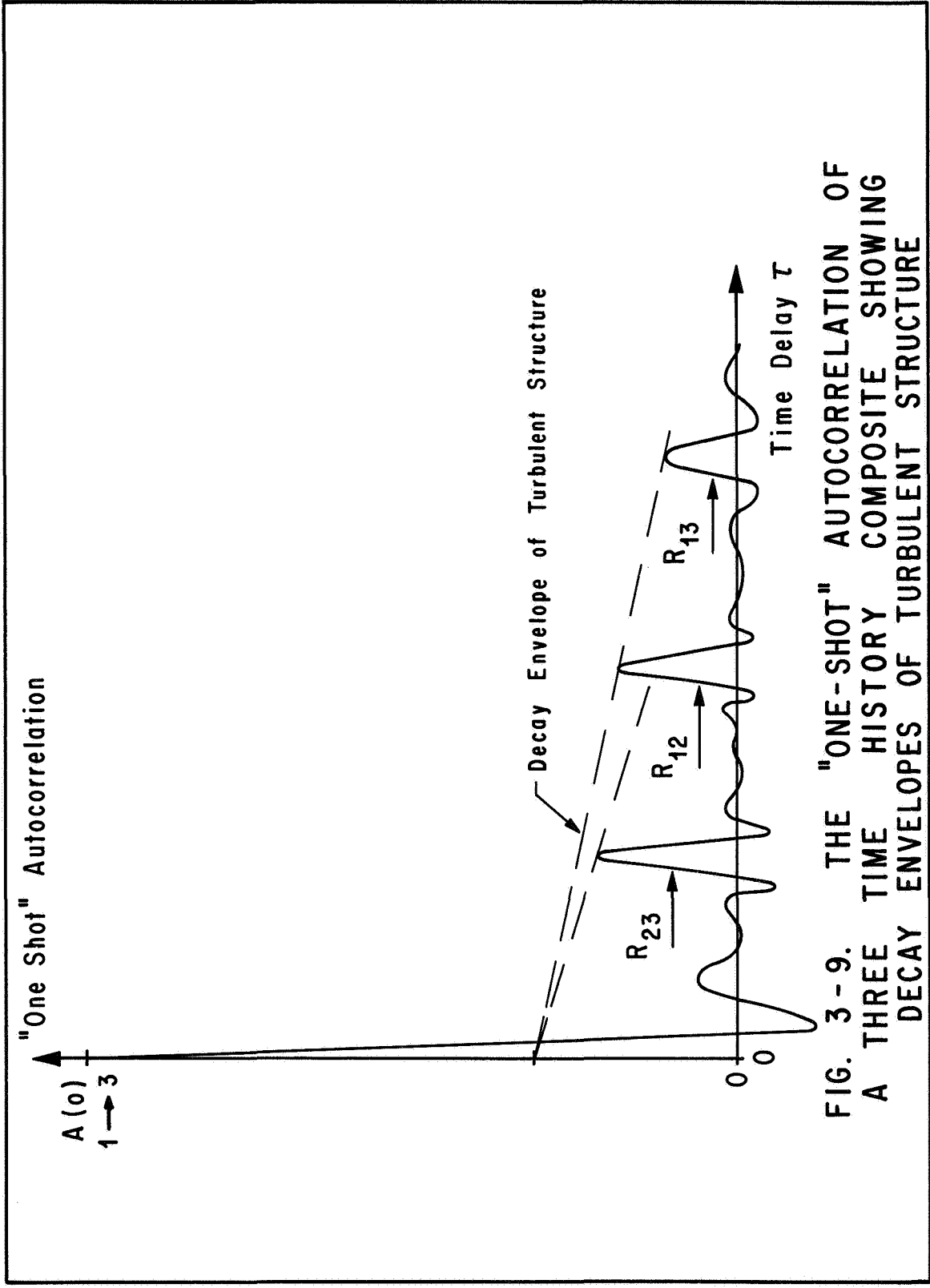


FIG. 3-9. THE "ONE-SHOT" AUTOCORRELATION OF A THREE TIME HISTORY COMPOSITE SHOWING DECAY ENVELOPES OF TURBULENT STRUCTURE

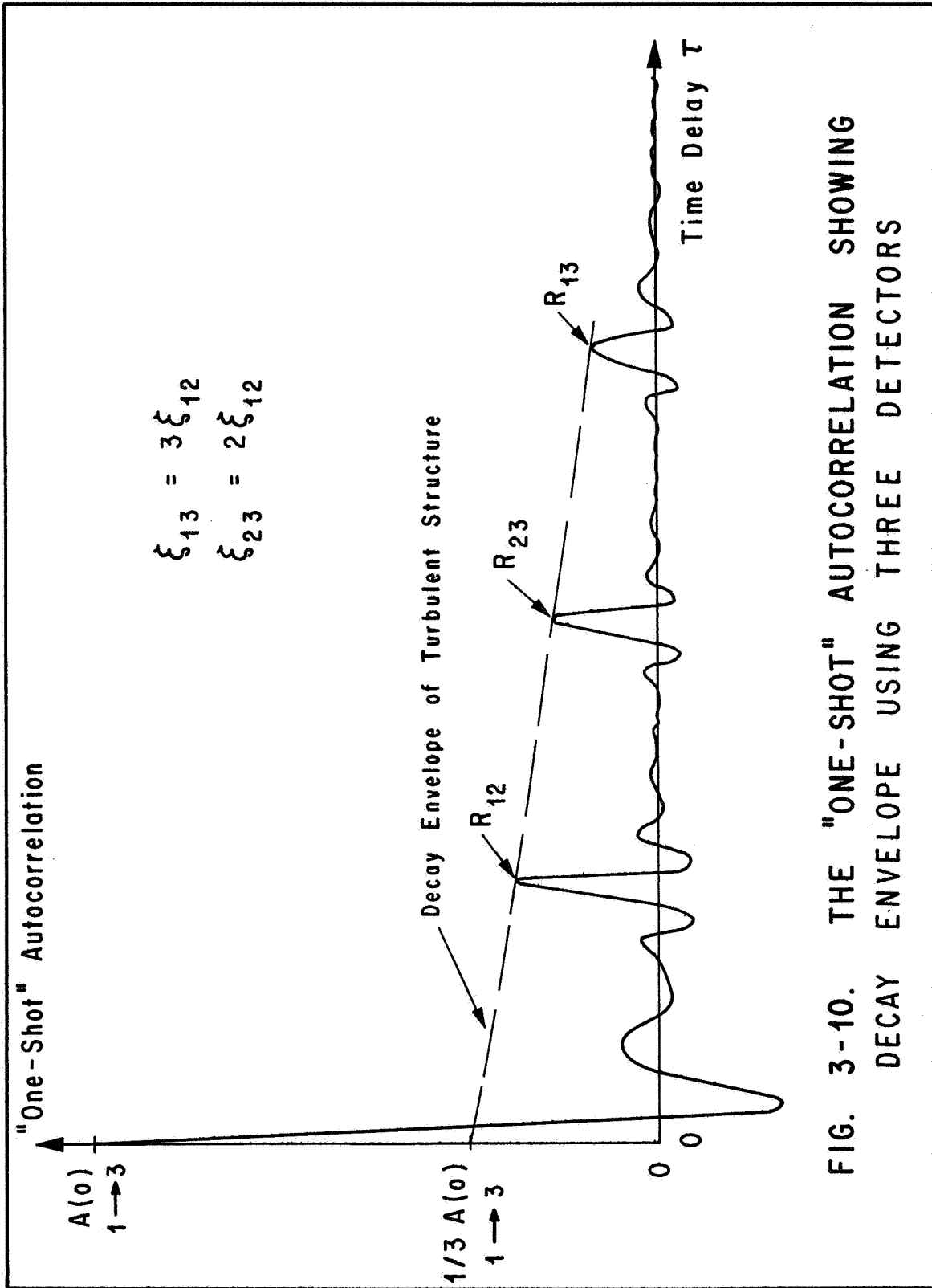


FIG. 3-10. THE "ONE-SHOT" AUTOCORRELATION SHOWING DECAY ENVELOPE USING THREE DETECTORS

Equation (58) can be represented more conveniently in terms of auto³ and cross-correlations, as was done previously.

$$A(\tau) \stackrel{\text{def}}{=} \sum_{i=1}^m \sum_{j=1}^m R_{ij}(\tau). \quad (59)$$

For the applications considered here,

$$R_{XY}(\tau) = R_{YX}(-\tau) = 0, \quad (60)$$

for $X > Y$, and

$$R_{XX}(\tau) = A_X(\tau), \quad (61)$$

where X and Y are particular values of i and j . Therefore,

$$A(\tau) = \sum_{i=1}^m A_i(\tau) + \sum_{i=1}^m \sum_{j=2}^m R_{ij}(\tau), \quad j > i. \quad (62)$$

Equation (62) is the general form of the "one-shot" autocorrelation for this particular type of application. For the present, assume that the beams have equal sensitivities, s , and that the zero time lag value of the individual autocorrelations of the $f_i(t)$'s are equal. Then,

$$A(0) = \sum_{i=1}^m A_i(0) = mA_X(0) \quad (63)$$

and

$$A_X(0) = \frac{1}{m} [A(0)]. \quad (64)$$

If it is further assumed that the signal-to-noise ratio approaches infinity as the beam separation approaches zero between the first beam and any one of the downstream beams (i.e., no noise when $\xi_{1j} = 0$), then the value of the "one-shot" autocorrelation is equal to the cross-correlation at $\tau = 0$.

$$A_X(0) = R_{XY}(\tau = 0, \xi_{XY} = 0). \quad (65)$$

For this particular case, the curve representing the trace of peaks as a function of τ on the "one-shot" autocorrelogram (i.e., the curve representing the rate of turbulence decay) will pass through the point

$$\left[\tau = 0, \frac{1}{m} A(0) \right].$$

$l \rightarrow m$

This value, at $\tau = 0$, is an upper limit and must decrease as the signal-to-noise ratio decreases, because, at $\tau = 0$ on any autocorrelogram, the noise is correlated as strong as the signal.

3.2.5 Time Delays and Zoning of the "One-Shot" Autocorrelogram

Overlapping of regions of correlation on the "one-shot" autocorrelogram prohibits certain combinations of beam separations and limits the minimum separation between any two of the beams. There is a solution to the overlapping problem referred to herein as the method of induced time delay. Electronic time delay techniques are employed in many fields. In this report, there are three purposes of the induced time delay: (1) to avoid peak interference on the "one-shot" correlogram, (2) to identify a correlation peak partially lost in correlated noise, and (3) to zone the "one-shot" auto- or cross-correlogram, thereby providing means for identifying particular pairs of signals associated with a particular correlation peak on a "one-shot" auto- or cross-correlogram.

With respect to (1) above, figure 3-11A shows a "one-shot" autocorrelogram where the measurement was made with two parallel laser beams separated by 1.90 inches in Mach 2.0 flow. The beams were located in the turbulent boundary layer.

The effect of overlapping is clearly evident by comparing figure 3-11A with 3-11B. In figure 3-11B, a cross-correlation was made between the two beams which eliminate the overlapping problem when only two beams were used.

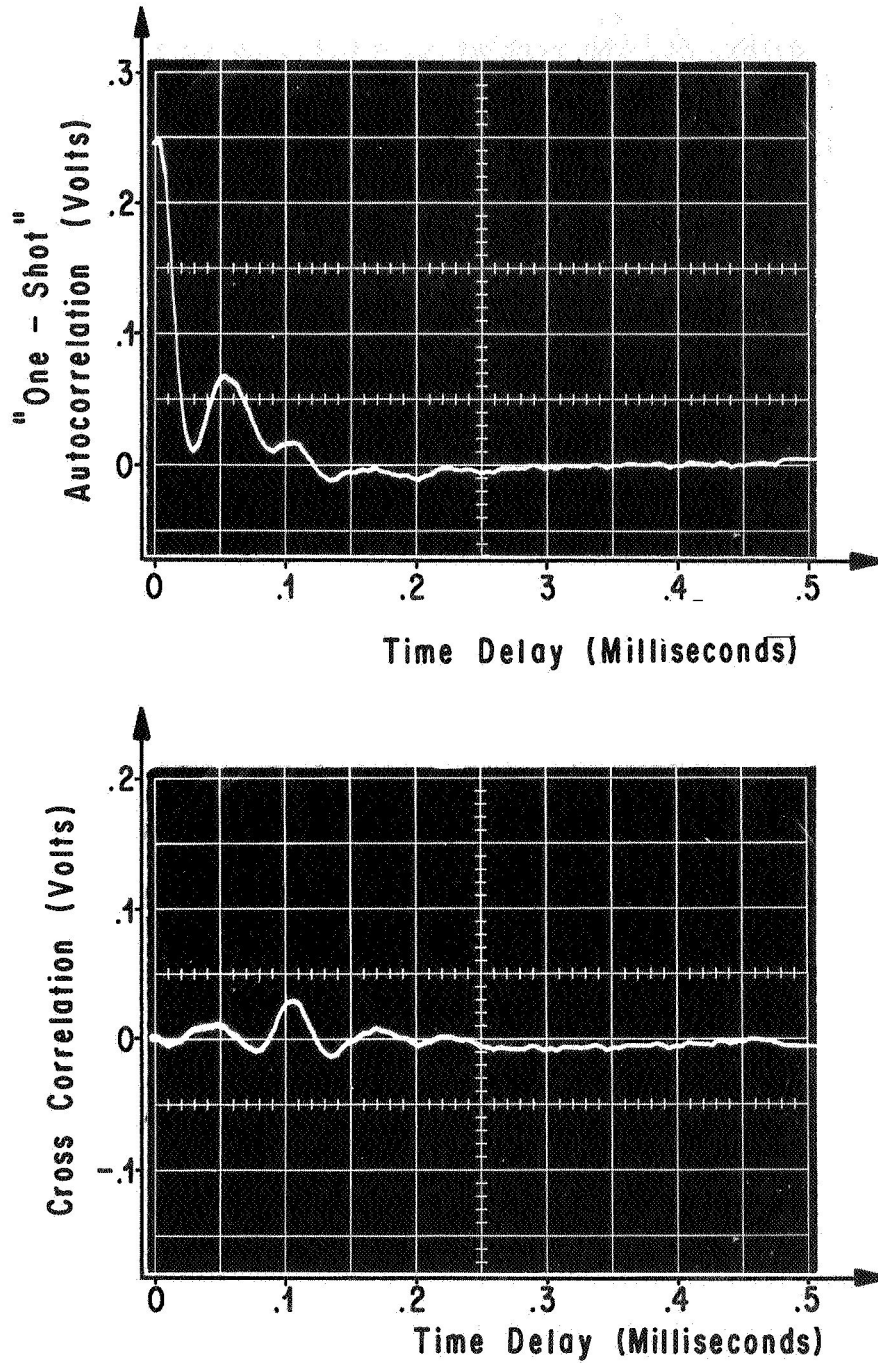


FIG. 3-11. A(TOP): "ONE-SHOT" AUTOCORRELATION OF TWO SIGNALS ADDED. B(BOTTOM): CROSS-CORRELATION OF SIGNAL ONE WITH TWO.

There is a solution to the overlapping problem. If the second signal of figure 3-11A had been delayed by electronically introducing a known time delay, Δt , the peak at $\tau_m = 0.106$ ms would have occurred at $\tau'_m = \tau_m + \Delta t$. If a time delay of 0.100 ms had been introduced into the signal from the downstream beam, the "one-shot" autocorrelogram would have looked like the one shown in figure 3-12, which is a much more accurate correlogram from the standpoint of studying the non-zero time delay correlation.

In particular, induced time delays provide flexibility to the "one-shot" autocorrelation technique and extend its range of application. For example, the speed and direction of atmospheric ground winds can be theoretically determined by the "one-shot" autocorrelation method.

Figure 3-13 is a schematic diagram of an atmospheric wind detection system composed of six signals retrieved by optical remote sensing techniques. Five of the six detectors are arranged in a fan for the purpose of determining which signal from the fan is correlated strongest with the signal from an "up-wind" location. It is also desired to determine the time lag of maximum correlation. Ideally, this can be accomplished with the "one-shot" autocorrelation method using induced time delays of known value.

As shown in figure 3-13, the signals from the fan B, C, D, E, and F are each delayed electronically and then added together. The resulting signal is added to signal A. The "one-shot" autocorrelogram of the summed signal should, theoretically, appear as shown at the bottom of figure 3-13.

Induced time delays can be used to zone the "one-shot" autocorrelogram for the purpose of peak identification. If no time delays are introduced, the peaks would probably overlap. Even if no overlapping occurs, there would be doubt as to which signal from the fan produced a particular peak.

The induced time delay, Δt , is large compared to the expected transit time, τ_m . Since signals B, C, D, E, and F are delayed by Δt , $2\Delta t$, $3\Delta t$, $4\Delta t$ and $5\Delta t$ seconds, respectively, a peak resulting from correlation between signals A and B would be expected to occur at $\tau'_{ab} = \tau_m + \Delta t$. Likewise, for signals A and C, $\tau'_{ac} = \tau_m + 2\Delta t$, etc. Also, the induced time delay method provides a graphical relationship between wind direction and the abscissa of the "one-shot" autocorrelogram. It follows that by comparing the "one-shot" autocorrelograms of the same data but with different induced time delays, peak identification should be enhanced.

The induced time delay method of peak identification should apply just as well to cross-correlation, perhaps better.

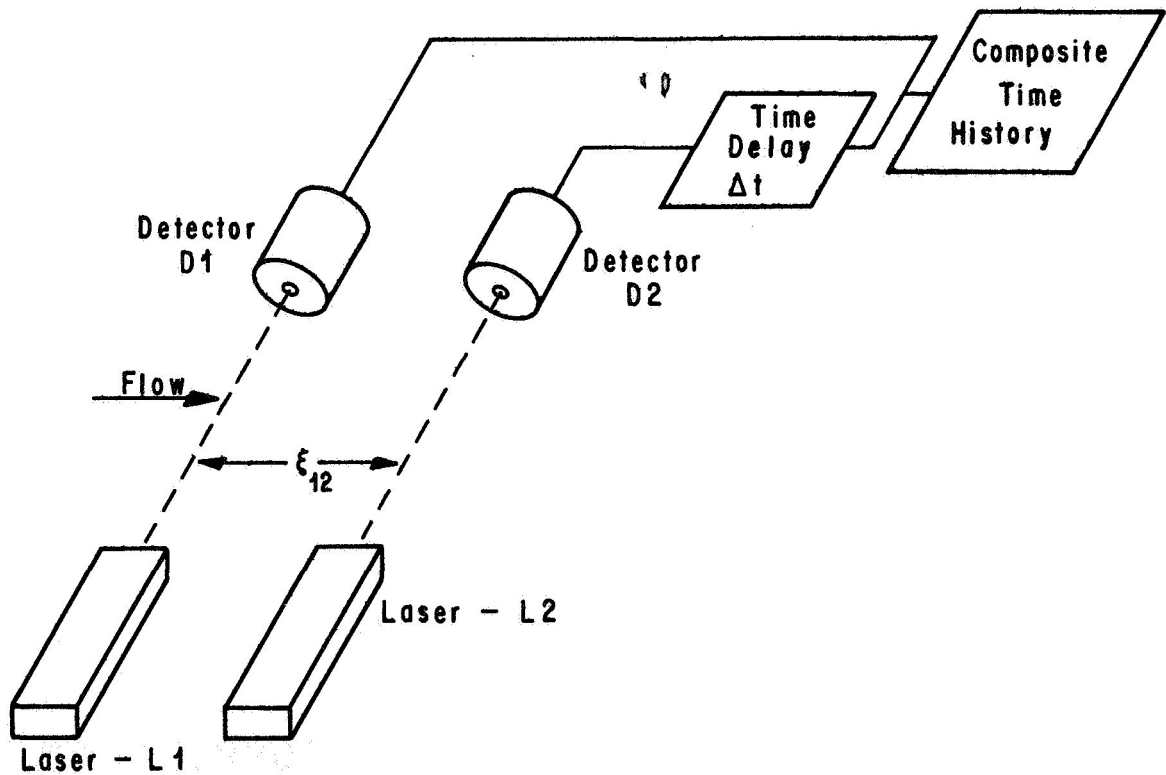
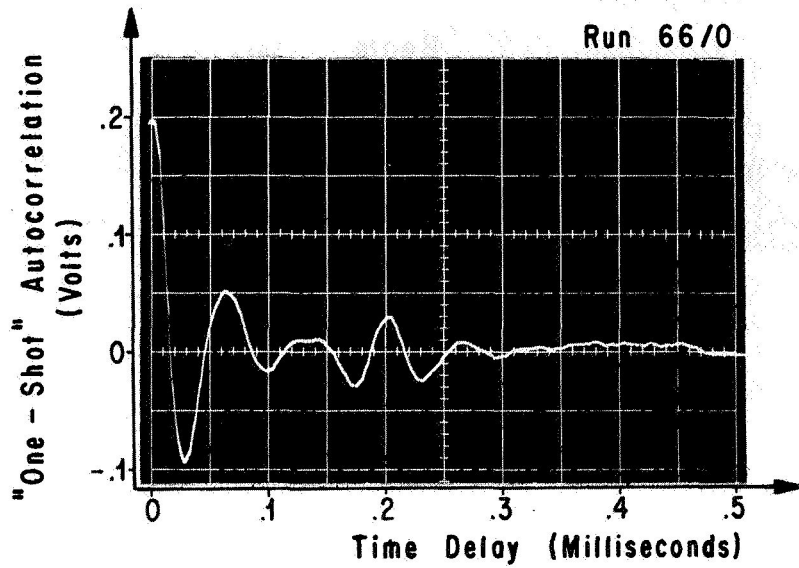


FIG. 3-12. "ONE-SHOT" AUTOCORRELATION WITH INDUCED TIME DELAY

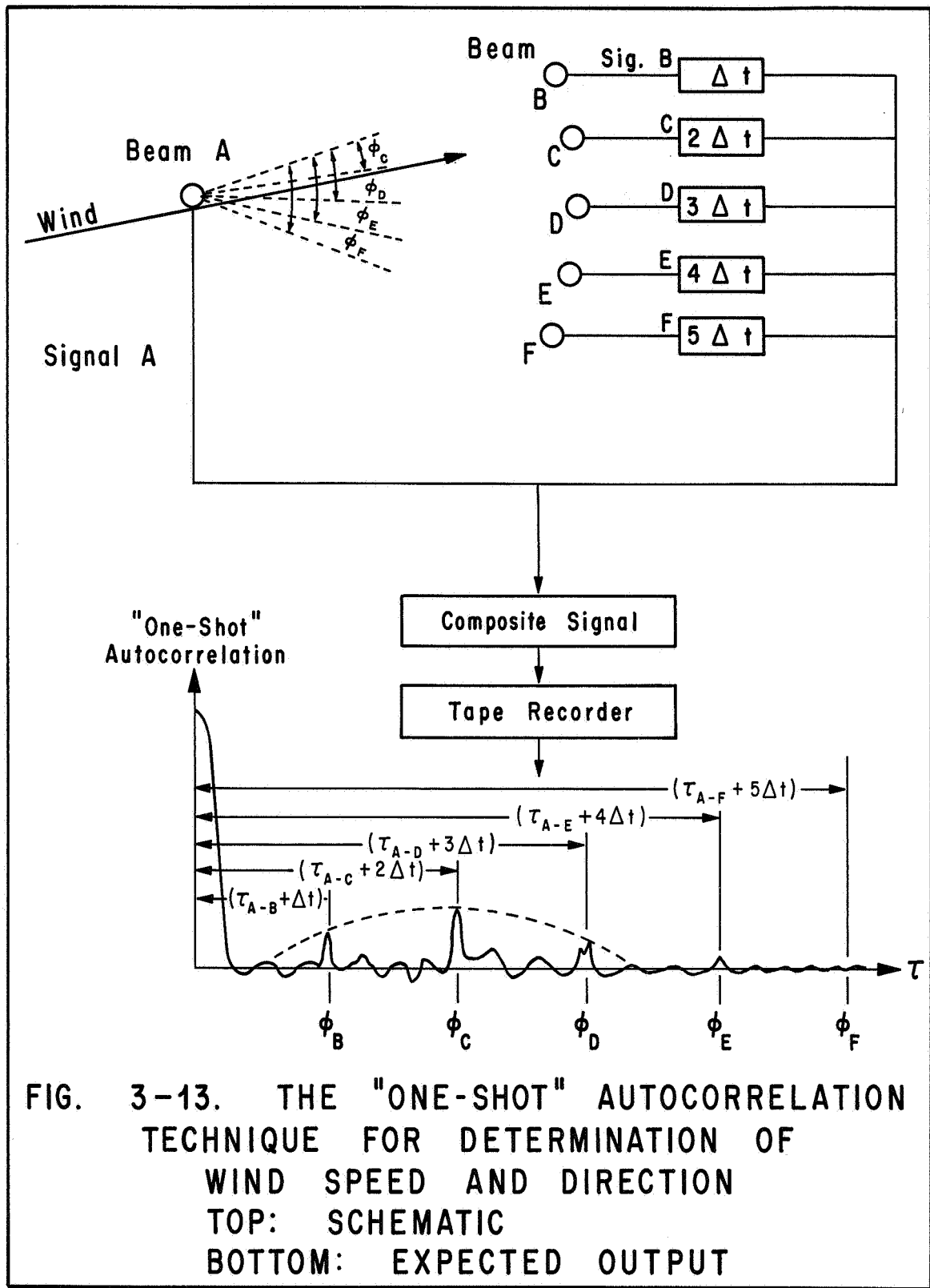


FIG. 3-13. THE "ONE-SHOT" AUTOCORRELATION TECHNIQUE FOR DETERMINATION OF WIND SPEED AND DIRECTION
 TOP: SCHEMATIC
 BOTTOM: EXPECTED OUTPUT

3.2.6 Noise Analysis*

The major disadvantage of the "one-shot" autocorrelation is that the noise-to-signal ratio, taken with respect to a particular time history contained in the composite, is greater than the noise-to-signal ratio of the particular time history taken separately. This is necessarily true, because, in a region on the autocorrelogram where two signals of a composite time history are correlated, all other signal and noise components represent noise in the computation. For applications where the noise-to-signal ratios of the individual time histories are large, the "one-shot" integration time may become very long to achieve the same accuracy as that obtained from the individual cross-correlations. However, this has not been proven experimentally.

In the following, let

n_a = noise-to-signal ratio of composite time history.

n = noise-to-signal ratio of individual time history.

m = number of time histories composing the composite time history.

i_c = instantaneous value of the composite time history.

i_k = instantaneous value of the k th individual time history ($k = 1, 2, \dots, m$).

i_{s_k} = instantaneous signal of i_k

i_{n_k} = instantaneous noise of i_k .

Assumptions:

- (1) The noise-to-signal ratio of the individual time histories are equal.
- (2) The rms value of the individual time histories are equal.
- (3) There is statistical stationarity.

*The conventional signal-to-noise ratio has been inverted here because the mathematics is simpler.

Derivation:

From the definitions, it follows that

$$i_c = i_1 + i_2 + i_3 + \dots + i_m = \sum_{k=1}^m i_k, \quad (66)$$

$\sqrt{\overline{i_c^2}}$ = rms value of composite time history,

$$\overline{i_c^2} = \frac{1}{T_a} \int_0^{T_a} (i_1 + i_2 + \dots + i_m)^2 dt, \quad (67)$$

$$\overline{i_c^2} = \overline{i_1^2} + \overline{i_2^2} + \dots + \overline{2i_1i_2} + \dots \quad (68)$$

The cross product terms approach zero as $T_a \rightarrow \infty$. Thus,

$$\overline{i_c^2} = \overline{i_1^2} + \overline{i_2^2} + \dots + \overline{i_m^2} = \sum_{k=1}^m \overline{i_k^2}. \quad (69)$$

If the noise-to-signal ratio is defined as the ratio of the rms noise in the composite to the rms value of the signal, then,

$$n_a = \left\{ \frac{\overline{i_c^2} - \overline{i_s^2}}{\overline{i_s^2}} \right\}^{1/2} \quad (70)$$

and

$$n_a = \left\{ \left(\overline{i_c^2} / \overline{i_s^2} \right) - 1 \right\}^{1/2}. \quad (71)$$

If the individual noise-to-signal ratio is defined as the ratio of the rms noise to the rms signal, taken with respect to the individual time histories, then

$$n = \left\{ \frac{\overline{i_n^2}}{\overline{i_s^2}} \right\}^{1/2} \quad (72)$$

and

$$n^2 = \frac{\overline{i_n^2}}{\overline{i_s^2}}. \quad (73)$$

Now substituting equation (69) into (71), we get

$$n_a = \left\{ \left(\frac{\overline{i_1^2} + \overline{i_2^2} + \dots + \overline{i_m^2}}{\overline{i_s^2}} \right) - 1 \right\}^{1/2}. \quad (74)$$

By assumption 2,

$$\sqrt{\overline{i_1^2}} = \sqrt{\overline{i_2^2}} = \sqrt{\overline{i_3^2}} = \dots = \sqrt{\overline{i^2}} \quad (75)$$

$$\overline{i_1^2} = \overline{i_2^2} = \overline{i_3^2} = \dots = \overline{i^2} \quad (76)$$

and

$$\overline{i^2} = \overline{i_{s_1}^2} + \overline{i_{n_1}^2} = \overline{i_{s_2}^2} + \overline{i_{n_2}^2} = \dots = \overline{i_s^2} + \overline{i_n^2}. \quad (77)$$

By assumptions 1 and 2,

$$\overline{i_{s_1}^2} = \overline{i_{s_2}^2} = \dots = \overline{i_s^2} \quad (78)$$

$$\overline{i_{n_1}^2} = \overline{i_{n_2}^2} = \dots = \overline{i_n^2}. \quad (79)$$

Substitution of equation (76) into (69) gives

$$\overline{i_c^2} = m \overline{i^2}, \quad (80)$$

and from equation (77), we see that

$$\overline{i^2} = \overline{i_s^2} + \overline{i_n^2}. \quad (81)$$

Replacing $\overline{i^2}$ in equation (80) by the expression in (81) yields

$$\overline{i_c^2} = m(\overline{i_s^2} + \overline{i_n^2}). \quad (82)$$

Substitute equation (82) into (71).

$$n_a = \left\{ m \left(1 + \frac{\overline{i_n^2}}{\overline{i_s^2}} \right) - 1 \right\}^{1/2}. \quad (83)$$

Substitute equation (73) into (83).

$$n_a = \left\{ m(1 + n^2) - 1 \right\}^{1/2}. \quad (84)$$

Equation (84) is the rms noise-to-signal ratio of a composite time history taken with respect to one of the individual signals and expressed as a function of the rms noise-to-signal ratio of the individual signal.

The power noise/signal ratio of the composite time history is

$$n_{pa} = n_a^2. \quad (84a)$$

The power noise/signal ratio of an individual time history is

$$n_p = n^2. \quad (84b)$$

Then, from equation (84), we see that

$$n_{pa} = m(1 + n_p) - 1. \quad (84c)$$

In figure 3-14, n_a is plotted versus m for several values of n . For large values of n ,

$$n_a \doteq \sqrt{m} n. \quad (85)$$

For the range of values plotted in figure 3-14, equation (85) is not a bad approximation even for $n = 4$, $m = 2$. For $n = 0$, which corresponds to the case where there is no noise in the individual time histories,

$$n_a = \sqrt{m} - 1. \quad (86)$$

It is seen from equation (86) that the minimum noise-to-signal ratio of the composite time history is unity.

The practical limitation is not set by the increase in noise-to-signal ratio directly; rather, it is the increase in integration time required to obtain the same results that would be obtained by calculating the individual cross-correlations with equal confidence levels. The increase in integration time can be described as the ratio of T_a to T . Here, T_a is the integration time required to compute the "one-shot" autocorrelation and T is the integration time required to compute a cross-correlation between two of the individual time histories. The relationship is*

$$\frac{T_a}{T} = m^2 - \frac{m^2 - 1}{(n^2 + 1)^2 + 1}. \quad (87)$$

*This relationship is obtained from reference 6. The n used in the reference is the square of the n used here.

Note:
rms Values And Noise-to-Signal Ratios of The
Individual Time Histories Are Assumed Equal.

Ratio of Noise-to-Signal of
a Composite Time History, n_0

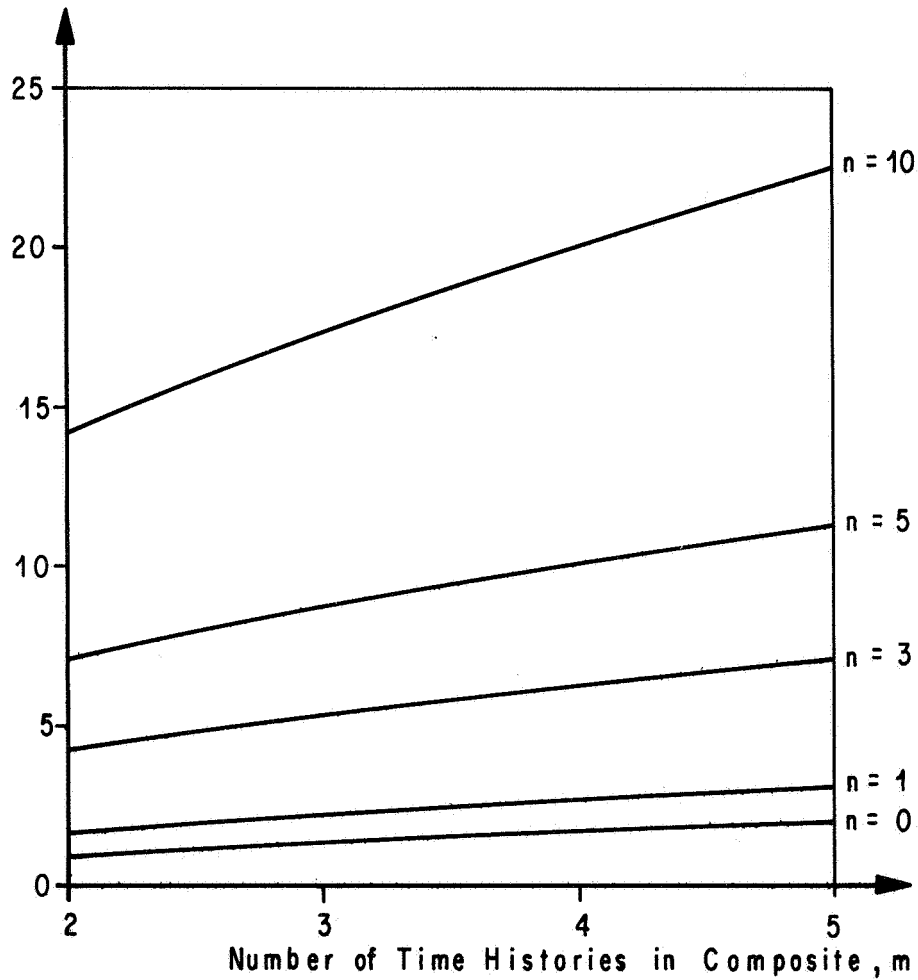


FIG. 3-14. NOISE-TO-SIGNAL RATIO OF A COMPOSITE
VERSUS
NUMBER OF TIME HISTORIES ADDED

In figure 3-15, the functional relationship between T_a/T , m , and n is shown. From this figure the following observations can be made:

- (1) The minimum value of T_a is

$$T_a = (2.5)T,$$

which corresponds to the case of adding two identical signals to form the composite, i.e., $n = 0$, $m = 2$. However, for this case, T is also a minimum. Therefore, adding two, three, or four such signals should be considered practical. Verification of this has already been presented for $m = 2$ and $m = 3$.

- (2) The percentage of increase in integration time due to adding time histories with noise-to-signal ratios, n , equal to or greater than three ($n \geq 3$) is essentially the same for fixed m . That is, to a good approximation,

$$\frac{T_a}{T} = m^2, \quad \text{for } n \geq 3.$$

- (3) The limits T_a/T are

$$\frac{m^2 + 1}{2} \leq \frac{T_a}{T} \leq m^2.$$

The increase in the required integration time, then, represents a very important limitation upon the practical application of the "one-shot" autocorrelation method. There is, however, another limitation that is not so critical. This is the increase in computation time.

The ratio of computation times is given by

$$\gamma_a = \frac{T_a}{(\text{number of peaks}) \cdot T}. \quad (88)$$

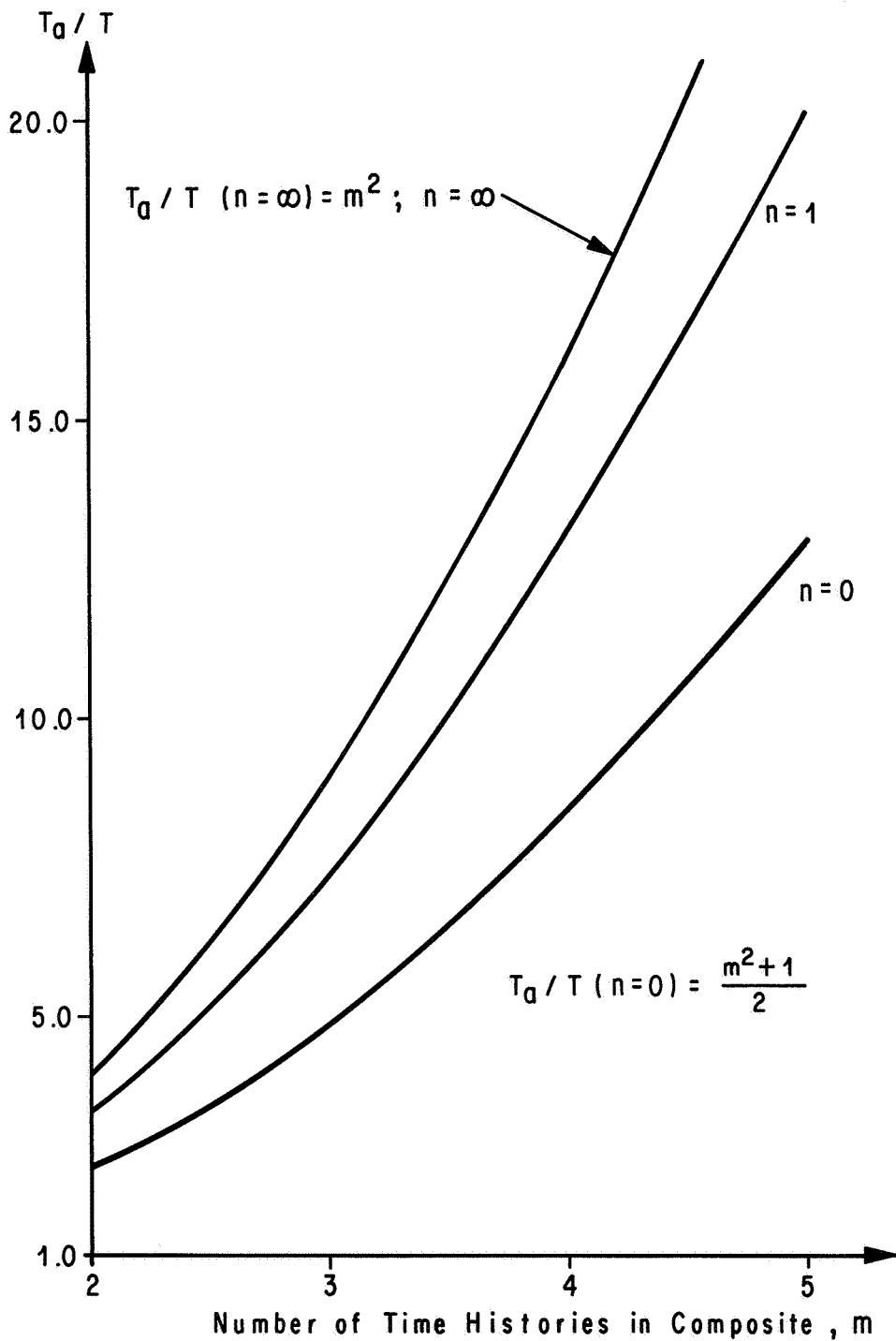


FIG. 3-15. INCREASE IN INTEGRATION TIME FOR A COMPOSITE TIME HISTORY VERSUS NUMBER OF TIME HISTORIES IN COMPOSITE

As explained in section 3.2.3, the number of peaks on the "one-shot" autocorrelogram is

$$\text{number of peaks} = 1 + \sum_{k=1}^m (m - k). \quad (56)$$

The ratio of computation times is

$$\gamma_a = \left[\frac{1}{1 + \sum_{k=1}^m (m - k)} \right] \frac{T_a}{T}. \quad (89)$$

Thus,

$$\gamma_a = \left\{ \frac{2}{m(m - 1) + 2} \right\} \frac{T_a}{T} \quad (90)$$

which has upper and lower limits:

$$\frac{(m^2 + 1)}{m(m - 1) + 2} \cong \gamma_a \cong \frac{2m^2}{m(m - 1) + 2}. \quad (91)$$

In figure 3-16, γ_a is plotted versus m . This figure represents the case where all peaks of the "one-shot" autocorrelogram are considered as useful data.

3.3 The "One-Shot" Cross-Correlation

3.3.1 Statement of the Concept

The second kind of "one-shot" correlation technique is the "one-shot" cross-correlation, which is described in the following statement:

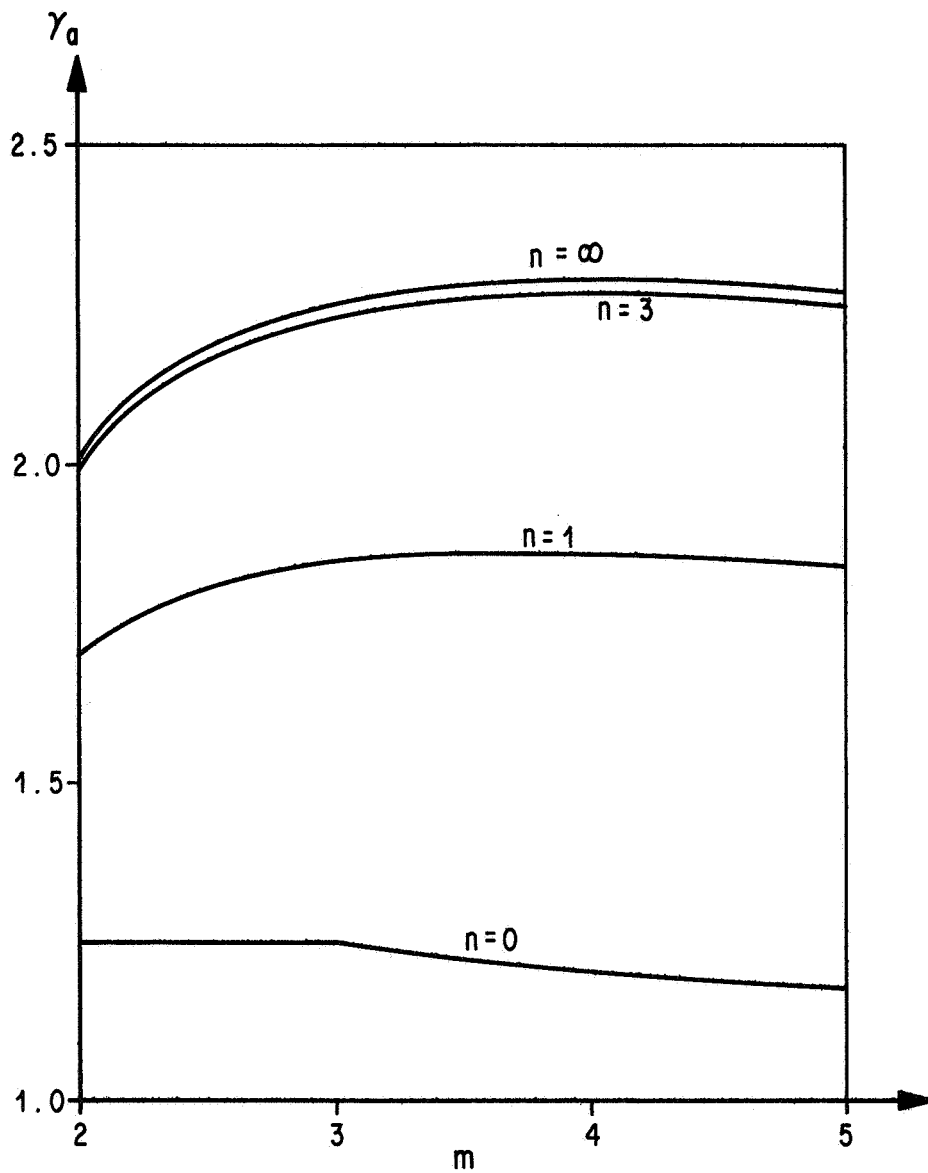


FIG. 3-16 RATIO OF COMPUTATION TIME (γ_a)
 VERSUS
 NUMBER OF TIME HISTORIES IN COMPOSITE (m)

- The cross-correlation of a single time history with a composite time history, the single time history containing a random signal that is statistically correlated to two or more random signals contained in the composite, will result in a cross-correlogram exhibiting peaks of cross-correlation between the signal in the separate time history and each of the signals in the composite, the signals in the composite sufficiently lagging one another in time.

The differences between the "one-shot" autocorrelation and the "one-shot" cross-correlation are as follows: (1) The "one-shot" cross-correlogram does not have the large peak at zero time delay representing the mean square value of the composite signal, and (2) the peaks resulting from correlations between all possible pairs, other than those pairs formed between the signal in the separate time history and each of those in the composite, are not present on the "one-shot" cross-correlogram.

These differences represent a loss of information. There are cases, however, where it is desirable to eliminate this additional computation. For example, when the noise-to-signal ratio of the individual time histories of a composite used in computing a "one-shot" autocorrelation are large, usually the error in evaluating the zero time delay point on the eddy decay curve is large. Also, the required integration time may be very long. In such a case, a considerable advantage can be gained by using the "one-shot" cross-correlation. The advantages are (1) lower noise-to-signal ratio and, therefore, a shorter required integration time, and (2) the capability to compute the cross-correlation peak at zero time delay directly without an electrically induced time delay, which is necessary with the "one-shot" autocorrelation.

3.3.2 Mathematical Development

In the following, consider the cross-correlation of a single time history, $f_0(t)$, with a composite time history, $F(t)$. $F(t)$ is composed of m individual time histories, such that

$$F(t) = \sum_{k=1}^m f_k(t). \quad (92)$$

Assume that each time history in $F(t)$ and $f_0(t)$ represents random time histories and that each can be expressed as the sum of signal plus noise

where a signal in $F(t)$ represents that portion of a time history which is correlated to the signal of $f_o(t)$. Then,

$$f_o(t) = f_{s_o}(t) + f_{n_o}(t) \quad (93)$$

$$F(t) = \sum_{k=1}^m [f_{s_k}(t) + f_{n_k}(t)]. \quad (94)$$

Furthermore, assume for each $f_k(t)$ that

$$\overline{f_k(t)} = \lim_{T \rightarrow \infty} \frac{1}{T} \int_0^T f_k(t) dt = 0 \quad (95)$$

and

$$\overline{f_o(t)} = \lim_{T \rightarrow \infty} \frac{1}{T} \int_0^T f_o(t) dt = 0. \quad (96)$$

The "one-shot" cross-correlation of $f_o(t)$ with $F(t)$ is defined as

$$R(\tau) = \lim_{l \rightarrow m} \frac{1}{T_c} \int_0^{T_c} f_o(t) \cdot F(t + \tau) dt \quad (97)$$

and

$$R(\tau) = \lim_{l \rightarrow m} \frac{1}{T_c} \int_0^{T_c} f_o(t) \cdot \sum_{k=1}^m f_k(t + \tau) dt. \quad (98)$$

It is assumed that T_c is sufficiently long, such that

$$R(\tau) = \frac{1}{T_c} \int_0^{T_c} f_o(t) \cdot \sum_{k=1}^m f_k(t + \tau) dt \quad (99)$$

is a good approximation to equation (98).

Substitute equations (93) and (94) into (99).

$$R(\tau) = \frac{1}{T_c} \int_0^{T_c} [f_{s_o}(t) + f_{n_o}(t)] \cdot \sum_{k=1}^m [f_{s_k}(t + \tau) + f_{n_k}(t + \tau)] dt. \quad (100)$$

Performing the indicated multiplication and taking the summation outside the integral, we obtain

$$R(\tau) = \sum_{k=1}^m \frac{1}{T_c} \left[\int_0^{T_c} f_{s_o}(t) \cdot f_{s_k}(t + \tau) dt + \int_0^{T_c} f_{s_o}(t) \cdot f_{n_k}(t + \tau) dt \right. \\ \left. + \int_0^{T_c} f_{n_o}(t) \cdot f_{s_k}(t + \tau) dt + \int_0^{T_c} f_{n_o}(t) \cdot f_{n_k}(t + \tau) dt \right]. \quad (101)$$

The last three integrals on the right-hand side of equation (101) are approximately zero because the time-average value of the products of signals with noise, and noise with noise are zero; i.e., the noise component of $f_o(t)$ is not correlated with the signal and noise components in the composite, $F(t)$.

Equation (101) reduces to

$$R(\tau) = \sum_{k=1}^m \frac{1}{T_c} \int_0^{T_c} f_{s_o}(t) \cdot f_{s_k}(t + \tau) dt. \quad (102)$$

The summation in equation (102) represents the sum of the cross-correlations of the single time history $f_o(t)$ with each of the time histories in the composite evaluated at the same time delay, τ .

$$R(\tau) = \sum_{l \rightarrow m} \sum_{k=1}^m R_{ok}(\tau), \quad (103)$$

where the subscripts, $()_{ok}$, indicate the signals cross-correlated, as well as the order of the cross-correlation.

If it is assumed that the signals in the composite are introduced sequentially such that each signal in time lags the previous signal sufficiently to avoid peak interference, the "one-shot" cross-correlation expressed in equation (103) becomes

$$R(\tau_{oj}) = R_{oj}(\tau_{oj}), \quad (104)$$

$l \rightarrow m$

where τ_{oj} is the time delay corresponding to the peak of the cross-correlation $R_{oj}(\tau_{oj})$ between $f_o(t)$ and $f_j(t + \tau)$ in the composite. All other cross-correlations in equation (103) evaluated at τ_{oj} are zero by the assumption that overlapping does not occur.

$$\sum_{\substack{k=1 \\ k \neq j}}^m R_{ok}(\tau_{oj}) = 0. \quad (105)$$

Therefore, the "one-shot" cross-correlogram will be composed of as many peaks as there are time histories in the composite, each of which contains a random signal statistically correlated to the random signal in $f_o(t)$.

$$\text{number of peaks} = m. \quad (106)$$

The time delay between the k th and $(k+1)$ peaks is $\tau_{o,k+1} - \tau_{o,k}$, which is sufficient to avoid overlapping.

3.3.3 Experimental Verification

In figure 3-17, three laser beams, parallel to each other and normal to the mean flow direction, are directed through the turbulent boundary layer on a thin plate. The free-stream Mach number is approximately 2.0. The beams form a plane that differs only slightly from a plane parallel to the surface of the plate. Beam 1 from the upstream laser passes through the boundary layer, and a knife-edge blocks approximately 50 percent of the laser light, preventing it from reaching the photodiode. The uninterrupted portion of the beam is monitored by the photodetector A. The fluctuations of the laser beam perpendicular to the knife-edge causes fluctuations in the amount of light monitored by the photodiode which converts these fluctuations into an ac-electrical signal.

The downstream laser beam is split into two beams of equal power. Beam 3 passes directly through the boundary layer. Beam 2 is reflected upstream and then through the boundary layer at a location which is 2.32 inches upstream of beam 3 and 2.63 inches downstream from beam 1. After beam 2 passes through the boundary layer, it is reflected downstream. Beams 2 and 3 are added optically by monitoring both beams with the same photodetector B. The fluctuations of beams 2 and 3 are retrieved by use of a knife-edge in the manner described from beam 1.

The cross-correlation of the time history monitored by detector A, with the composite time history monitored by detector B, is shown in figure 3-7 (lower right). The two peaks predicted by the "one-shot" cross-correlation theory are clearly evident and provide strong experimental support to its validity.

In order to compare the "one-shot" cross-correlogram obtained above with the "one-shot" autocorrelogram calculated from a composite of the same three time histories, the output of detector A was electronically added to the output of detector B, and the autocorrelation of the composite was computed as a function of time delay. This "one-shot" autocorrelogram is shown in figure 3-17 (upper right). The structure of this "one-shot" autocorrelogram was previously discussed in section 3.2.3.

In figure 3-18, a "one-shot" cross-correlation is shown with three beams in the composite time histories. During this particular run, the second beam in the composite was not positioned on the knife-edge. Instead, it was located on the edge of the photodiode opposite to the knife-edge (in the downstream direction). Thus, the edge of the photodiode performed the same function as the knife-edge, except the sign of the signal was reversed. This inverted the second peak on the "one-shot" cross-correlogram and demonstrates the schlieren principle very well.

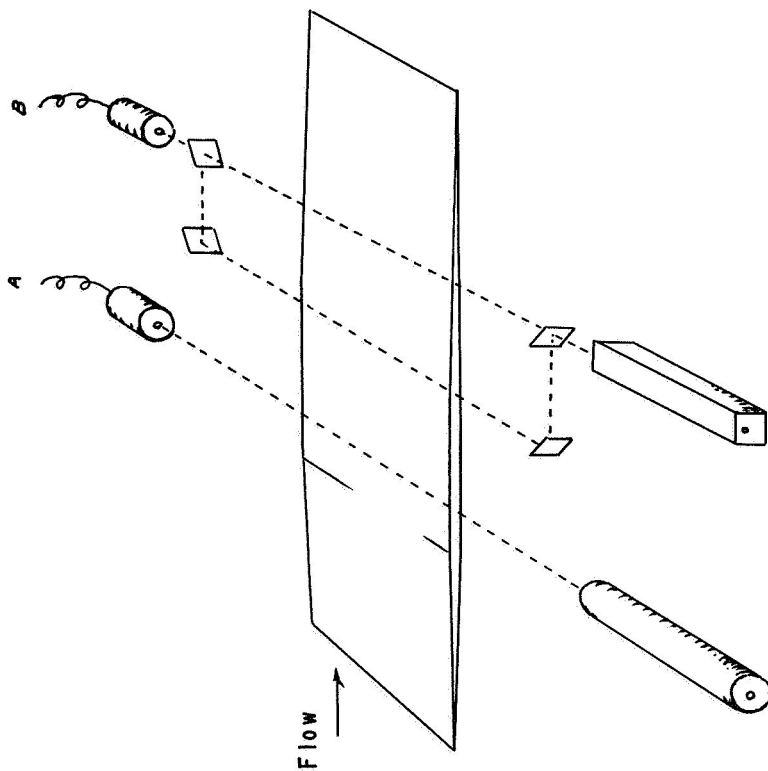
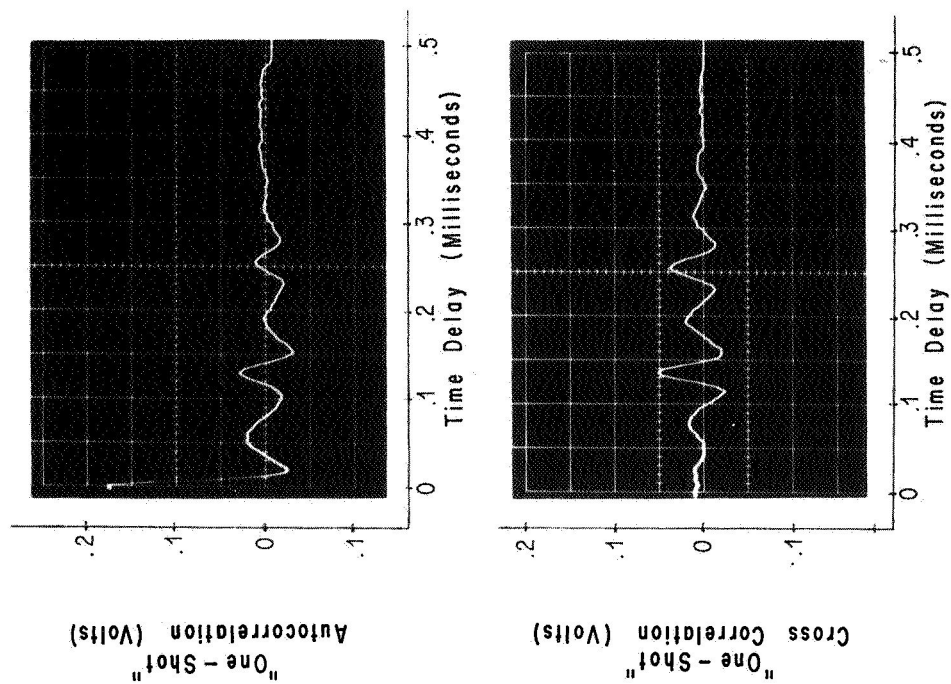


FIG. 3-17. "ONE - SHOT" CORRELATION PROFILES
 MEASURED IN A SUPERSONIC TURBULENT
 BOUNDARY LAYER

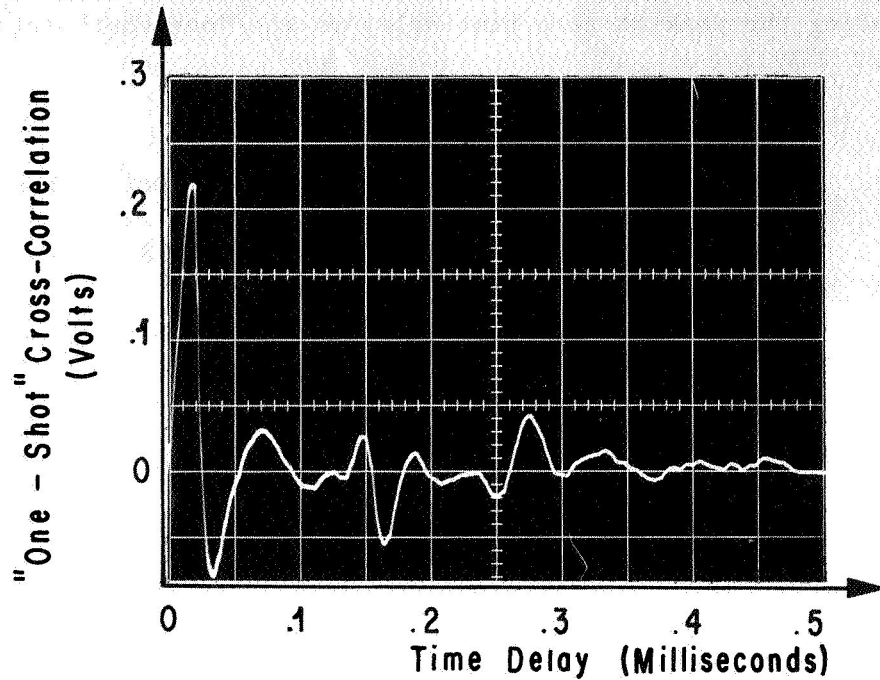


FIG. 3-18. "ONE-SHOT" CROSS-CORRELOGRAM WITH THREE TIME HISTORIES IN THE COMPOSITE. SIGN OF SECOND SIGNAL WAS NEGATIVE

3.3.4 Noise Analysis

For the same individual time histories the integration time required to compute the "one-shot" cross-correlation would be less than the integration time required to compute the "one-shot" autocorrelation, both having the same number of peaks on their correlograms (excluding the peak at zero time delay on the "one-shot" autocorrelogram).

In the following, we let

T_c = integration time for a "one-shot" cross-correlation.

n = rms noise/signal ratio of a signal in a composite time history.

$i_o(t)$ = instantaneous value of the independent time history.

$i_c(t)$ = instantaneous value of the composite time history.

m = number of beams in the composite time history.

$i_k(t)$ = instantaneous value of the k th individual time history in the composite.

T = integration time required to compute the cross-correlation between the independent time history and one of the time histories in the composite.

The rms noise/signal ratio of i_o is defined as

$$n_o \triangleq \left(\frac{\overline{i_{no}^2}}{\overline{i_{so}^2}} \right)^{1/2}, \quad (107)$$

and from section 3.2, the noise-to-signal ratio for a signal in a composite is

$$n_c = [m(1 + n^2) - 1]^{1/2}. \quad (108)$$

In equation (108), it has been assumed that the noise-to-signal ratio, n , and the mean squared values of the individual time histories in the composite are equal. Also, statistical stationarity is assumed.

The ratio of integration times is

$$\frac{T_c}{T} = \frac{n_c^2 n^2 + n_c^2 + n^2 + 2}{n^4 + 2n^2 + 2}. \quad (109)$$

It has been assumed in equation (109) that the noise-to-signal ratio and mean squared value of the independent time history, i_o , are equal to those of an individual time history in the composite; i.e.,

$$n_o = n \quad (110)$$

$$\overline{i_o^2} = \overline{i_k^2}. \quad (111)$$

Rearranging equation (109) yields

$$\frac{T_c}{T} = 1 + \left[\frac{(n^2 + 1)}{(n^2 + 1)^2 + 1} \right] (n_c^2 - n^2). \quad (112)$$

Substituting equation (108) into (112) and rearranging gives

$$\frac{T_c}{T} = 1 + \left[\frac{(n^2 + 1)^2}{(n^2 + 1) + 1} \right] (m - 1) \quad (113)$$

or

$$\frac{T_c}{T} = m - \frac{(m - 1)}{(n^2 + 1)^2 + 1}. \quad (114)$$

The upper limit of equation (114) is

$$\lim_{n \rightarrow \infty} (T_c/T) \rightarrow m \quad (115)$$

and the lower limit is

$$\lim_{n \rightarrow 0} (T_c/T) \rightarrow \frac{m+1}{2}, \quad (116)$$

or

$$\frac{m+1}{2} \cong \frac{T_c}{T} \cong m. \quad (117)$$

Equation (114) shows that for $n \geq 3$ the ratio of integration times (T_c/T) is, to a very good approximation, equal to the number of individual time histories in the composite:

$$\frac{T_c}{T} \doteq m; \quad \text{for } n \geq 3. \quad (118)$$

In figure 3-19, T_c/T is plotted versus m for various values of n .

From equation (56) in section 3.2.3, the number of peaks on a "one-shot" autocorrelogram are (excluding the peak at $\tau = 0$)

$$\text{number of peaks} = \sum_{k=1}^m (m_a - k) \quad (119)$$

$$P_a = \frac{1}{2} (m_a^2 - m_a). \quad (120)$$

The number of peaks on the "one-shot" cross-correlogram are

$$P_c = m_c. \quad (121)$$

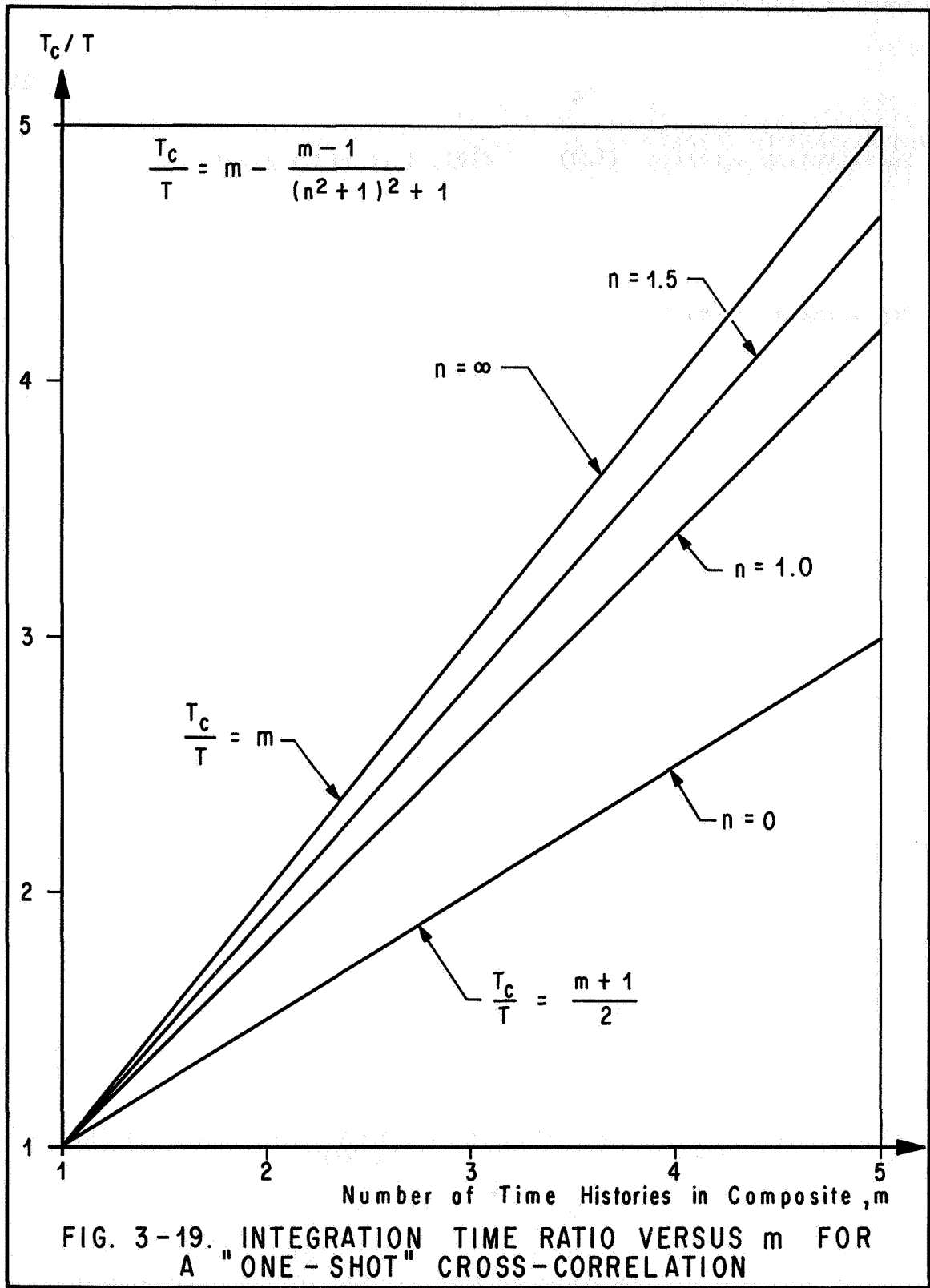


FIG. 3-19. INTEGRATION TIME RATIO VERSUS m FOR A "ONE-SHOT" CROSS-CORRELATION

However, for comparison purposes, it should be required that

$$P_c = P_a. \quad (122)$$

Substituting equations (120) and (121) into (122) gives

$$m_c = \frac{1}{2} (m_a^2 - m_a). \quad (123)$$

Replacing m in equation (87) with m_a , we obtain

$$\frac{T_a}{T} = m_a^2 - \frac{m_a^2 - 1}{(n^2 + 1)^2 + 1}, \quad (124)$$

which is the "one-shot" autocorrelation integration time ratio. Replacing m in equation (114) with m_c , we obtain

$$\frac{T_c}{T} = m_c - \frac{m_c - 1}{(n^2 + 1)^2 + 1}. \quad (125)$$

Dividing equation (124) by (125) yields

$$\frac{T_a}{T_c} = \frac{m_a^2(n^2 + 1)^2 + 1}{m_c(n^2 + 1)^2 + 1}, \quad (126)$$

and substituting equation (123) into (126) yields

$$\frac{T_a}{T_c} = \frac{2m_a^2(n^2 + 1)^2 + 2}{m_a(m_a - 1)(n^2 + 1)^2 + 2}. \quad (127)$$

From equation (127), the following conclusions can be drawn:

- (1) The lower limit of the integration time ratio is

$$\lim_{n \rightarrow 0} (T_a/T_c) \rightarrow \frac{2m_a^2 + 2}{m_a(m_a - 1) + 2} \cdot \quad (128)$$

- (2) The upper limit is

$$\lim_{n \rightarrow \infty} (T_a/T_c) \rightarrow \frac{2m_a}{m_a - 1} \cdot \quad (129)$$

- (3) The integration time required for the "one-shot" autocorrelation is always longer than that required for the "one-shot" cross-correlation. The minimum value occurs in the limit as $m_a \rightarrow \infty$ and is equal to 2.

$$\left(\frac{T_a}{T_c}\right)_{\min} = \lim_{m_a \rightarrow \infty} (T_a/T_c) \rightarrow 2.$$

- (4) The maximum value of T_a/T corresponds to the limit as $n \rightarrow 0$ for $m_a = 3$ and is equal to 3.

$$\left(\frac{T_a}{T_c}\right)_{\max} = \lim_{\substack{n \rightarrow 0 \\ m_a=3}} (T_a/T_c) \rightarrow 3.$$

- (5) For comparison purposes, the minimum value of m_a is 3 because the "one-shot" autocorrelogram for $m_a = 2$ has only one peak, other than that at $\tau = 0$, and the corresponding "one-shot" cross-correlation reduces to the standard cross-correlation. By equation (123), $m_c = 1$ for $m_a = 2$. These equalities imply that there is only one time history in the composite of the "one-shot" cross-correlation.)

- (6) The upper limit is approached rapidly as n increases.
For $n \geq 3$,

$$\frac{T_a}{T_c} = \frac{2m_a}{m_a - 1} ; \quad n \geq 3 \quad (130)$$

with less than one percent error.

- (7) The range of T_a/T_c is

$$2.50 \leq \frac{T_a}{T_c} \leq 3.00$$

for all combinations of n 's and m_a 's between the limits defined below.

$$0 \leq n \leq \infty$$

$$3 \leq m_a \leq \infty .$$

Therefore, the required integration time for a "one-shot" autocorrelation is 250 to 300 percent longer than that required for a "one-shot" cross-correlation. This statement is, of course, restricted to the assumptions made above.

In figure 3-20, T_a/T_c is plotted versus m_a for several values of n . If the power noise-to-signal ratio had been used in the analysis in place of the rms noise-to-signal ratio, conclusion (3) would have been the only one affected ($n \geq 3$ would have been $n_p \geq 9$ since $n_p = n^2$).

The ratio of the computation time required for the "one-shot" cross-correlation, T_c , to that required for m number of separate cross-correlations (one for each peak on the "one-shot" correlogram) is

$$\gamma_c = \frac{T_c}{mT} = 1 - \frac{m - 1}{m[(n^2 + 1)^2 + 1]} . \quad (131)$$

The lower limit is

$$\lim_{n \rightarrow 0} (\gamma_c) \rightarrow \frac{m + 1}{2m} , \quad (132)$$

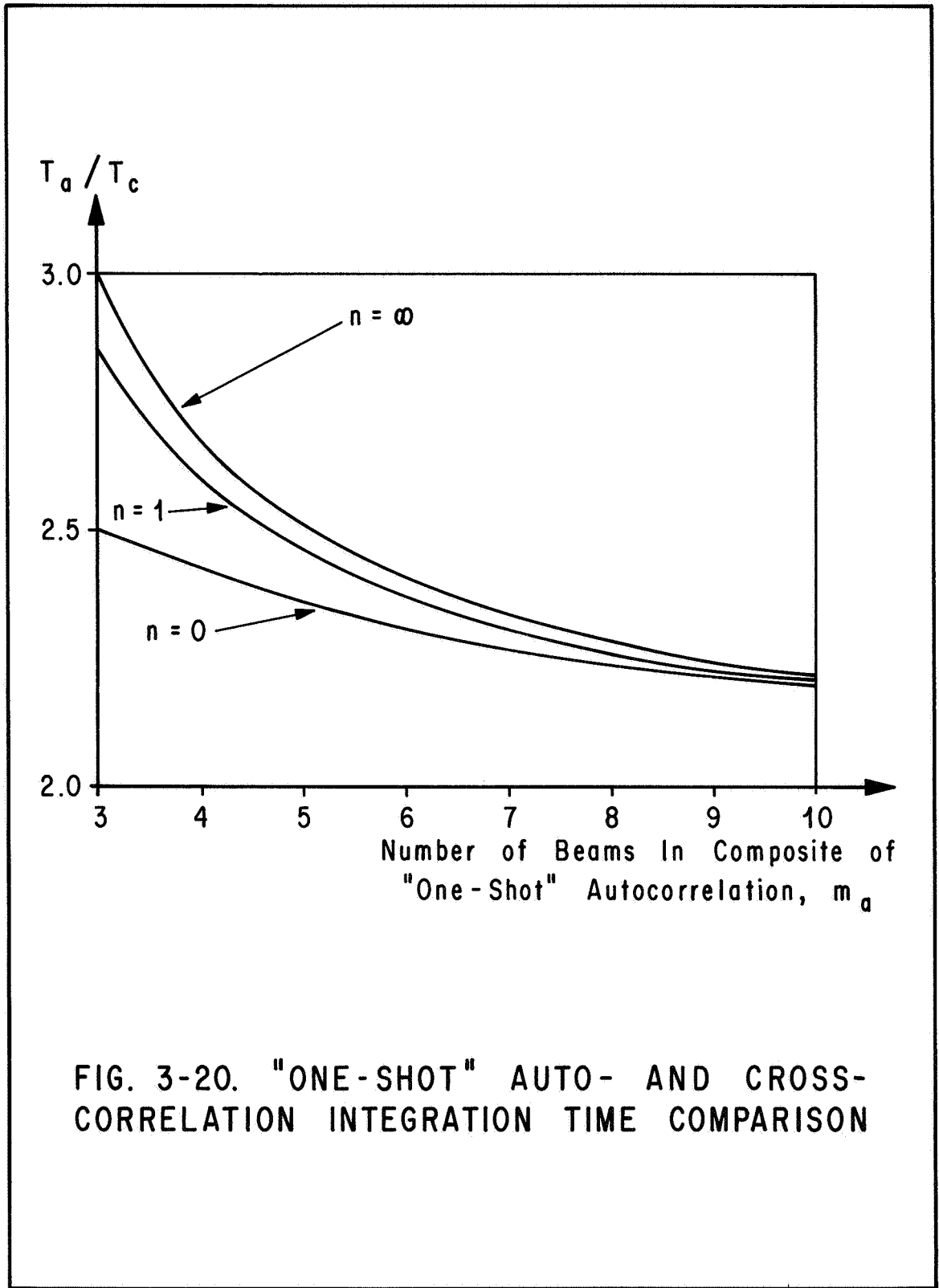


FIG. 3-20. "ONE-SHOT" AUTO- AND CROSS-CORRELATION INTEGRATION TIME COMPARISON

and the upper limit is

$$\lim_{n \rightarrow \infty} (\gamma_c) \rightarrow 1, \quad (133)$$

so that

$$\frac{m+1}{2^m} \leq \gamma_c \leq 1, \quad m \geq 2. \quad (134)$$

Thus, from equation (134), the computation time required to compute the "one-shot" cross-correlation is always less than the time required to compute the m number of cross-correlations separately. However, as n increases, the ratio, γ_c , rapidly approaches its upper limit. For $n \geq 3$,

$$\gamma_c = 1.0, \quad \text{for } n \geq 3 \quad (135)$$

with less than one percent error. Therefore, the "one-shot" computation time is never a disadvantage. Actually, γ_c does not account for computer printout time and other data handling procedures minimized by the "one-shot" method.

Figure 3-21 shows γ_c plotted versus m for $n = 0, 1$ and ∞ .

3.4 Cross Beam Discussion

3.4.1 General Discussion

The "cross-beam" theory [8] is essentially applicable to the measurements discussed below, which were made using crossed beams. However, as described in section 3.1.1, the signals were retrieved from the flow by employing the schlieren principle. The cross-beam runs differ from the parallel beam runs in that the correlated signals from crossed beams are retrieved from a "localized" region defined by the segments of the two beams through which the same disturbances pass. The length of the beam segment is approximately the size of the average disturbance passing through and common to both beams. Because the beams are crossed, the flow disturbances which do not pass through both beams, and thus do not cause correlated fluctuations in the signals, represent noise. As a result, the cross-beam method should require more integration time than the parallel beam method. Nevertheless, the crossed-beam

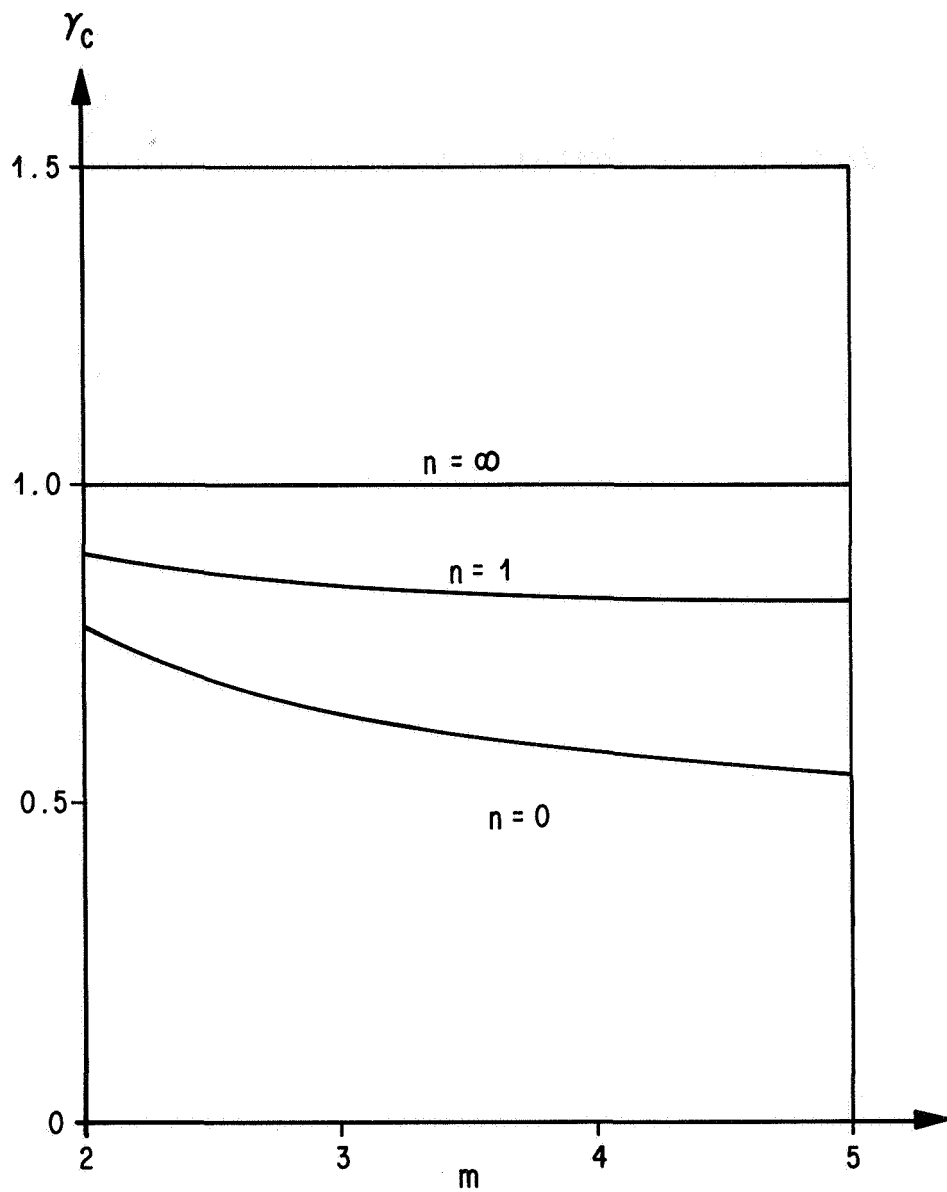


FIG. 3-21. COMPUTATION TIME COMPARISON OF
 "ONE-SHOT" CROSS-CORRELATION WITH
 m NUMBER OF INDIVIDUAL CROSS-CORRELATIONS

geometry offers many more advantages than disadvantages. The development of the cross-beam method is the ultimate objective.

In the following discussion, a crossed-beam geometry was used to investigate the contribution to the correlations computed using parallel beams resulting from (1) the boundary layer on the test section windows, (2) the interaction of the wall boundary layer with the boundary layer on the plate, (3) the wake from the indentations in the plate running parallel to the windows (figure A-8), and (4) a combination of these. Also, a crossed-beam geometry was used to make measurements in the wake of the model.

3.4.2 Effect of the Boundary Layer on the Test Section Windows

In section 3.1.1, it was assumed that the statistical properties of the turbulence along each of the laser beams were constant. This assumption is not valid for positions near the test section windows because of the influence of the wall boundary layer. However, the magnitude of the influence was the important point to be determined.

The necessity for this investigation results from the use of parallel beams. Because the average transit time of the disturbances between two parallel beams decreases from the window to the outer edge of the boundary layer, the effect should produce an unsymmetrical contribution to the correlogram distributed from a time delay (τ) slightly larger than the transit time corresponding to free-stream speed between the beams to larger values of τ . Also, the total contribution from the wall boundary layer should be small compared with the correlation resulting from the disturbances along the beams which are greater than the boundary layer thickness, δ_w , away from the windows (see figure 3-22).

Two runs were made using parallel beams separated by 1.87 inches. The first run was made with the beams passing through the boundary layer on the thin plate model (figure 2-3). The centerlines of the beams were 0.05 inch above the surface of the plate. The cross-correlation of the two signals is shown in figure 3-23B. The time delay of maximum correlation, τ_m , is equal to 0.112 milliseconds (0.106 ms plus 0.006 ms due to parallax). The same result was obtained when the run was repeated.

The beams were elevated to approximately 1.07 inches above the plate. One run was made and repeated twice. From the shadowgraph of the flow (figure 2-3), it can be seen that this is well above the major portion of the boundary layer ($\delta \approx 0.3''$).

All settings on the instrumentation were the same for all three runs made. The correlogram of one of the runs is shown in figure 3-23A. The correlograms of the other two runs were essentially the same as the first.

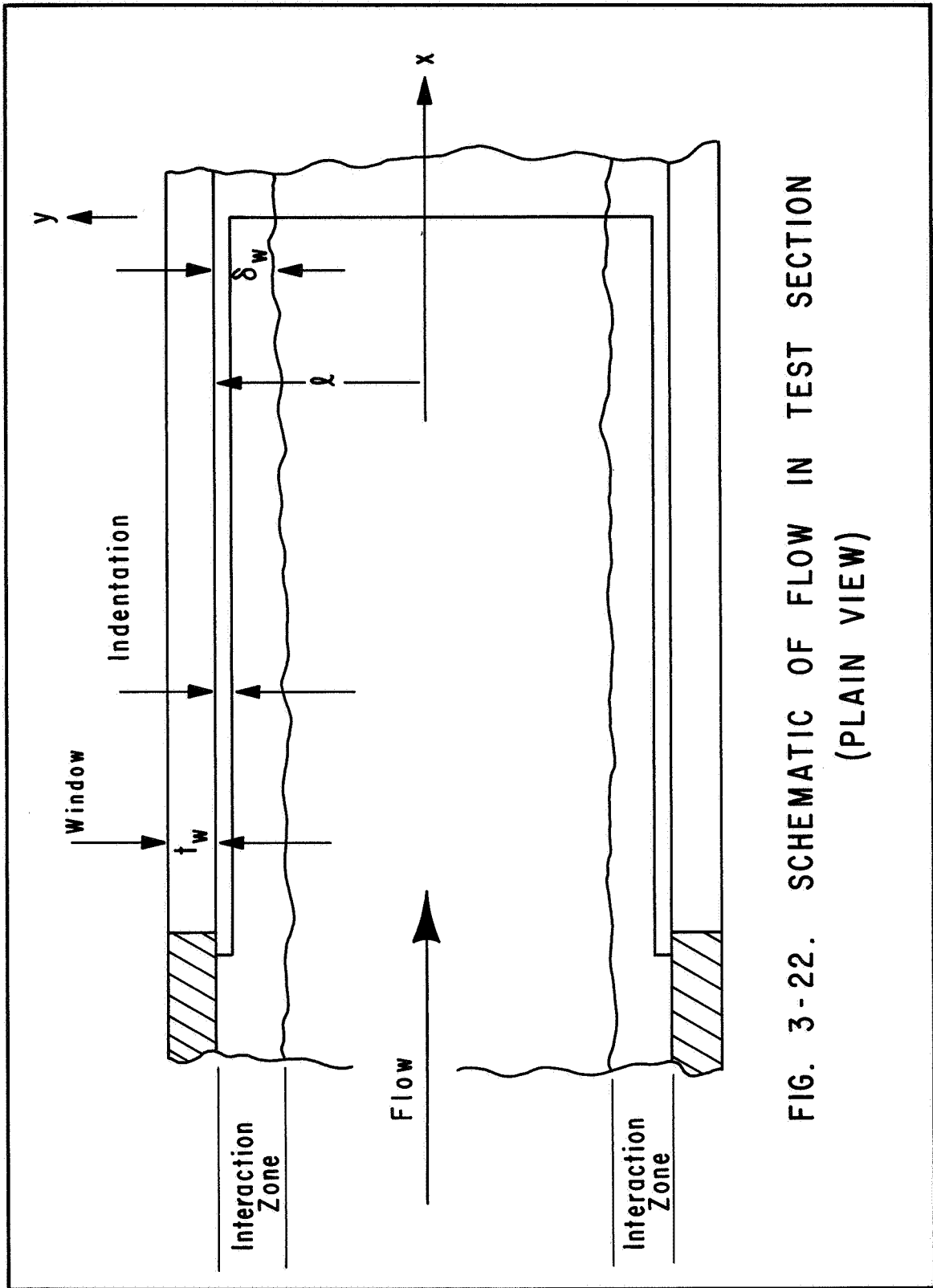


FIG. 3-22. SCHEMATIC OF FLOW IN TEST SECTION
(PLAIN VIEW)

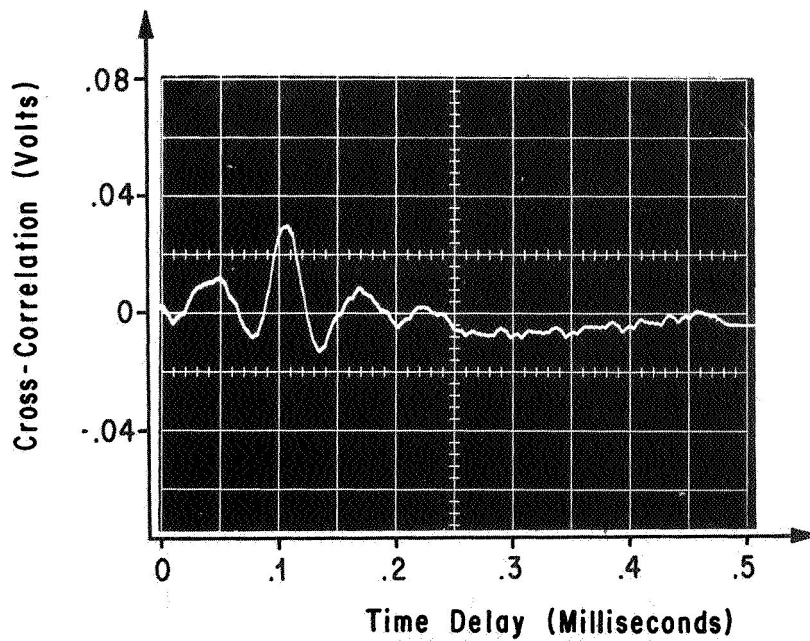
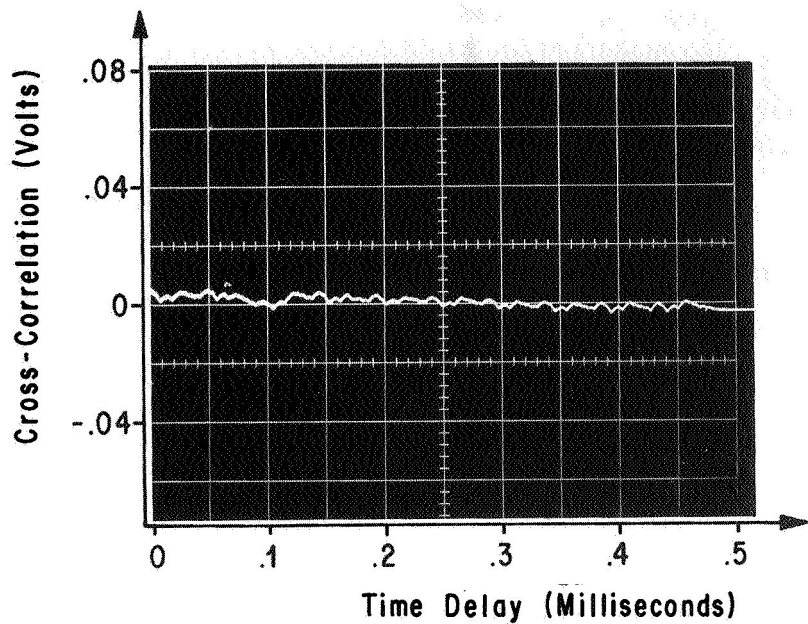


FIG. 3-23. A(TOP): CROSS-CORRELATION OF SEPARATED PARALLEL BEAMS, 1.03 INCHES ABOVE PLATE. B(BOTTOM): CROSS-CORRELATION OF SEPARATED PARALLEL BEAMS, 0.05 INCHES ABOVE PLATE.

A comparison of figures 3-23A and 3-23B would lead to the conclusion that the boundary layer on the test section windows through which the parallel beams pass does not significantly affect the correlogram. The observation that the amplitude of the signals decreased by approximately a factor of five when the beams were in the elevated position well above the boundary layer supports this conclusion.

Although the conclusion is reasonable, we cannot assume that the wall boundary layer 1.07 inches above the plate has the same effect on the correlogram as the flow resulting from the interaction of the wall and plate boundary layers near the surface of the plate. This region of interaction may contribute heavily to the correlation. Therefore, it was necessary to design a test which would separate the correlations along the beams, such that the contributions due to the interaction zone could be separated from those due to the boundary layer on the model.

3.4.3 Investigation of the Boundary Layer Interaction Zone

Figure 3-24 shows the plan view of the test section. The two laser beams were crossed such that the point of intersection was in the middle of the test section and the plane formed by the beams was approximately parallel to the surface of the plate.

Two runs were made with this geometry and the cross-correlograms were computed on-line. Because of the geometry of the beams and the flow, the cross-correlogram is symmetrical about the origin ($\tau = 0$). The positive time lag range was computed during the first run (figure 3-24A), and the negative range was computed during the second run (figure 3-24B). Cross-correlations between the beam segments \overline{AC} and \overline{BC} correspond to the positive range of the cross-correlogram, and cross-correlations between beam segments \overline{DC} and \overline{EC} correspond to the negative range.

Two dominant peaks occurred on the cross-correlogram, one at +0.167 ms and the other at -0.167 ms ($\pm 0.158 \text{ ms} \pm 0.009 \text{ ms}$ due to parallax). The common disturbances producing the correlations represented by these large peaks can be estimated by multiplying the approximate speed of transit, measured with parallel beams at the same distance above the plate (1510 fps) by the transit time (time delay) taken from the cross-correlogram.

$$\begin{aligned} \xi_{\text{approx.}} &= \bar{U} \cdot \tau_m \\ &= (1510)(12)(0.167) 10^{-3} \\ &= 3.02 \text{ inches.} \end{aligned}$$

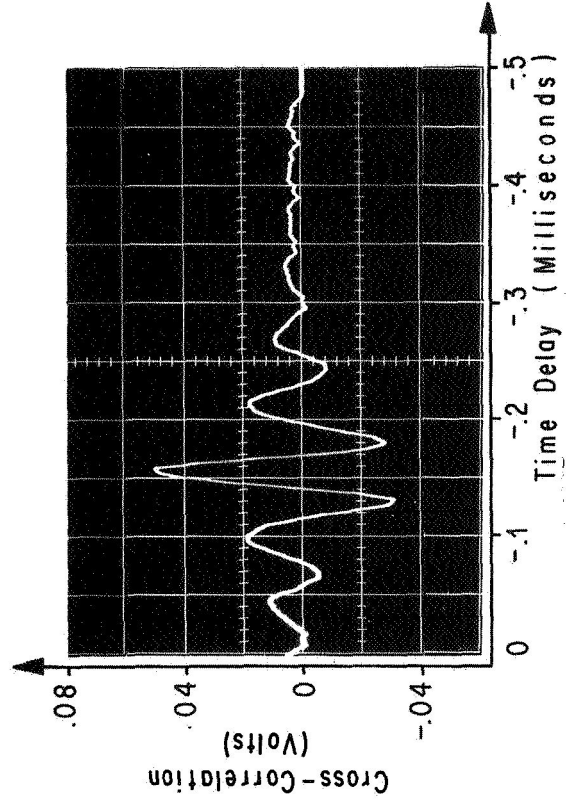
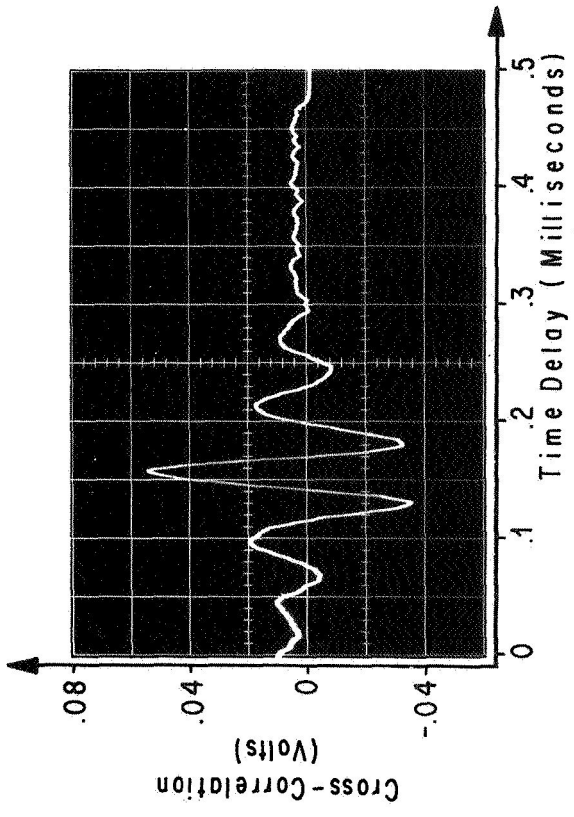
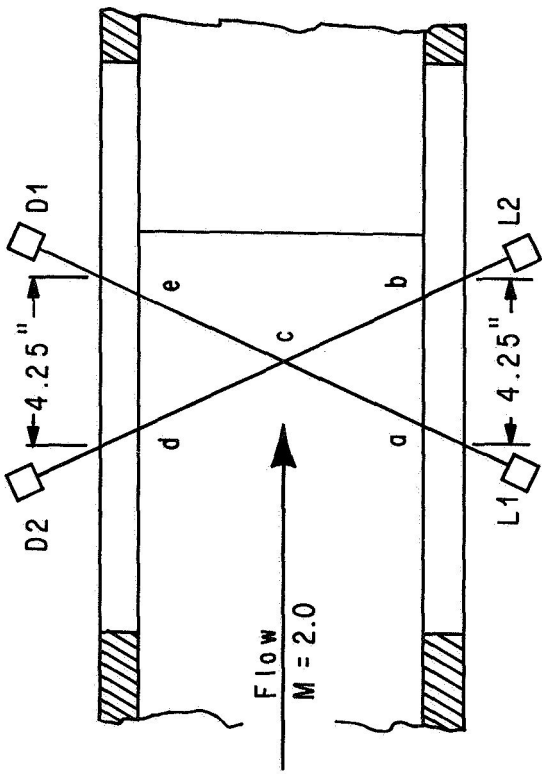


FIG. 3-24. CROSS-CORRELATION MEASUREMENTS OF THE INFLUENCE OF THE INTERACTION ZONE UPON PARALLEL BEAM CORRELATIONS
 A. (LEFT): POSITIVE TIME LAG RANGE
 B. (RIGHT): NEGATIVE TIME LAG RANGE

Thus, the beam segments through which the common disturbances causing these large peaks pass are separated by approximately 3.0 inches. From the beam geometry, we see that the beam segments are very near the windows in the interaction zone of the wall and plate boundary layers.

To check this result, the position of beam intersection was changed (see figure 3-25A). For this run, the beams were crossed in the wall boundary layer on the detector side of the tunnel. The plane formed by the beams was essentially the same as that of the previous case (0.20 inches above the surface of the plate).

The cross-correlogram of beam 1 with beam 2 representing the cross-correlation between beam segments \overline{AC} and \overline{CB} is shown in figure 3-25B. The time lag of maximum correlation is 0.263 ms (0.248 ms + 0.015 ms for parallax). Again using the mean speed of disturbances which was measured with parallel beams, the corresponding distance of separation can be estimated.

$$\begin{aligned}\xi_{\text{est.}} &= \bar{U} \cdot \tau_m = (1510)(0.263) 10^{-3} \quad (12) \\ &= 4.77 \text{ inches.}\end{aligned}$$

Thus, the beam segments through which the common disturbances producing the correlation peak pass are separated by approximately 4.8 inches. From the geometry of figure 3-25A, we see that the beam segments separated by 4.8 inches, as measured in the direction of flow, are well inside the interaction zone near the window.

The positive correlation at zero time lag in figure 3-25B was expected and is due to correlation of the disturbances passing through the intersection of the beams.

Figure 3-26 shows the negative time lag range of the cross-correlogram representing cross-correlation of disturbances passing through beam segments \overline{DB} and \overline{EB} . The zero time lag peak was expected; however, the large peak previously obtained in the negative time lag range with the beam intersection in the center of the test section was not computed. An acceptable explanation for this is not presently available.

For the next two runs, the horizontal plane of the beams was elevated 1.55 inch above the surface of the plate. No other changes were made for these two runs, which were made to evaluate the contribution of the wall boundary layer to the correlogram.

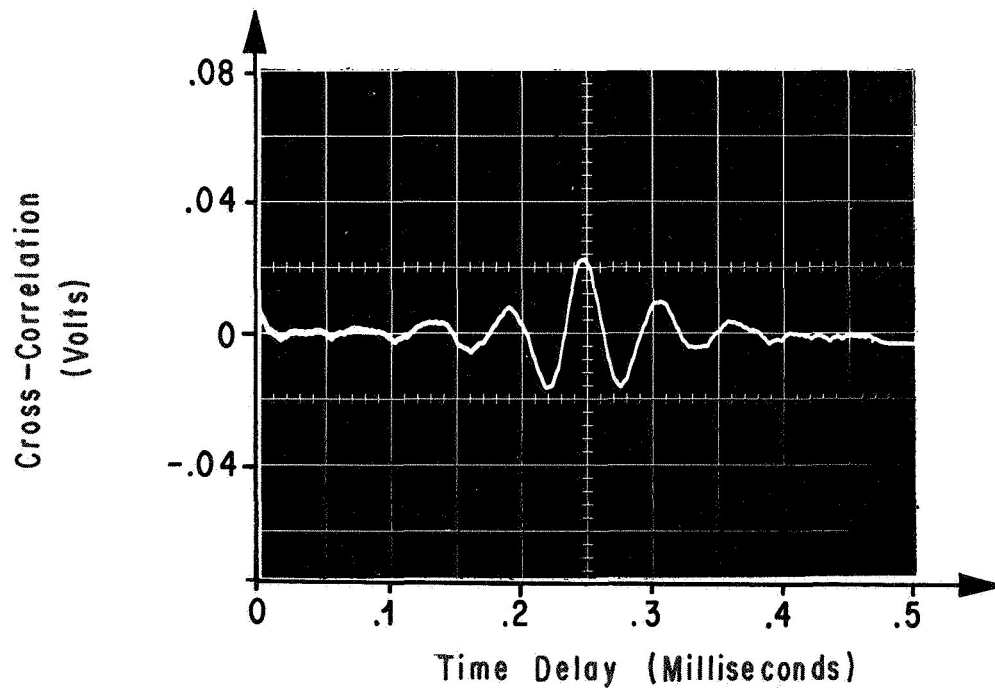
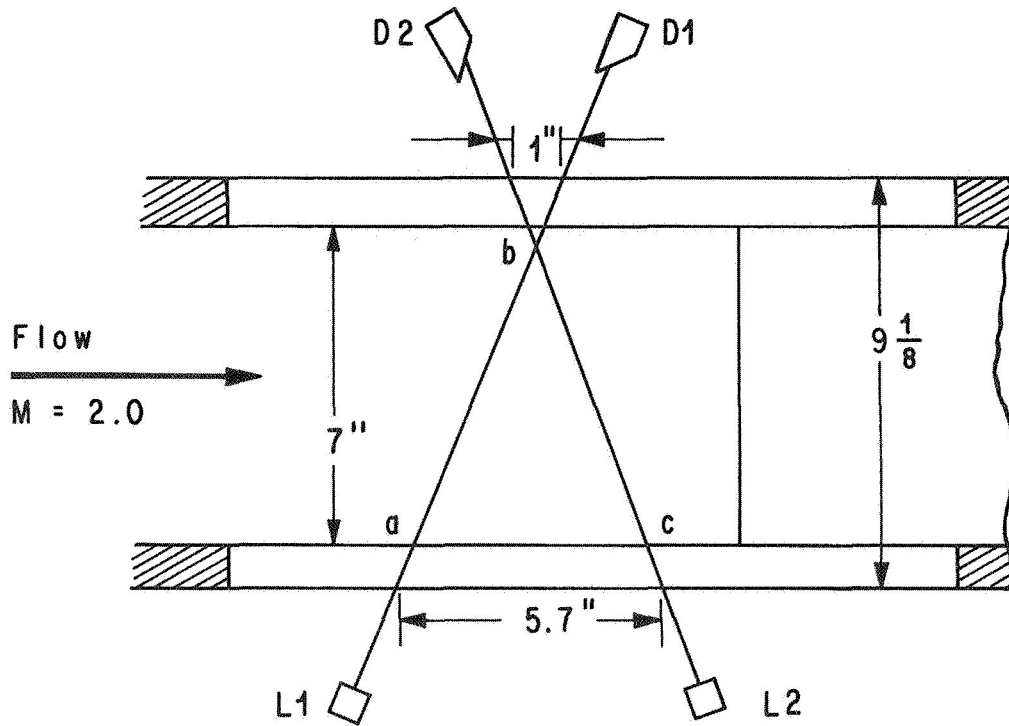


FIG. 3-25. A(TOP):SCHEMATIC OF BEAM GEOMETRY
 B(BOTTOM): POSITIVE TIME LAG RANGE
 OF CROSS-CORRELOGRAM
 SHOWING CONTRIBUTION OF
 INTERACTION ZONE

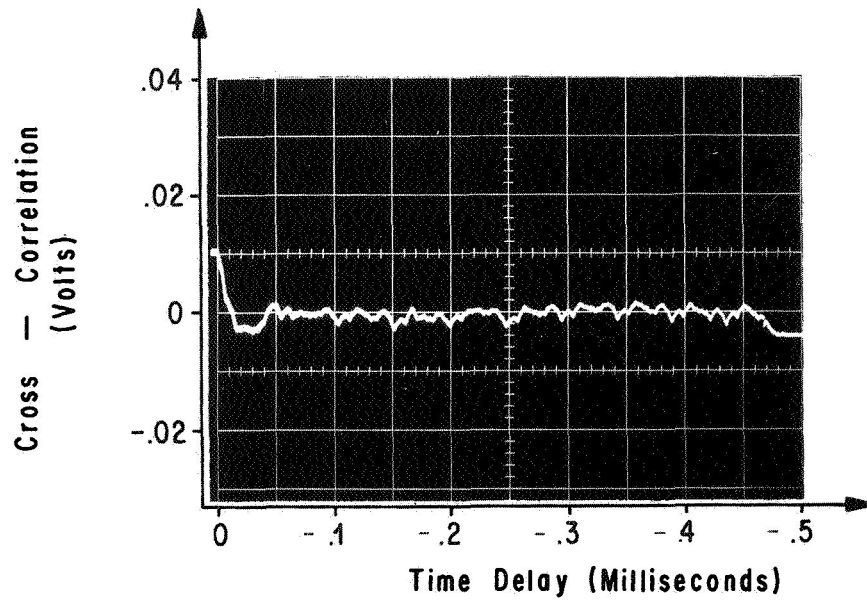
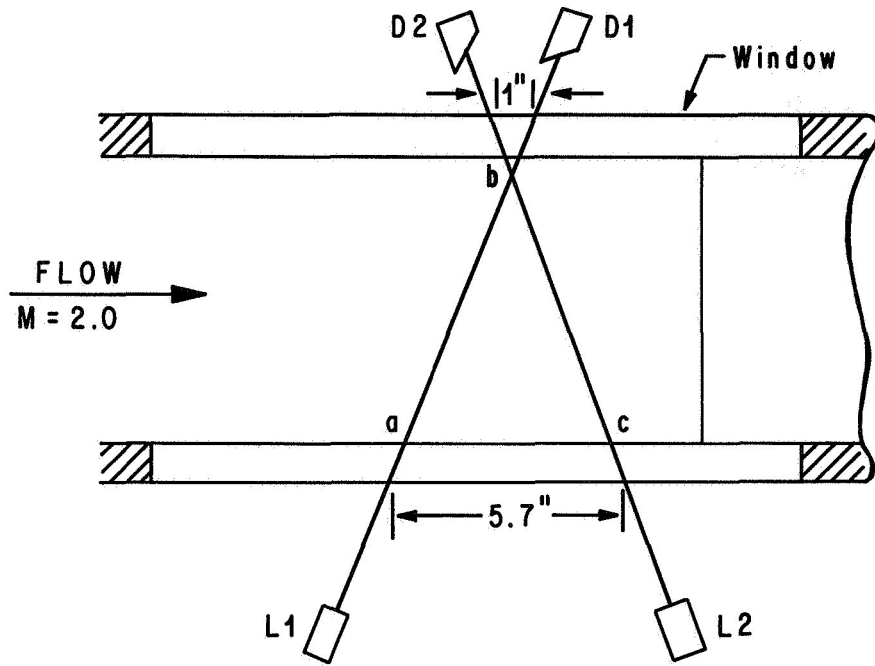


FIG. 3-26. A (TOP): SCHEMATIC OF BEAM GEOMETRY
 B (BOTTOM): NEGATIVE TIME LAG
 RANGE OF CROSS - CORRELOGRAM FOR BEAM
 GEOMETRY SHOWN IN SCHEMATIC

Figure 3-27A shows the positive time lag range, and figure 3-27B shows the negative range. These cross-correlograms corroborate the results obtained using parallel beams, i.e., that the wall boundary layer alone would have very little influence upon the correlograms computed from signals retrieved from the plate boundary layer if the two flows did not interact.

Finally, it can be concluded, but not without an element of uncertainty, that the interaction zone near the window and plate model is a region of intense turbulence and contributes significantly to the magnitude and shape of the correlograms computed from signals retrieved with parallel laser beams presented in this report.

In general, these results do not invalidate measurements taken during this test series, since the test objectives were primarily to ascertain the feasibility of applying electro-optical remote sensing techniques to making measurements of supersonic turbulent flows, and to demonstrate the "one-shot" techniques without extensive alterations to the tunnel or expenditures of time and manpower. From this standpoint, the primary test objectives were achieved, since parallel beam correlation represents an optically integrated ensemble average correlation of "eddy" transit times across the entire test section. However, before quantitative measurements are made using parallel beams, a two-dimensional flow field with minimized edge effects should be sought, possibly through improvement in model design and sensing mode.

Other attempts to minimize edge effects were also examined. One method investigated is a type of shadow-correlation technique, which is described in section 3.4.5. Crossing the beams in a vertical plane which is perpendicular to the flow also effectively eliminates edge effects, but the cross-beam method is rather cumbersome for measuring the velocity profile or other flow properties near flat plates because of geometrical limitations. Transparent models would, perhaps, allow cross-beam measurements, but passing a beam through a transparent model introduces a new problem of beam stability which should be investigated. Nevertheless, cross-beam measurements should be quite successful and convenient for making measurements in the wake. The next section discusses one such attempt to obtain these cross-beam measurements in the turbulent wake of the thin-plate model under investigation.

3.4.4 Cross-Beam Measurement in Turbulent Wake

This section discusses the feasibility of making cross-beam measurements in the turbulent wake of the thin-plate model. More space is available in the wake for geometric beam arrangements than in the boundary layer on the model. However, the beams could not be crossed perpendicular to one another [8] in a vertical plane perpendicular to

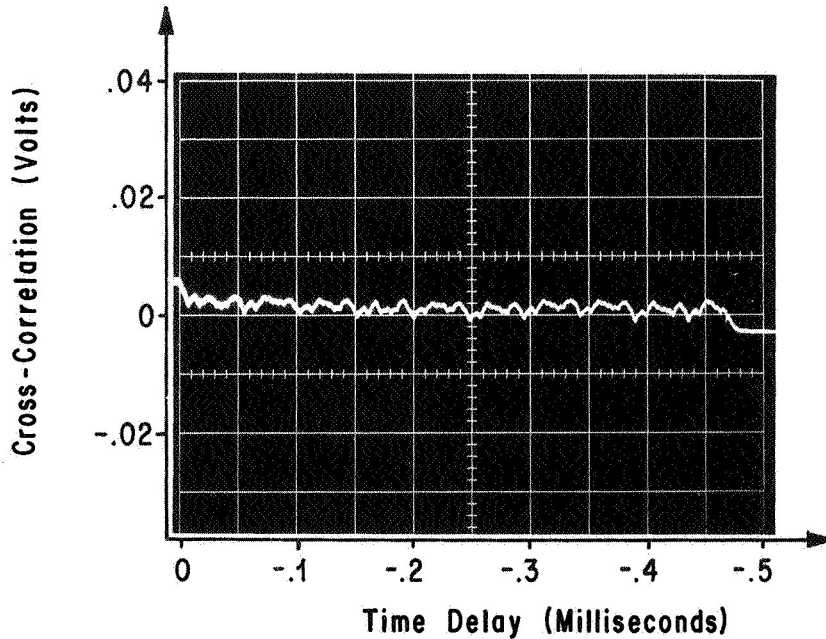
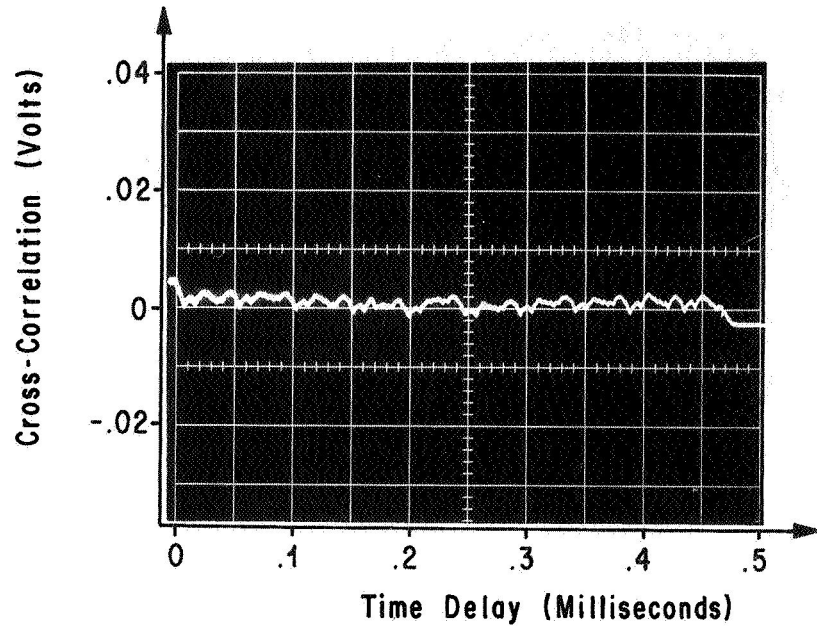


FIG. 3-27. A (TOP): POSITIVE TIME LAG RANGE OF CROSS-CORRELOGRAM FOR BEAM GEOMETRY SHOWN AT TOP OF FIG. 3-26.
 B (BOTTOM): NEGATIVE TIME LAG RANGE FOR SAME BEAM GEOMETRY AS IN (A).

the flow because the Bisonsic Wind Tunnel does not have windows available for passing a vertical beam through the flow. Consequently, a modified cross-beam geometry was used (figure 3-28A). This beam arrangement was sufficient to avoid contributions to the cross-correlogram from the flow field near both windows. Only disturbances in the center of the wake and near the middle of the test section were common to both signals. The distance between the beams traversed by the common disturbances was 0.516 inch.

The cross-correlogram computed for this run is shown in figure 3-28B. The maximum correlation corresponds to a time lag, τ_m , of 0.036 ms (0.034 ms plus 0.002 ms compensation for parallax). Thus, the most probable transit speed of a disturbance, averaged over the transit distance, is

$$\langle U \rangle = \frac{\xi}{\tau_m} = \frac{0.043}{36 \times 10^{-6}} = 1194 \text{ fps.}$$

This speed is 71.9 percent of the free-stream speed, U_∞ , i.e.,

$$\frac{\langle U \rangle}{U_\infty} = \frac{1194}{1660} = 0.719,$$

which is not unreasonable.

The beams were not crossed in the vertical plane because it was desired that the distance between the beams vary across the test section. This provided means by which correlations near the windows, if they would have been present, could have easily been identified by their location on the cross-correlogram.

This cross-beam measurement was apparently successful from a feasibility viewpoint. From these results, it appears that the application of the cross-beam method in measuring certain properties of supersonic turbulent flow is feasible.

3.4.5 Experimental Results Using a Shadow-Correlation Method

In the previous section, it was shown that the interaction zone near the test section windows had a significant influence upon the correlograms computed from signals retrieved with parallel laser beams. The reasons for this are (1) the interaction zone is a zone of more

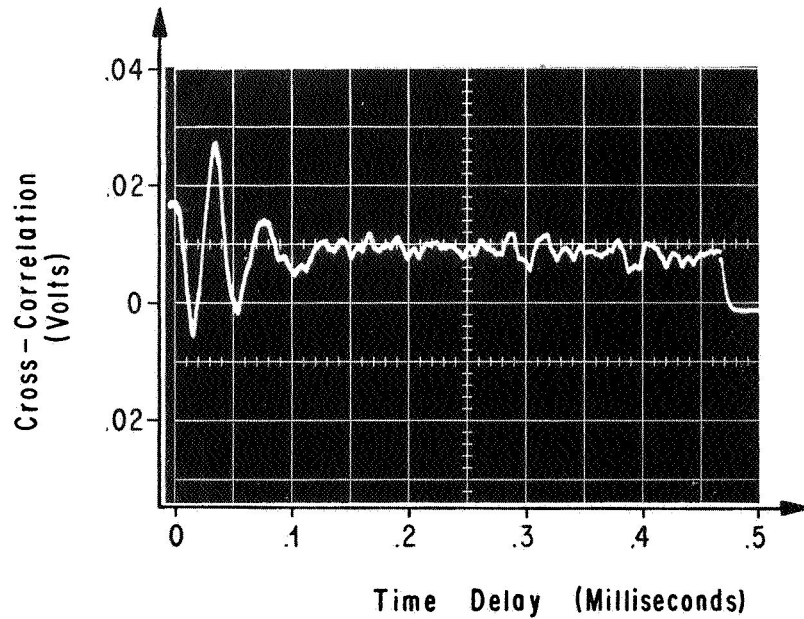
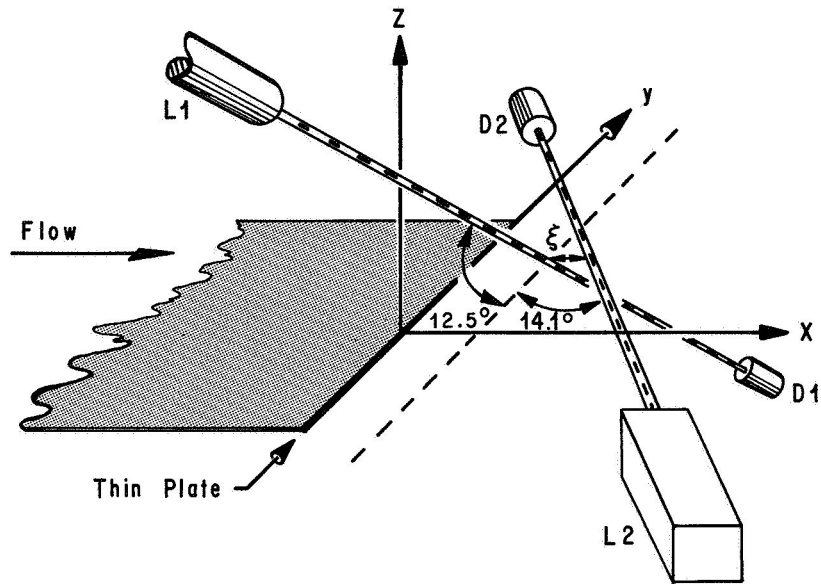


FIG. 3-28. A (TOP): SCHEMATIC OF CROSS-BEAM GEOMETRY
 B (BOTTOM): CROSS-CORRELOGRAM OF LOCAL SIGNAL IN THE SUPERSONIC TURBULENT WAKE OF THE THIN PLATE MODEL

intense turbulence than is the turbulence in the plate boundary layer, and (2) the measurements were made with the laser quasi-schlieren system, which is sensitive to the first derivative of the density gradient component normal to the Poynting vector of the beams.

There are at least four alternatives offering some relief to this problem: (a) to redesign the experiment such that the interaction zone is eliminated or the intensity of the turbulence in it is reduced to an acceptable level; (b) to employ a sensing mode which is less sensitive to the interaction zone; (c) to use crossed beams instead of parallel beams, or (d) to study the turbulence in the interaction zone itself, since it can already be measured very well. Because alternative (a) above is a matter of model or facility design, no discussion will be presented here. Alternative (c) has already been proven to be a successful solution (section 3.4.4). Alternative (d) provides interesting material for discussion but falls outside the scope of this report. Alternative (c) is of direct importance to the purpose here, but will be discussed briefly because of the limitations of the instrumentation available for investigation of the shadow-correlation remote sensing mode.

In section 3.1.1, the laser quasi-schlieren principle was described. It was shown that the ac-coupled electrical time history of a beam was directly proportional to its deflection. This was accomplished by placing a knife-edge in the beam (figure 3-1). As each disturbance intersects the beam, it causes the beam to be deflected in a particular direction, and the knife-edge is sensitive to the x-component of this deflection. Thus, it is evident that the detailed composition of a disturbance determines the magnitude and direction of a deflection. If this is actually the case, then it should be possible to sense the changes in composition by monitoring the intensity fluctuations inside the beam itself. To do this, the knife-edge in figure 3-1 was replaced with a thin plate having a small pinhole. The diameter of the pinhole was smaller than that of the laser beam. The plate is placed perpendicular to the beam such that the centerlines of the beam and pinhole are collinear (see figure 3-29). Because the pinhole diameter is sufficiently small, the photodetector is never exposed to the circumference of the laser beam. Therefore, the fluctuations in total power monitored by the photodetector are a result of the fluctuations in intensity near the circumference of the pinhole produced by the disturbances inside the beam.

Two runs were made using the shadow-correlation mode. The beam geometry for the first of these is shown in figure 3-30A. This run was made with the beams crossed in the horizontal plane in the turbulent boundary layer on the plate model similar to those described in section 3.4.3. The purpose of this run was to compute the contribution to the cross-correlogram resulting from signals retrieved from the interaction

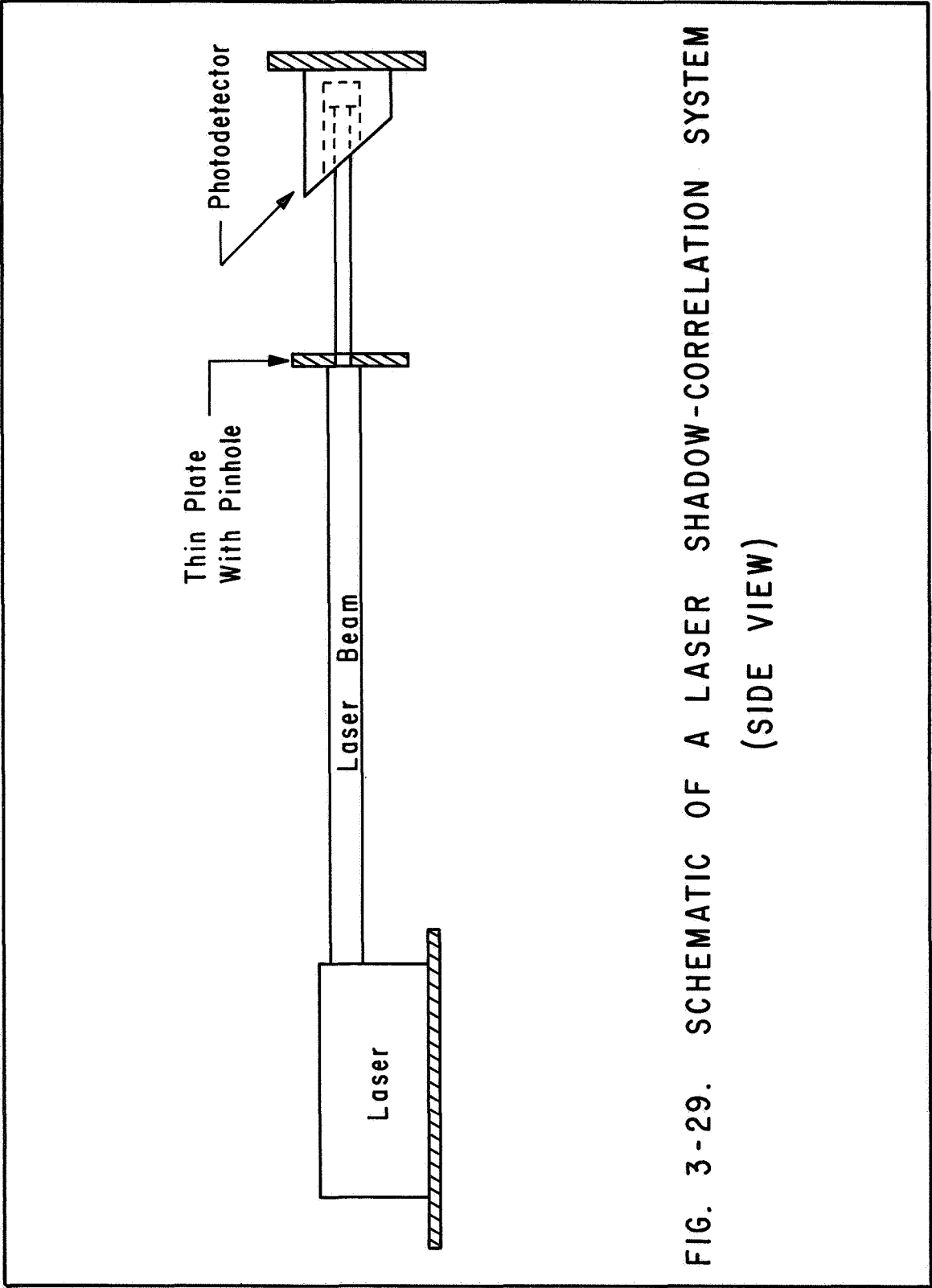


FIG. 3-29. SCHEMATIC OF A LASER SHADOW-CORRELATION SYSTEM
(SIDE VIEW)

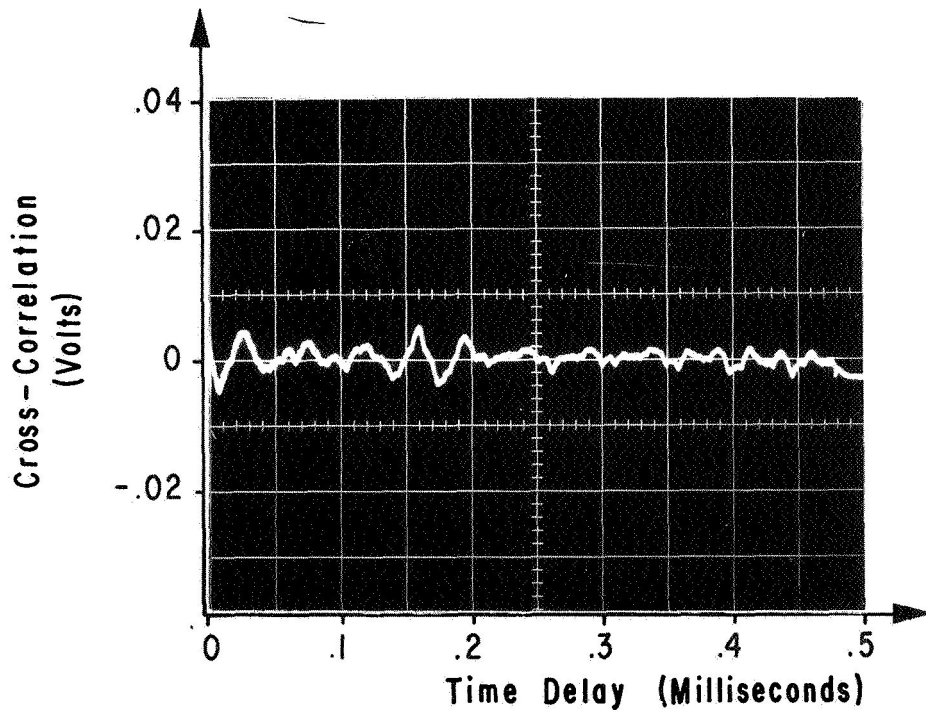
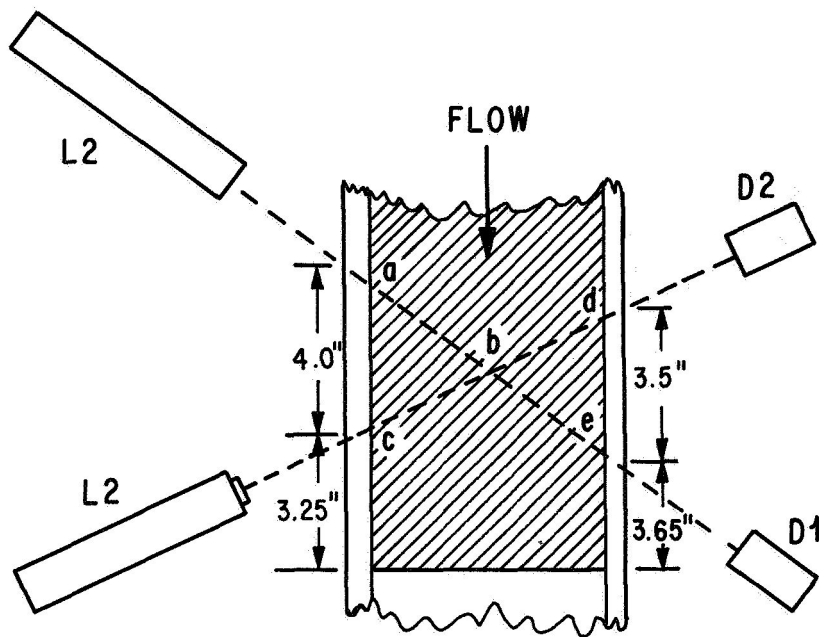


FIG. 3-30A (TOP): SCHEMATIC OF BEAM GEOMETRY.
 B (BOTTOM): SHADOW-CORRELOGRAM OF
 POSITIVE TIME LAG RANGE
 FOR BEAM GEOMETRY SHOWN
 IN SCHEMATIC (TOP).

zones near the windows. The cross-correlogram is shown in figure 3-30B. At a time lag of 0.160 ms, the contribution of one interaction zone can be detected. However, by comparing this correlogram with that of figure 3-24A, it can be seen that a significant reduction has been achieved.

The purpose of the second run was to compute the correlogram from signals retrieved with parallel beams in the turbulent boundary layer for a qualitative comparison with figure 3-30B. The correlogram for this run is shown in figure 3-31B and the beam geometry is shown in figure 3-31A.

Comparing figures 3-30B and 3-31B, it can be concluded that the shadow-correlation mode offers a considerable advantage over the quasi-schlieren mode where the beams must pass through regions of turbulence near or on the test section windows. However, the magnitude of the correlation is reduced for the shadow-correlogram due primarily to a decrease in signal-to-noise ratio.

These conclusions must be considered as preliminary due to the limitations of the instrumentation and hardware available.

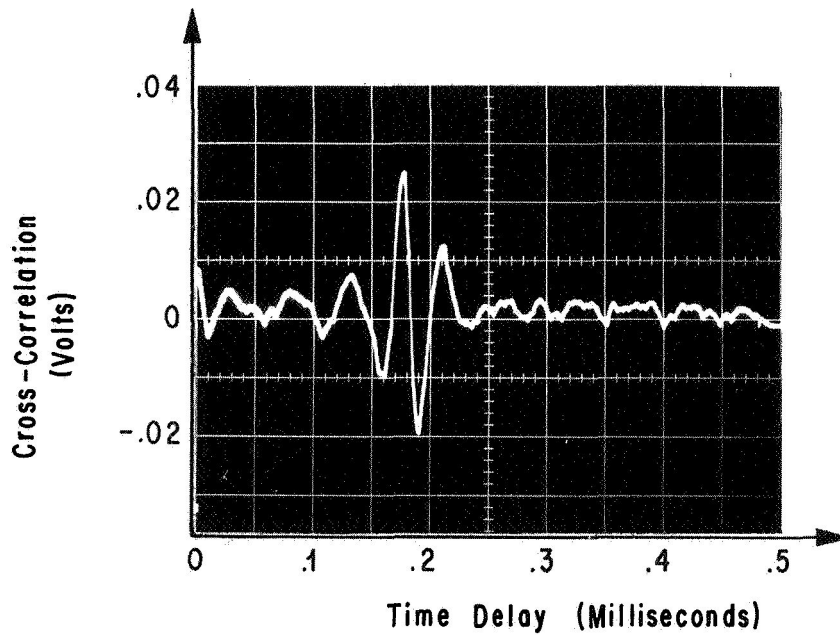
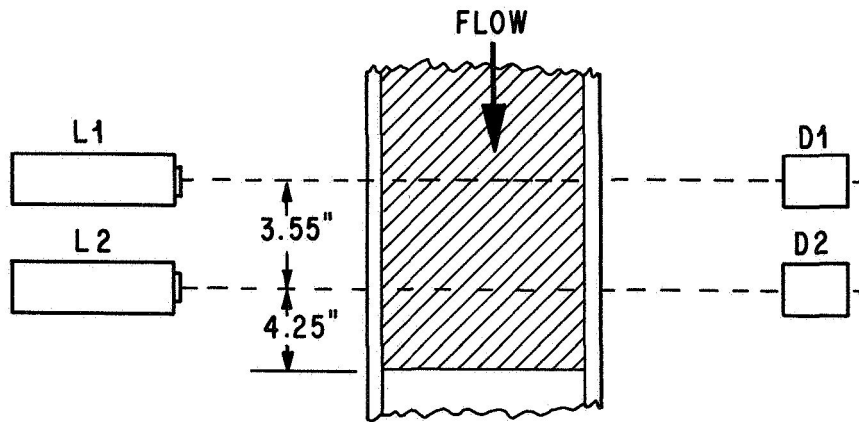


FIG. 3-31. A(TOP): SCHEMATIC OF PARALLEL BEAM GEOMETRY (PLAN VIEW)
 B(BOTTOM): SHADOW CROSS-CORRELOGRAM FOR PARALLEL BEAM GEOMETRY SHOWN IN SCHEMATIC (TOP)

IV. CONCLUSIONS

Theoretical discussions and qualitative experimental results have been presented in an attempt to assess the feasibility of remotely retrieving statistically correlated signals from supersonic aerodynamic turbulence which could successfully be used to compute auto- and cross-correlograms exhibiting accurate, reproducible, and readily identifiable flow-related "peaks" of correlation. With respect to this objective, the qualitative results presented in this report indicate that optical remote probing of supersonic aerodynamic turbulence using statistical correlation is feasible, without the use of tracers, in the Bisons Wind Tunnel of MSFC, and, perhaps, in other facilities which exhibit similar low facility-induced noise levels. Other conclusions of this investigation are as follows:

(1) Optical remote sensing with parallel or crossed laser beams can yield consistent and reproducible statistical results which are related to aerodynamic turbulence, the particular relationships requiring theoretical analyses and quantitative experimental verification.

(2) The use of parallel laser beams for retrieving signals from two-dimensional turbulence* increases the power signal-to-noise ratio relative to that obtained with crossed beams. However, direct localized measurements require the crossed-beam geometry.

(3) The laser quasi-schlieren system presented herein requires isolation from the mechanical, and perhaps acoustical, facility-induced noise. For this system, the major portion of the facility-induced noise enters the system at the light sources.

(4) With respect to the data presented in this report, which was obtained with a laser quasi-schlieren system in combination with a parallel beam geometry, the boundary layer on the windows of the test section did not significantly contribute to the computed correlograms. However, the interaction zone resulting from the interaction of the window and model boundary layers apparently dominated the measurements. This result does not invalidate measurements taken during this test, since the test objective was primarily to ascertain the feasibility of applying electro-optical remote-sensing techniques to making qualitative measurements in a supersonic turbulent flow. From this standpoint, the primary test objectives were achieved. However, before quantitative

*Note: Two-dimensional time-averaged turbulent properties.

measurements are made using parallel beams, a two-dimensional flow field with minimized edge effects should be sought, possibly through improvement in model design and sensing mode.

(5) The shadow-correlation method significantly reduces the contributions of the interaction zones, and the crossed-beam geometry successfully avoids them.

(6) The "one-shot" auto- and cross-correlation methods provide a convenient means for measuring the decay history of turbulent structures in two- or three-dimensional fluid flows (for detailed comparison of these methods see section 3.3.4).

(7) The most important advantages of the "one-shot" autocorrelation method are as follows:

- (a) It represents the only method for measuring the decay history of turbulence from one sample of data.
- (b) Because it is necessary to monitor only a single composite signal, there is a reduction in instrumentation compared to that required for a two-channel cross-correlation system.
- (c) Phase matching errors are eliminated.
- (d) Facility operation is reduced by 400 percent because only one run of the facility is required to measure the decay history.
- (e) The amount of data handling, storage, etc., is reduced.
- (f) The overall data-processing time is reduced.
- (g) This method is the only means by which the decay history can be observed visually "on-line" by displaying the "one-shot" autocorrelograms on an oscilloscope as the data are collected and computed from the same set of turbulent data.

(8) The major disadvantage of the "one-shot" autocorrelation is that the signal-to-noise ratio, taken with respect to a particular time history contained in the composite, is smaller than the signal-to-noise ratio of the particular time history taken separately.

(9) The "one-shot" cross-correlation method has the following major advantages over the "one-shot" autocorrelation: (a) There is a higher signal-to-noise ratio, and therefore the required integration time for a "one-shot" autocorrelation is 250 to 300 percent longer than that required for a "one-shot" cross-correlation. (This statement is, of course, restricted to the assumptions in section 3.3.4.) The "one-shot" method provides a means for computing the cross-correlation peak at zero time delay directly without the electrically induced time delay necessary with the "one-shot" autocorrelation.

(10) The computation time required for the "one-shot" cross-correlation is equal to or less than that required to compute the equivalent number of individual cross-correlations.

(11) The method of induced time delay extends the potential application of the "one-shot" correlation methods and may be used (a) to avoid peak interference on a "one-shot" correlogram, (b) to identify a correlation peak partially lost in correlated noise, and (c) to zone the "one-shot" auto- or cross-correlogram, thereby providing a means for identifying a particular pair of signals associated with a particular correlation peak on a "one-shot" auto- or cross-correlogram.

(12) The laser quasi-schlieren system described in section 3.1.1 is the most reproducible, convenient, and flow-sensitive system presently available for studying remote sensing of aerodynamic turbulence in wind tunnels.

(13) No experimental attempt was made to determine how the correlations computed from signals retrieved using the laser quasi-schlieren system were physically related to the flow disturbances causing the signals. It can be concluded, however, that the correlations presented in this report are related to the propagation of supersonic turbulence.

(14) The shape of the correlogram in the region of a "peak" correlation computed from laser quasi-schlieren signals is directly related to the position of the knife-edges relative to one another and the flow itself. One explanation of this is presented in section 3.1.1 where it is theoretically concluded that the correlation between signals is proportional to the time-averaged two-point product of the fluctuating density gradient component in the direction of flow. For parallel beams, this two-point product is integrated along the beams from source to detector.

APPENDIX A

DESCRIPTION OF THE BISONIC WIND TUNNEL FACILITY, MODELS, AND INSTRUMENTATION

This appendix presents a general discussion of important design characteristics of MSFC's 7-Inch Bisonic Wind Tunnel facility, the two-dimensional, boundary layer and wedge models, instrumentation for remote sensing supersonic flows, the general test procedure, and the analog data reduction equipment used for this test series.

The salient features of this equipment and instrumentation and their respective roles in data interpretation are discussed below.

A-1 MSFC's 7 x 7-Inch Bisonic Wind Tunnel (BWT)

This test facility is a supersonic blowdown type of wind tunnel (Figure A-1). Dry air at atmospheric pressures (or atmospheric air at approximately 14.4 psia with 1.6 percent variation) is supplied to a 7" x 7" test section and exhausted to essentially vacuum conditions (approximately 20 to 29 in. hg.). Figure A-2 shows a schematic representation of this facility. Major dimensions of the tunnel are given in Figure A-3.

Two air dryers are connected in tandem to charge the tanks (Figure A-2). The first takes in air at 3,000 cu ft/min, while the second takes in this amount and recirculates an additional 12,000 cu ft/min. Two combined tanks equipped with a rubber diaphragm liner store up to 60,000 cu ft; however, one tank is currently not in the circuit.

Two Fuller duplex and two-stage rotary pumps provide an overall vacuum rate of 8920 cu ft/min. This results in a 40-minute pump-down time from atmosphere (approx. 14.4 psi) to 0.15 psi for the six interconnected cylindrical steel vacuum tanks. The combined capacity for this vacuum storage is 42,000 cu/ft.

Mach number control is provided by removable nozzles (Figure A-3) machined from solid brass to a tolerance of ± 0.001 inches. A hydraulically activated mechanism clamps and aligns the nozzle in position. The

test section formed by the nozzle is 7.029 inches wide and about 7 inches high (see Figure A-4). Although several nozzles providing Mach numbers of 1.54, 1.99, 2.44, 3.00, 3.26, 4.00, and 5.00 are available, only a Mach number of 1.99 was used in these tests. The test rhombus, shock angle, mass flow, etc., for this nozzle-model combination are discussed in subsection A-2 of this appendix.

The test section side walls which enclose the windows are hinged at the top and are activated by (see Figure A-1) hydraulic cylinders. These doors, one on either side, extend the full length of the test section. The 6- x 6-inch glass windows, 1 and 1/16 inches thick, are mounted in the doors in such a manner that discontinuities between frame and glass surface inside the test section (Figure A-4) are avoided. These windows provide schlieren and shadowgraph visualization of the flow region, as well as to facilitate access for remote sensing by lasers, ultraviolet, or other light sources.

Pneumatically inflated seals are used along the nozzle contour (Figure A-4) and at the rim of the doors. Tunnel operation is automatically blocked if all seals are not activated.

Two primary valves (Figures A-2 and A-3) separate the test section from the air supply and vacuum tanks, respectively. Both valves, which are hydraulically activated, provide positive sealing when closed. When in the open position, a box-shaped extension on the gate is aligned with the tunnel duct in such a manner that a smooth continuity of aerodynamic surfaces is provided.

Starting and stopping processes require about four seconds. The air flow is controlled by the upstream gate valve. This has two advantages: (1) starting loads on the model and test section are reduced to a minimum, and (2) the tunnel is evacuated before the flow is established, and therefore settling time is reduced for the flow since test section pressures are nearer vacuum than atmospheric.

An adjustable outlet diffuser (Figure A-3) of high aerodynamic efficiency increases tunnel running time. The maximum and minimum positions of the diffuser are preset for each nozzle (corresponding to a given Mach number). At the start condition, the diffuser is open and is automatically closed immediately after the flow is established to provide maximum pressure recovery.

The operation of the wind tunnel is automatic. All valves, gates and diffusers are hydraulic, and may be operated through a series of micro-switches and relay circuits by one button. By turning the selector switch to manual position, any of the operations can also be controlled individually, if desired.

Figure A-5 shows the details of the control console for the tunnel, along with an optional tape recorder. Notice the simplified controls and lighted control diagram mid-way of the center panel. In this visual-control schematic, each control element (valve, diffuser, etc.) is illuminated as it is activated either manually or electronically. The close proximity of the tunnel control console can be observed in Figure A-1.

Additional information on the 7-inch Bisonic Wind Tunnel can be obtained from reference 7.

A-2 Models

This section describes the design characteristics of the models used in this test series. The model most frequently used in this series is a thin two-dimensional plate for generation of turbulent boundary layer and wake flows. The second model consists of a two-dimensional wedge for simulation of base recirculating flows.

A-2.1 Thin Plate Model

This model is essentially a two-dimensional turbulence-generating plate (Figure A-6) constructed of aluminum. The leading edge has a $9^{\circ}32'$ taper which extends back for 1.5 inches. The plate consists of a $1/4$ " thick flat surface for an additional 4.5 inches. The overall plate, 17 inches long, has a trailing edge of 11 inches with a very slow $1^{\circ}34'$ taper. This model was mounted parallel to the floor on the horizontal centerline of the test section (Figure A-7). It spans the full width of the tunnel for the first $5-1/4$ inches, but has a $5/32$ -inch cutout or indentation on either side, avoiding full contact with the window of the tunnel (see Figure A-4). The model showing surface finish, leading edge, and threaded holes (six 8-32) for mounting is photographed in Figure A-8.

During these tests the models were operated with the Mach 1.99 nozzle. The flow field resulting from this combination of nozzle and thin-plate model is depicted in Figure 2-3.

The model was mounted as shown in Figures A-4 and A-5. In this position, the sonic throat moves slightly downstream (positive x-direction) from the nozzle geometric throat, and dual sonic throats (one above and one below) are formed on the model about one to one and one-half inches downstream of the nozzle throat. It can be seen from the shadowgraph in Figure 2-3 that no shock rhombus is formed on by leading edge or reflection from the walls.

Assuming the throat location described above, one-dimensional Mach number, static pressure, density and temperature variations were calculated for the model-nozzle combination. This information is depicted in Figure A-9 which also shows a drawing of the geometric relationship of the model and nozzle contour. The freestream flow speed in the test section is approximately 1660 fps. This information was used for comparison to convection speeds measured by the remote sensing system.

A-2.2 Two-Dimensional Wedge Model

The two-dimensional wedge model for simulation of recirculating base flows is presented in Figure A-10. The model, about 7 inches wide, about 4 inches long, and about 0.75 inch thick, spans the full width of the tunnel. Constructed of aluminum, the model is relatively smooth and has a surface finish (about 125). The leading edge has a 9° taper. The wedge is attached to the tunnel side walls by four 8-32 screws with the axis mounted along the centerline, and the tapered leading edge facing upstream. The flow field generated by this model is shown in Figure 2-1.

A-3 Instrumentation

This section describes the instrumentation used for sensing in this test series.

A typical laser-schlieren wiring schematic for remote-sensing instrumentation is shown in Figure A-11. Several variations of this arrangement are possible, depending on the type of flow problem and data desired (e.g., amount of filtering, amplification, general flow conditions, etc.). The basic components as seen from the schematic are, in order, a source (or laser), photodetector, photodetector power supply, amplifiers, low and high cutoff filter (optional for some cases), oscilloscope for observation of raw data signal, analog correlator, and finally an oscilloscope and Polaroid camera for viewing and recording the final correlogram of the signals.

Figure A-12 is a photograph showing part of the instrumentation installed at the 7-inch Bisonic Tunnel. This photograph shows the general arrangement of the light source (placed for parallel beam measurements), the traversing and elevating stand, the analog correlator, and part of the conventional schlieren system from which flow studies can be made independent of the remote-sensing system. Figure A-13 shows more details of the electronic equipment used for processing the raw signals. This equipment is described in more depth in the following paragraphs.

A-3.1 Photodiodes

The photodiodes used for signal detection were EG&G (Edgerton, Germeshausen, & Grier, Inc.) Model S-D 100. This is a fast response light detector which operates in the visible and near-infrared spectrum. This silicon photodiode, operating over a wide spectral range, has fast response time combined with high sensitivity. Spectral response is from 0.35 to 1.13 microns (near ultraviolet to near infrared). The sensitivity is $0.25 \mu\text{a}/\mu\text{w}$ at 0.9μ . Typical values of rise and fall times are 4×10^{-9} and 15×10^{-9} sec. Noise equivalent power (NEP) is in order of 1×10^{-12} watts/ $\sqrt{\text{cps}}$ at 1000 cps. A dark current lower than 0.2×10^{-6} amperes can be achieved with a bias of 10 volts.

The temperature operating range varies from -65 to $+100^\circ\text{C}$. The window is 0.12" in diameter, constructed of Corning 7052 glass. Sensitive area is 0.11 in^2 (0.073 cm^2). Typical characteristics of this photodiode are summarized in the following table.

TABLE A-1. PHOTODIODE CHARACTERISTICS

	Minimum	Typical	Maximum	Units of Range
Spectral Response	0.35		1.13	Microns (10% points)
Sensitivity (0.9μ)		0.25		$\mu\text{a}/\mu\text{w}$
Rise Time		4×10^{-9}		Sec @ 90
Fall Time		15×10^{-9}		Sec @ 90
Linearity		R^n		$n = 1.0$ (within 5% over 7 decades)
Bias	1		150	Volts
Capacitance		8		Picofarads @ 90
Saturation Photo-Current			0.12	Peak amps from photo active area, load < 500 ohms at 90 bias
Operating Temperature	-65		+ 100	$^\circ\text{C}$

During testing, these photodiodes are mounted in a convenient housing which has a BNC connector. The photodiode housing mounted on Uni-Slide elevating mechanisms are shown in Figure A-14. The adhesive tape showing on the photodiode holds safety razor blades in position to split the beam, thus creating a quasi-schlieren effect (see section 3.1.1). The photodetectors are mounted on an elevating and traversing stand similar to the laser source (Figure A-12). Figure A-15 shows the photodetector and mirror arrangement used for the cross beam measurement discussed in section 3.4.1.

A-3.2 DC Power Supply

The photodiode power supply consists of a 22-1/2 volt battery with an adjustable potentiometer to regulate the dc current. Normal operation is less than 1/2 unit output with a total power up to 1 milliwatt. Figure A-16 shows typical noise voltage as a function of frequency. These components are housed in a small metal box (2" x 4" x 4") with appropriate BNC connectors attached for convenience of operation.

Figure A-16 shows that, for a 22-1/2 V battery, this photodiode has less than 5 percent noise from 500 Hz to large values of frequency. Figure A-13 shows the photodiode power supply "one line," installed in its normal location.

A-3.3 Amplifiers

The amplifiers used for these tests were two (one per beam) Redcor Model 500, a two-stage type. The operating power of these amplifiers is 115V \pm 10 percent, 60 cycle ac current at 10 watts. The gain for each stage ranges from a minimum of 10 to a maximum of 1000 in 10 steps with accuracy of \pm 0.02 percent (dc), linearity \pm 0.01 percent (dc) and stability \pm 0.01 percent (dc). Bandwidth at 3 db full scale is 1000 KC maximum (dc) and 10 cps minimum (dc). Temperature operating range is 0 to 50°C. The following noise for the REDCOR is quoted with 99.9 percent confidence.

TABLE A-2. TYPICAL AMPLIFIER NOISE

<u>Frequency</u>	<u>Noise</u>
100 KC	10 μ v RMS
1 KC	20 μ v peak to peak
300 cps	14 μ v peak to peak
30 cps	4 μ v peak to peak

The output is ± 10 volts, ± 10 milliamperes current for both channels, and the settling time for a full-scale step input is 20 microseconds to 0.01 percent of final value at 100 KC bandwidth. Additional features of this amplifier is an adjustable bandwidth, high input impedance, and a bandwidth that is unaffected by gain change. It also features a solid state chopper.

Figure A-13 shows a pair of Redcor amplifiers on line; the corresponding wiring diagram is shown in Figure A-11.

A-3.4 Filters

An Allison variable filter (Model 2BR) was used on each leg of the remote sensing circuitry (see figures A-11 and A-13). This filter features two separate networks: a high-pass double K section filter (0 to 20 KC) and a low-pass double K section filter (0 to 20 KC). The low pass frequency was not used for this test; rather, the low pass was limited to 30 KHz by the Redcor low-pass frequency cutoff or to 100 KHz when no low-pass filter was used. Each filter has 2 controls: an active band switch which changes the cutoff frequency in octave steps and a multiplier dial which tunes the cutoff frequency over one octave. The cutoff frequency is that which is attenuated approximately 3 db from the minimum insertion loss. The minimum band pass without additional insertion loss is 1/3 octave. The attenuation rate of these filters is about 30 db per octave. Each was pre-tuned to provide a minimum phase shift for signals over the frequency range anticipated in these tests. Distortion is about 1 percent for a 10-volt input, and at 1 volt, it is less than 0.10 percent. This instrument is recommended for measurements to 120 db below 1 volt.

A-3.5 Light Source

The signal source was supplied by two types of lasers: a Spectra-Physics (S.P.) Model 130 Gas laser and a Quantum Physics (Q.P.) Model LS32 laser. These lasers are illustrated in Figure A-17 in the position for parallel beam remote-sensing in the Bionic Tunnel. Figure A-18 shows the quantum physics elevated by a Lab-Jack in order to obtain cross-beam turbulence flow measurements in the wake of the thin plate.

The operational and design characteristics of these lasers are examined in more detail in the following:

- ° Spectra-Physics Laser. The Model 130 S.P. laser has a helium-neon gas filled plasma tube 27.5 cm long with an inside diameter of 2.5 mm. The ends of this tube are terminated with optical, schlieren-free, fused silica Brewster's angle windows which result in a plane polarized output. Wavelength of this output is in the visible red circa 6328Å.

The standard instrument has a hemispherical resonator with one spherical reflector (30 cm radius) and one planar reflector. The resonator output power is 0.75 millivolts CW (minimum) from the spherical end. Resonator reflectors are also of optical quality, schlieren-free, fused silica. Reflectors are multi-layer dielectric coated for at least 99 percent reflectivity (at desired wave length) and are anti-reflection coated on back surfaces.

Beam diameter is 1.4 mm at the exit aperture, and diverges less than 0.7 milliradians (145 seconds of arc). Power input requirements are provided by a self contained discharge exciter dc power supply. This requires a 60 cps 115 volt input of approximately 90 va. The laser mode of operation normally used for these tests is TEM_{00} .

- Quantum Physics Laser. The Quantum-Physics gas-filled helium-neon laser (model LS32) used in these tests has a beam diameter of 1 mm, a power level output of 0.75 mw, and a wave length of 6328Å. In general this laser is similar to the Spectra-Physics Model 130 previously described.

A-3.6 Miscellaneous Laboratory Equipment

Other items of equipment consisted of two conventional Tecktronix Model 502A dual beam oscilloscopes, one for observing and measuring peak-to-peak voltage of the raw signal and one for viewing and recording the processed or correlated signal from the Princeton analog correlator. The latter was fitted with a swing-away Tektronix camera adapter. The signal was recorded on speed 3000 film by a laboratory Polaroid Land Camera. By using a manual shutter control, with an f setting of 16 and time exposure, the signal was traced on exposed film from a remote switch on the Princeton correlator where it had been temporarily stored in a multiple capacitor bank. A DIGITEX digital-type DC voltmeter was used to optimize power output by fine adjustment of the photodetector before each run. This equipment is shown in Figures A-11, A-12, and A-13.

A-4 Test Procedure

Before each series of runs, the equipment was checked to insure that each instrument was adjusted properly. Also, the band pass was selected commensurate with the particular test objectives, and filters were phase-matched by use of a signal generator and oscilloscope. The next step in the procedure was to align the laser source in the desired geometrical position and focus the beam onto the photodiode until the photodetector power output was maximized. This power output was approximately half of that available, since the remaining half of beam intensity was blocked by the knife-edge.

Pre-run checks were made with and without flow to determine the extent of extraneous noise which was correlated in the signals. When ground loops and extraneous mechanical vibrations were minimized, the desired band pass was set, the gains of the amplifier were adjusted to avoid clipping the signal, and the correlator gains were adjusted to optimize the correlatable signal to overcome correlator noise, yet at the same time avoid signal clipping. Blinking red lights warned when the correlator was overdriven.

Direct current signals were recorded before each run, and the dc meter disconnected from the circuit to avoid ground loops. Atmospheric pressure, ambient temperature, and the inches of vacuum were also recorded before each run. The tunnel was activated by the automatic start button allowing about five seconds for the tunnel to settle to steady state operation. The visual display panel indicated the sequence of valves and outlet diffuser positioning. Visual observations of these were made during each run. Run time varied from about 40 to 60 seconds for each case. Data were correlated "on-line" and temporarily stored in the analog correlator. Upon completion of the run, the correlation function was displayed on the oscilloscope and recorded on a polaroid photograph.

A-5 Data Reduction Equipment

Data taken during this test series were reduced on a Princeton Model 100 analog correlator. The primary function of this computer is to solve the following relationships:

$$C_{1,2}(\tau) = \lim_{T \rightarrow \infty} \frac{1}{T} \int_0^T f_1(t) \cdot f_2(t - \tau) dt$$

where "C" is a cross-covariance of the fluctuating portion of random signals which contain flow information. Signals f_1 and f_2 , respectively,

represent information from two beams of electromagnetic radiation. If f_1 and f_2 are identical, then the result is an autocorrelation where the following result is obtained:

$$C(\tau) = \lim_{T \rightarrow \infty} \frac{1}{T} \int_0^T f(t) \cdot f(t - \tau) dt.$$

This instrument operates as a hybrid computer to solve either of the two integrals for 100 n points of incremental time delay, $\Delta\tau$.

The "nth" point is approximated by

$$C_n(t) = \frac{1}{RC} \int_{-\infty}^{-\frac{t-t'}{RC}} V_A(t') \cdot V_B(t' - nt) \Delta dt,$$

where the following are true:

- "RC" = time constant of the averaging circuit
- " $n\Delta\tau$ " = time coordinates of the computed points
- t' represents past history (i.e., $t' > t$).

The three basic operations performed by the computer are (1) time shifting, (2) multiplication, and (3) integration.

The computed values are stored in a 100-channel analog memory and may be recorded during and after computation on stripcharts, x-y recorder or an oscilloscope-camera combination. The latter method was used to record data for this report. Computed accuracy should not exceed 1 percent deviation from the idealized function for any of the 100 points calculated.

Other typical specifications of the Princeton Correlator are as follows:

- Useful frequency range = Dc to about 250 KHz.
- Averaging time constant (normally 20 sec) can be varied from 0.1 to 400 seconds.

- Blinking red lights warn operator when the dynamic range of the input amplifiers is exceeded.
- Computed values can be stored in the correlator with a decay that will not exceed 300 mv in 10 minutes at 25°C.
- The compilation error is less than 1 percent of true value.
- Calibration accuracy = ± 2 percent.
- Gain = 0.01 to 5.0 in 1, 2, 5 sequence (with a variation of less than 0.1 percent/hour).
- Zero drift = ± 10 mv/hour.
- Linearity ≤ 1 percent.
- Delay range = 100 microseconds to 10 seconds in 1, 2, 5 sequence.
- Delay (time base τ) accuracy = ± 1 percent at mid-range and ± 2 percent at five fastest and three slowest ranges.

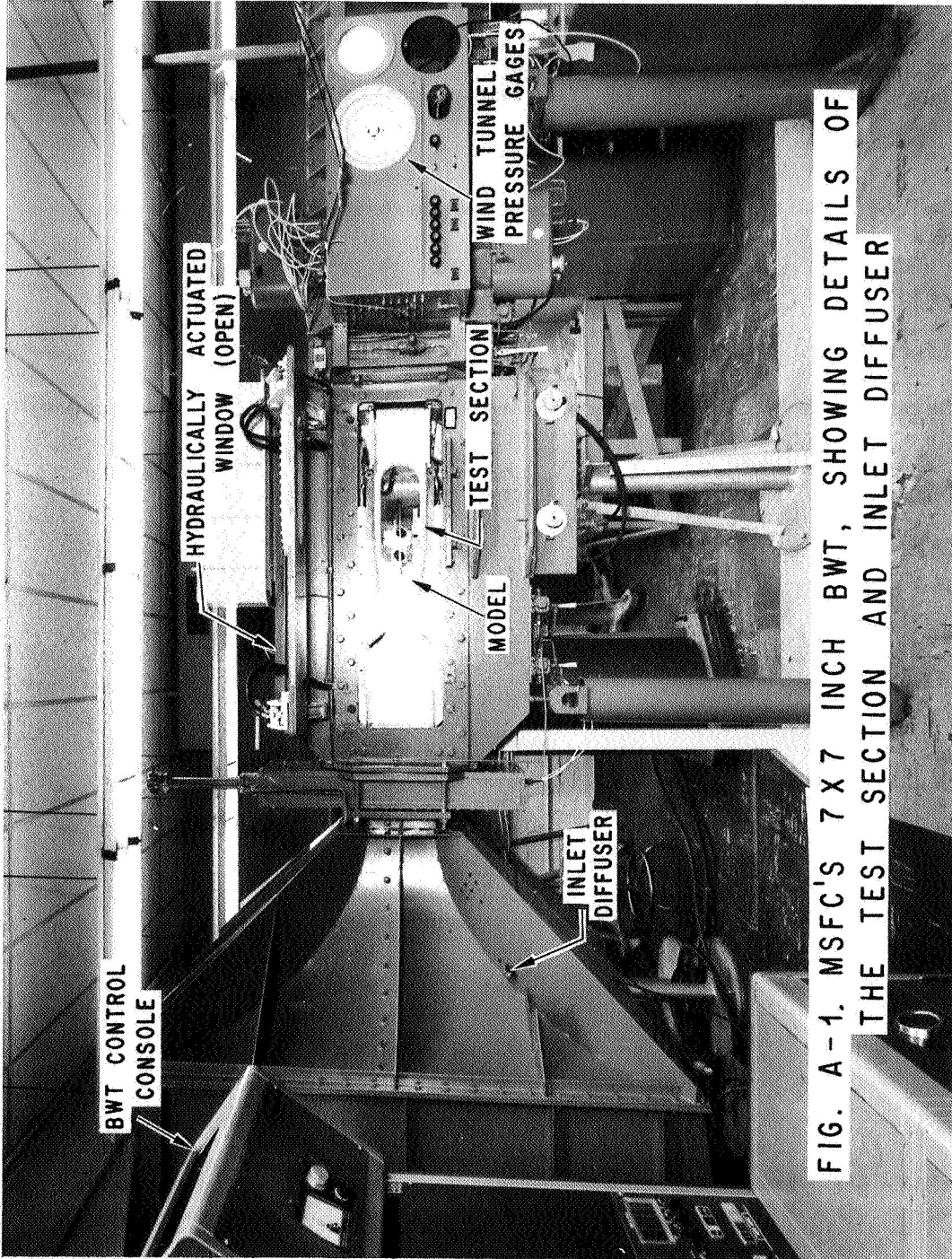
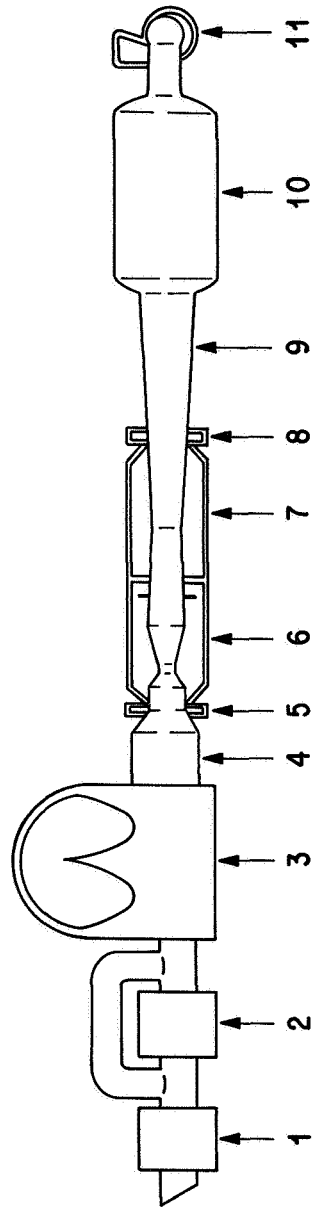


FIG. A-1. MSFC'S 7 X 7 INCH BWT, SHOWING DETAILS OF THE TEST SECTION AND INLET DIFFUSER



- | | | |
|-------------------------|--------------------------|----------------------------|
| 1. Dryer, Type CH | 5. Upstream Gate Valve | 9. Fixed Diffuser and Duct |
| 2. Dryer, Type CHR | 6. Test Section | 10. Vacuum Tank |
| 3. Dry Air Storage Tank | 7. Diffuser Section | 11. Vacuum Pump |
| 4. Settling Chamber | 8. Downstream Gate Valve | |

FIG. A-2. SCHEMATIC DRAWING OF
MSFC'S 7 x 7" BISONIC WIND TUNNEL FACILITY

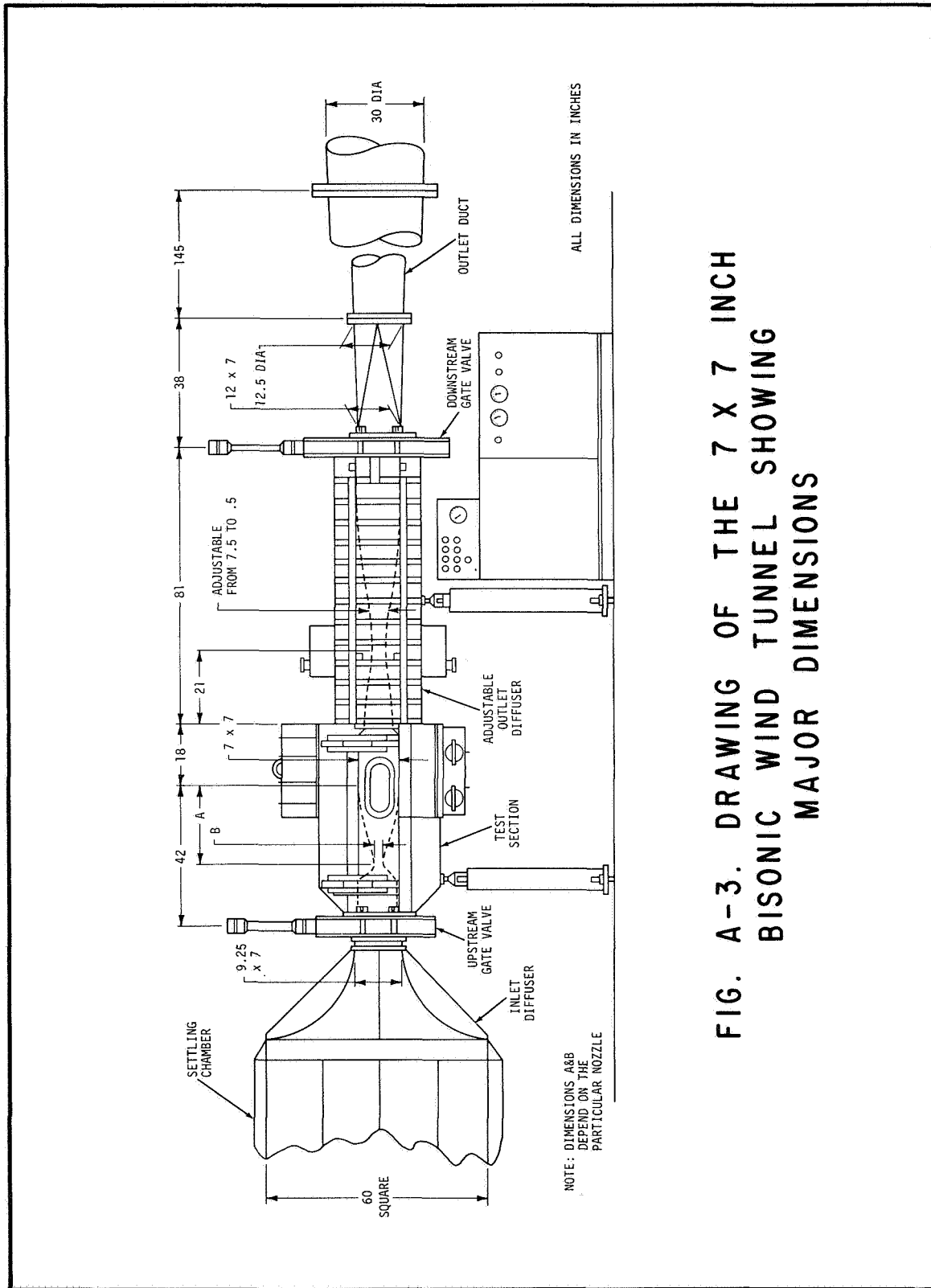


FIG. A-3. DRAWING OF THE 7 X 7 INCH
BISONIC WIND TUNNEL SHOWING
MAJOR DIMENSIONS

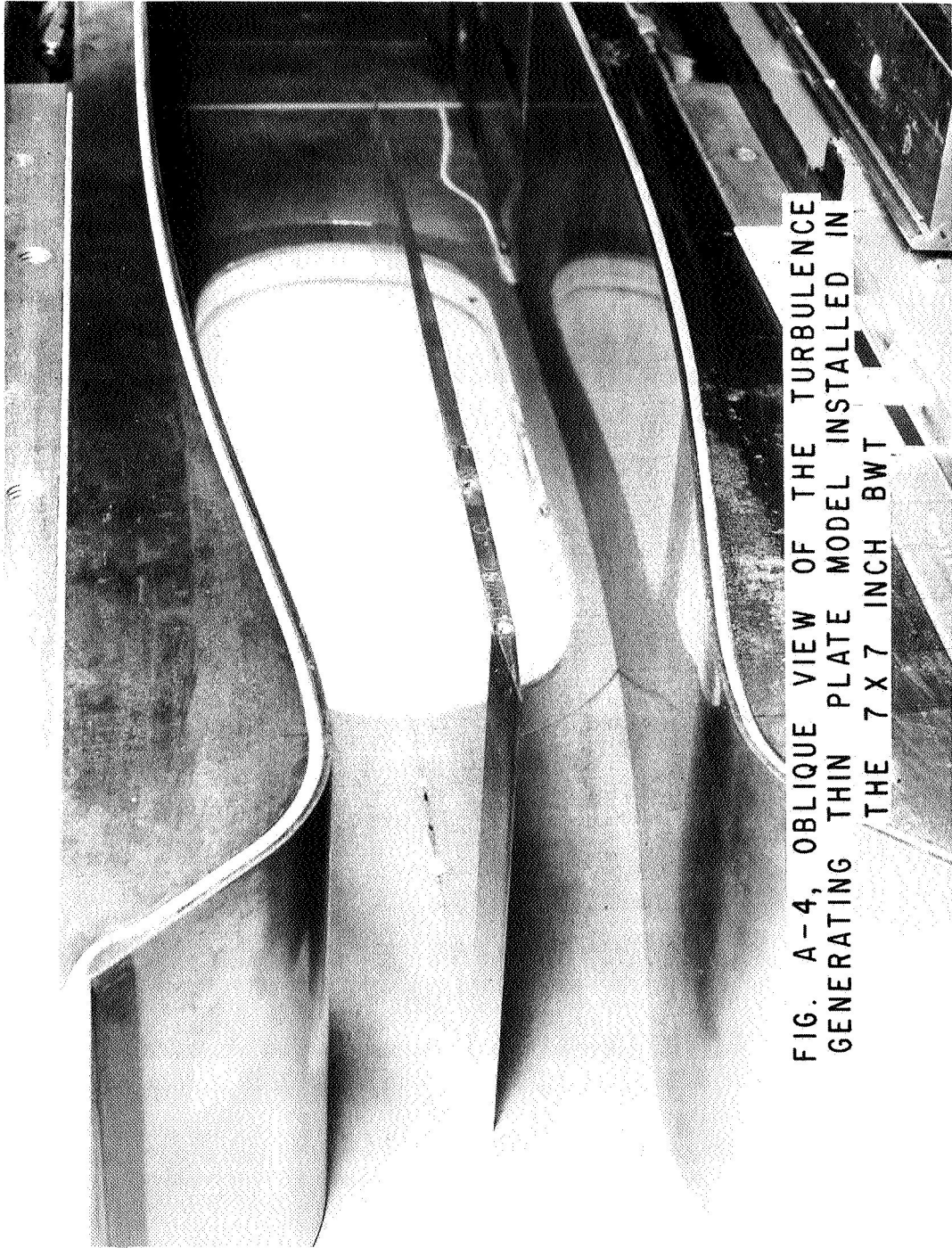


FIG. A-4, OBLIQUE VIEW OF THE TURBULENCE GENERATING THIN PLATE MODEL INSTALLED IN THE 7 X 7 INCH BWT

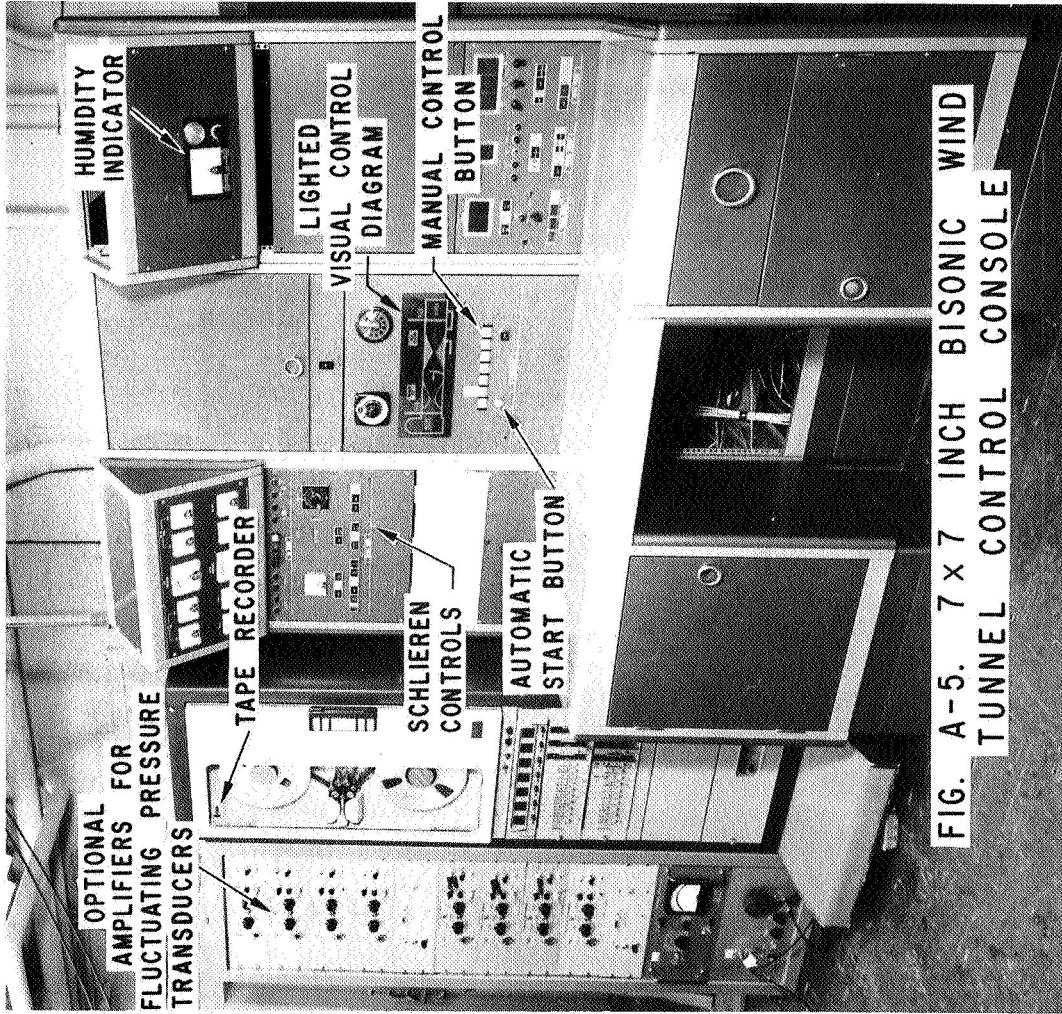


FIG. A-5. 7 x 7 INCH BISONIC WIND TUNNEL CONTROL CONSOLE

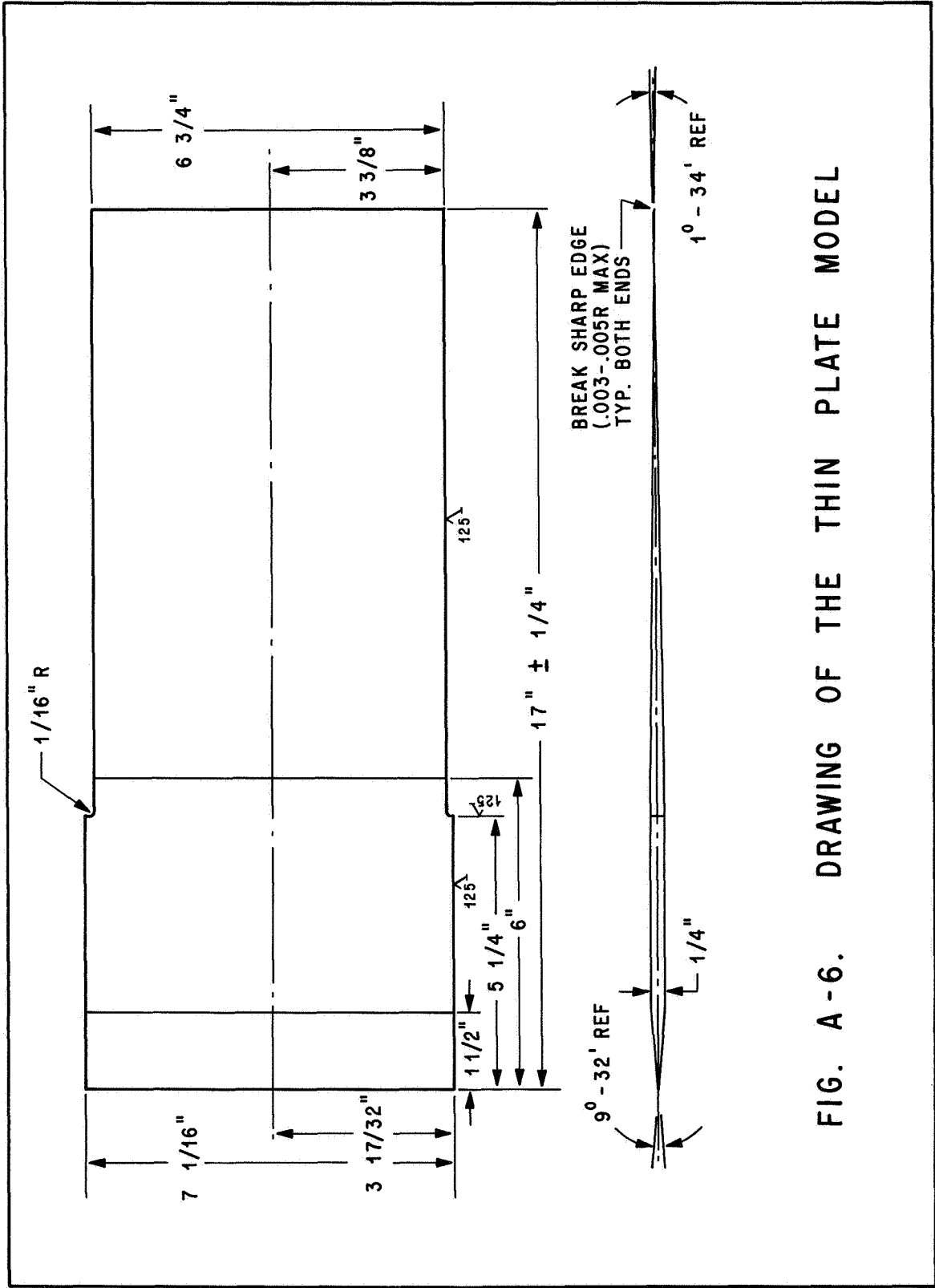


FIG. A-6. DRAWING OF THE THIN PLATE MODEL

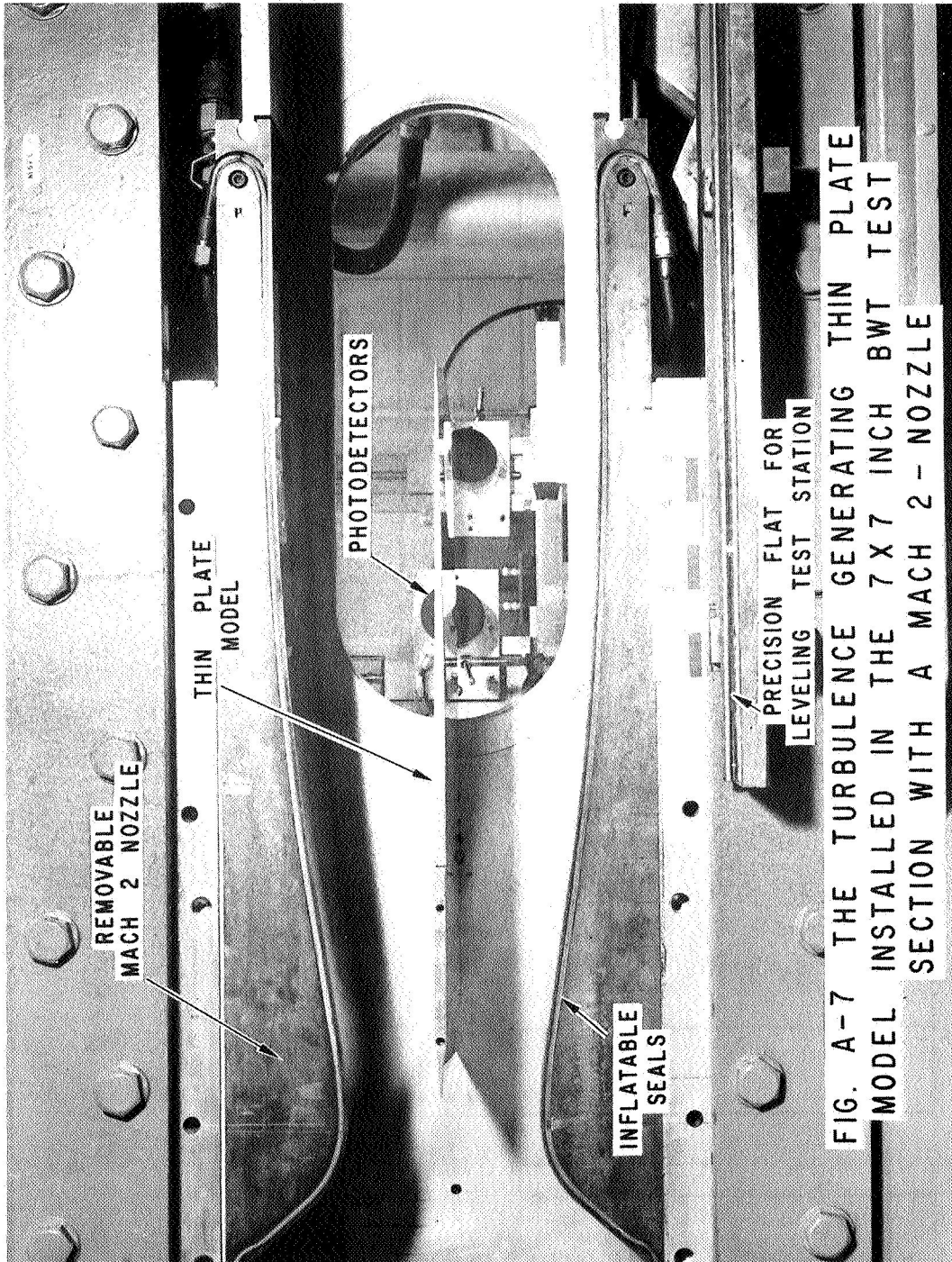


FIG. A-7 THE TURBULENCE GENERATING THIN PLATE MODEL INSTALLED IN THE 7 X 7 INCH BWT TEST SECTION WITH A MACH 2 - NOZZLE

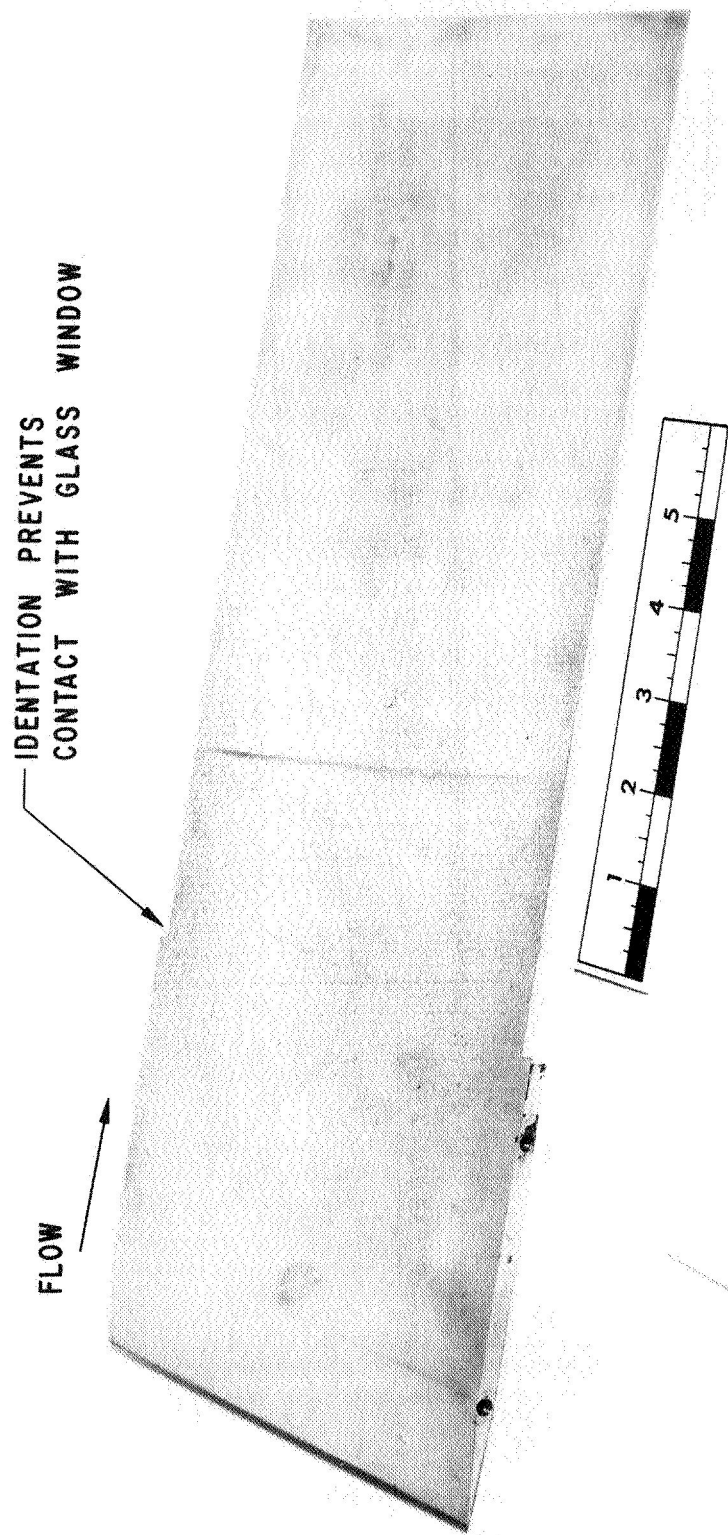


FIG. A-8 TWO DIMENSIONAL TURBULENCE GENERATING THIN PLATE MODEL

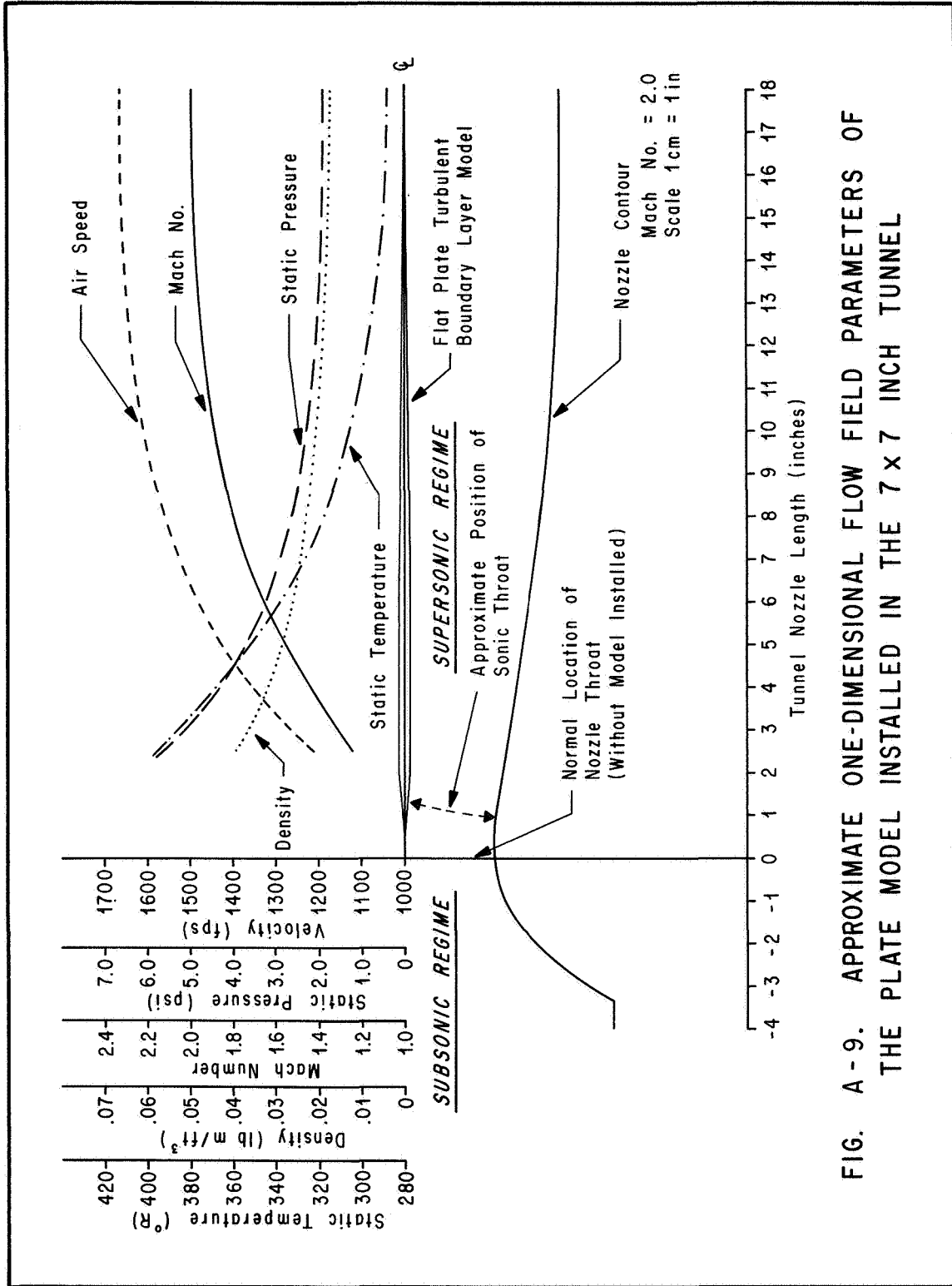


FIG. A-9. APPROXIMATE ONE-DIMENSIONAL FLOW FIELD PARAMETERS OF THE PLATE MODEL INSTALLED IN THE 7 X 7 INCH TUNNEL

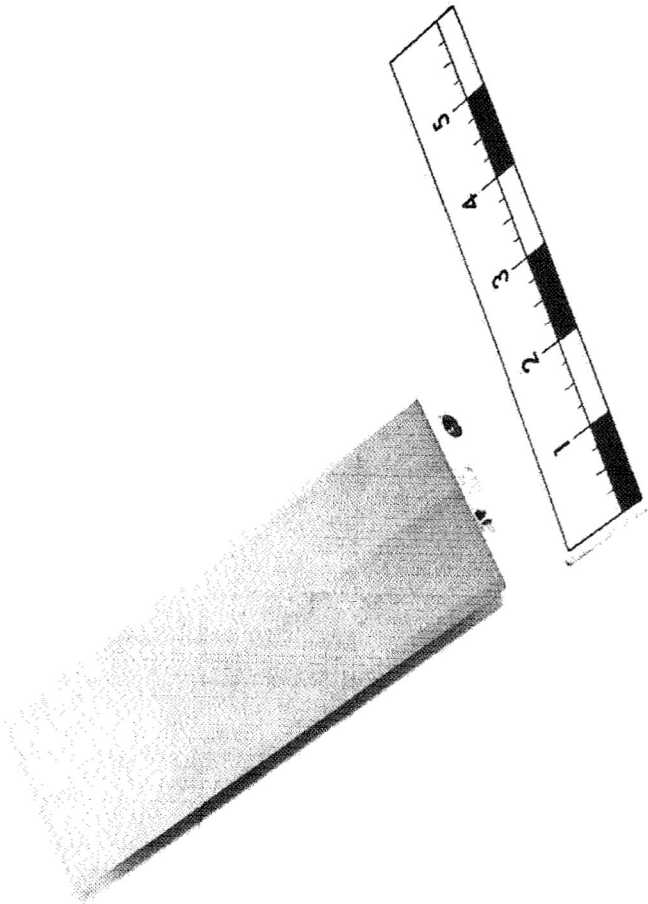
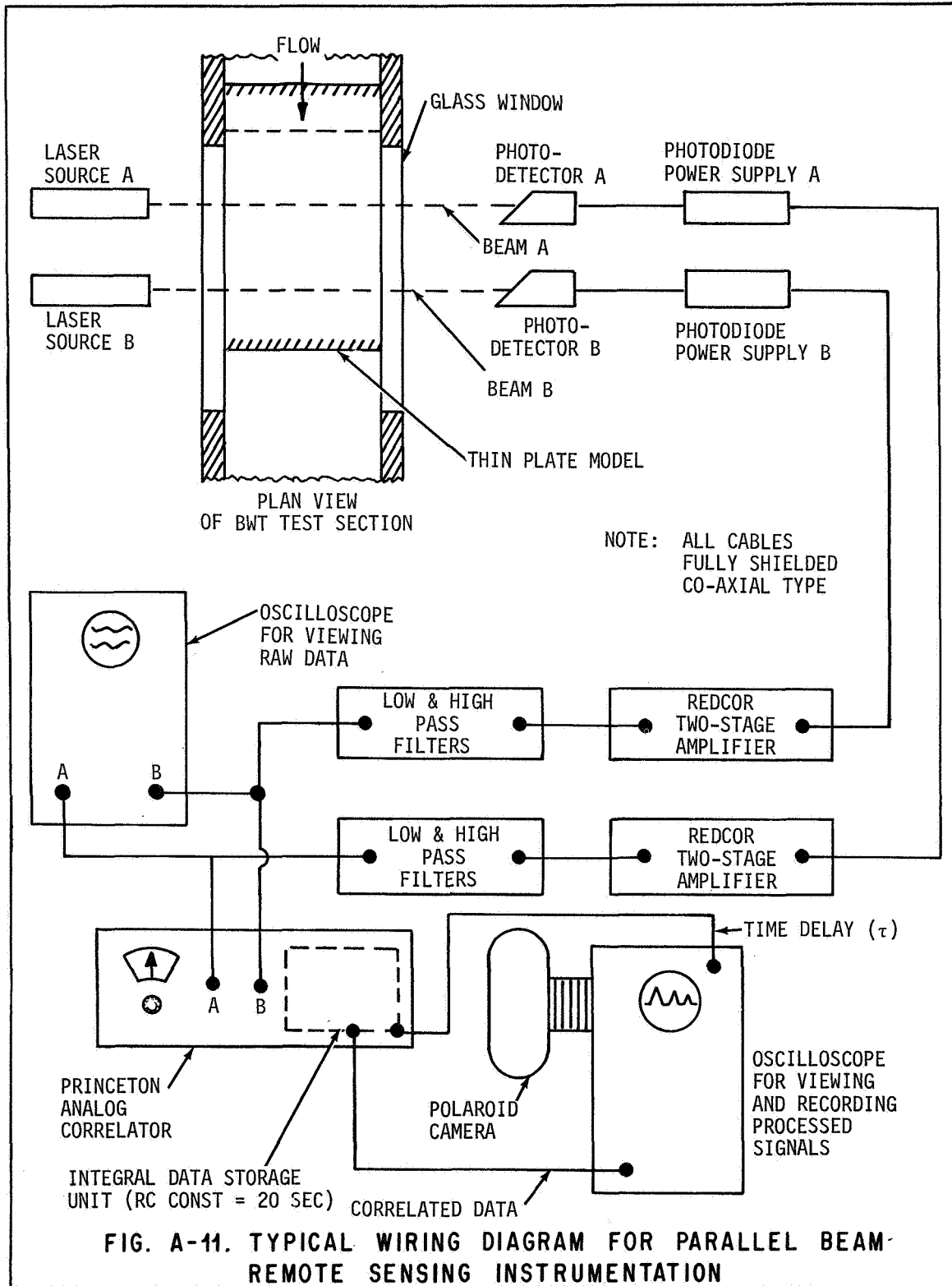


FIG. A-10 TWO-DIMENSIONAL WEDGE MODEL



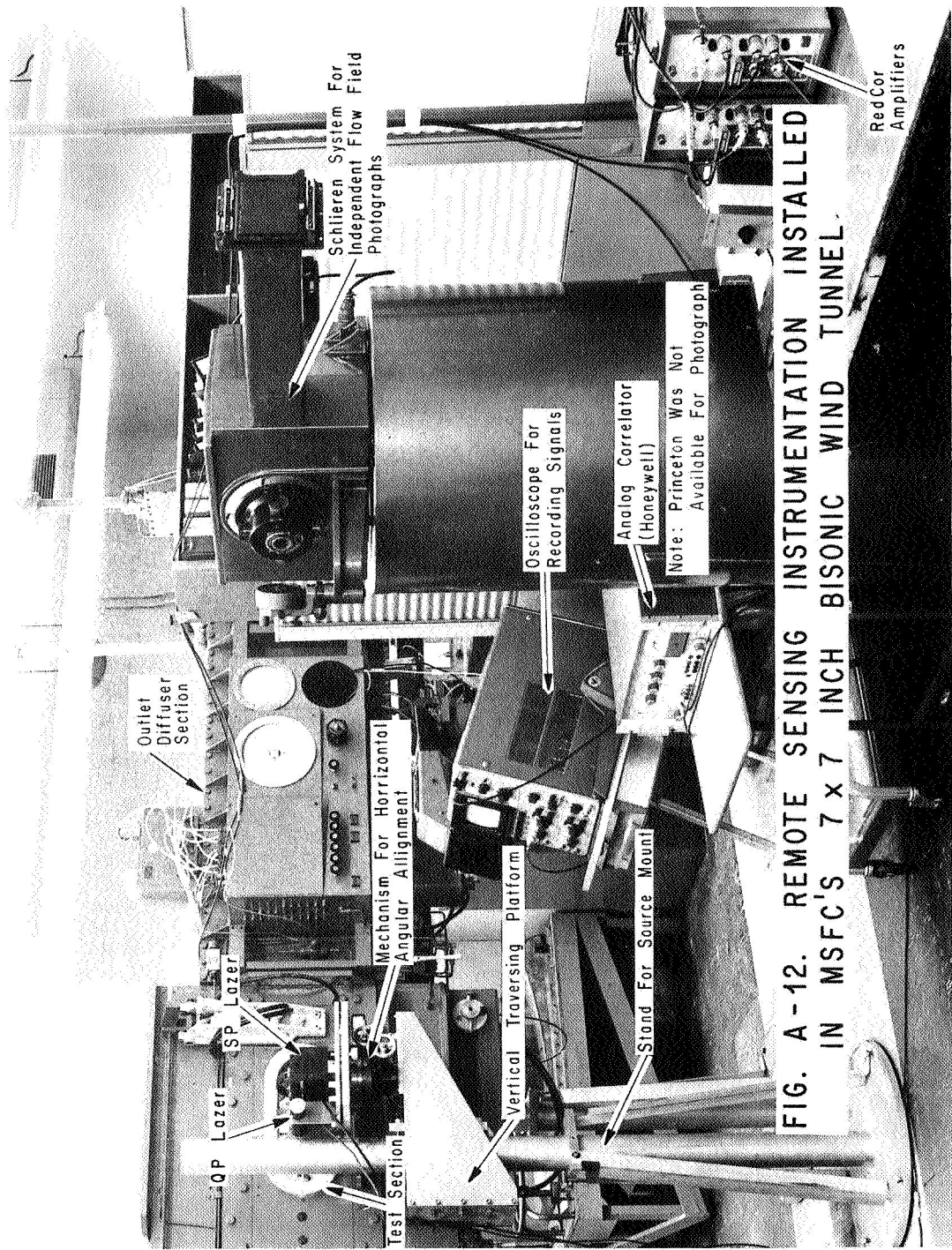
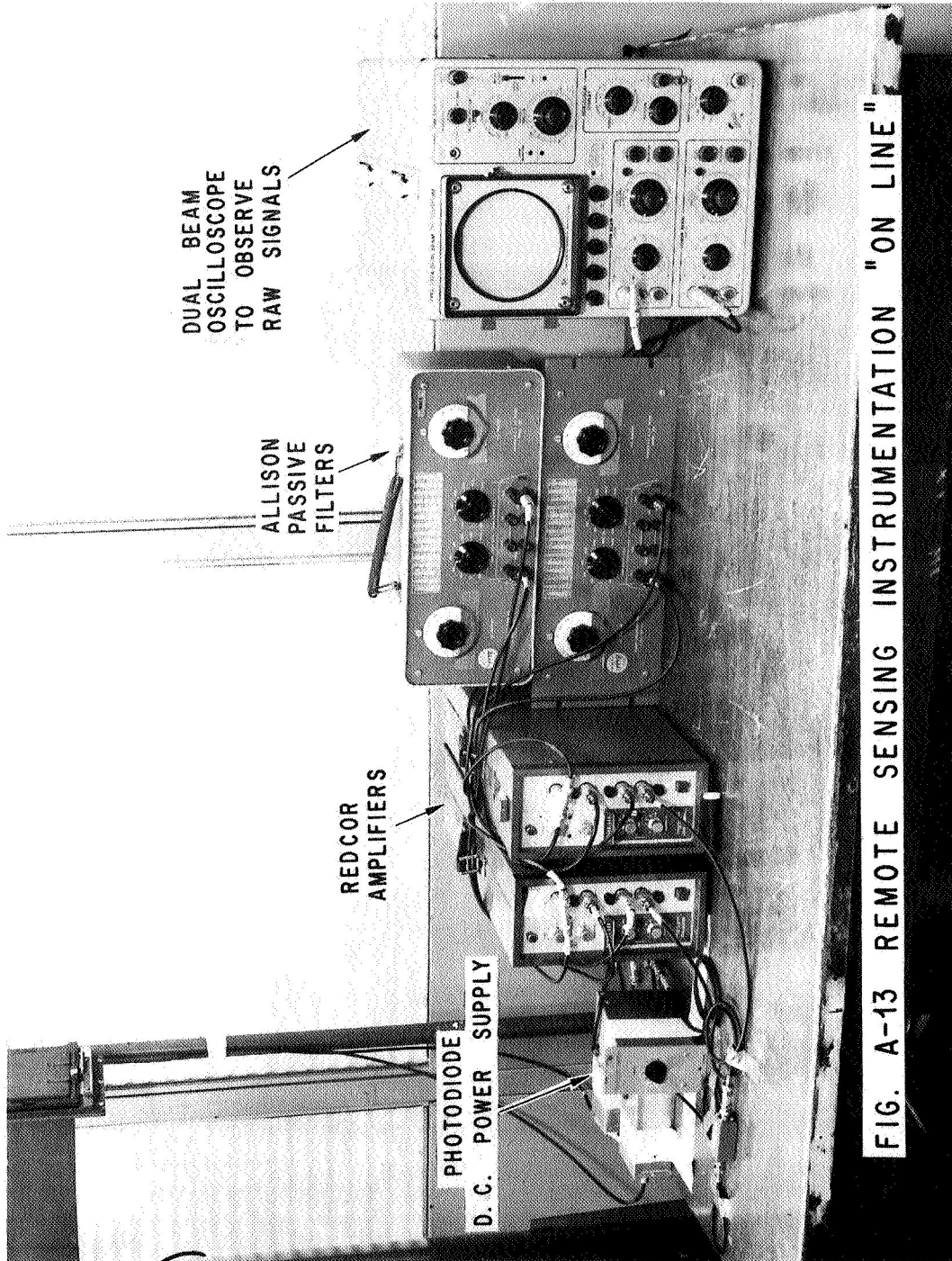


FIG. A-12. REMOTE SENSING INSTRUMENTATION INSTALLED IN MSFC'S 7 x 7 INCH BISONIC WIND TUNNEL.



DUAL BEAM
OSCILLOSCOPE
TO OBSERVE
RAW SIGNALS

ALLISON
PASSIVE
FILTERS

REDCOR
AMPLIFIERS

PHOTODIODE

D. C. POWER SUPPLY

FIG. A-13 REMOTE SENSING INSTRUMENTATION "ON LINE"

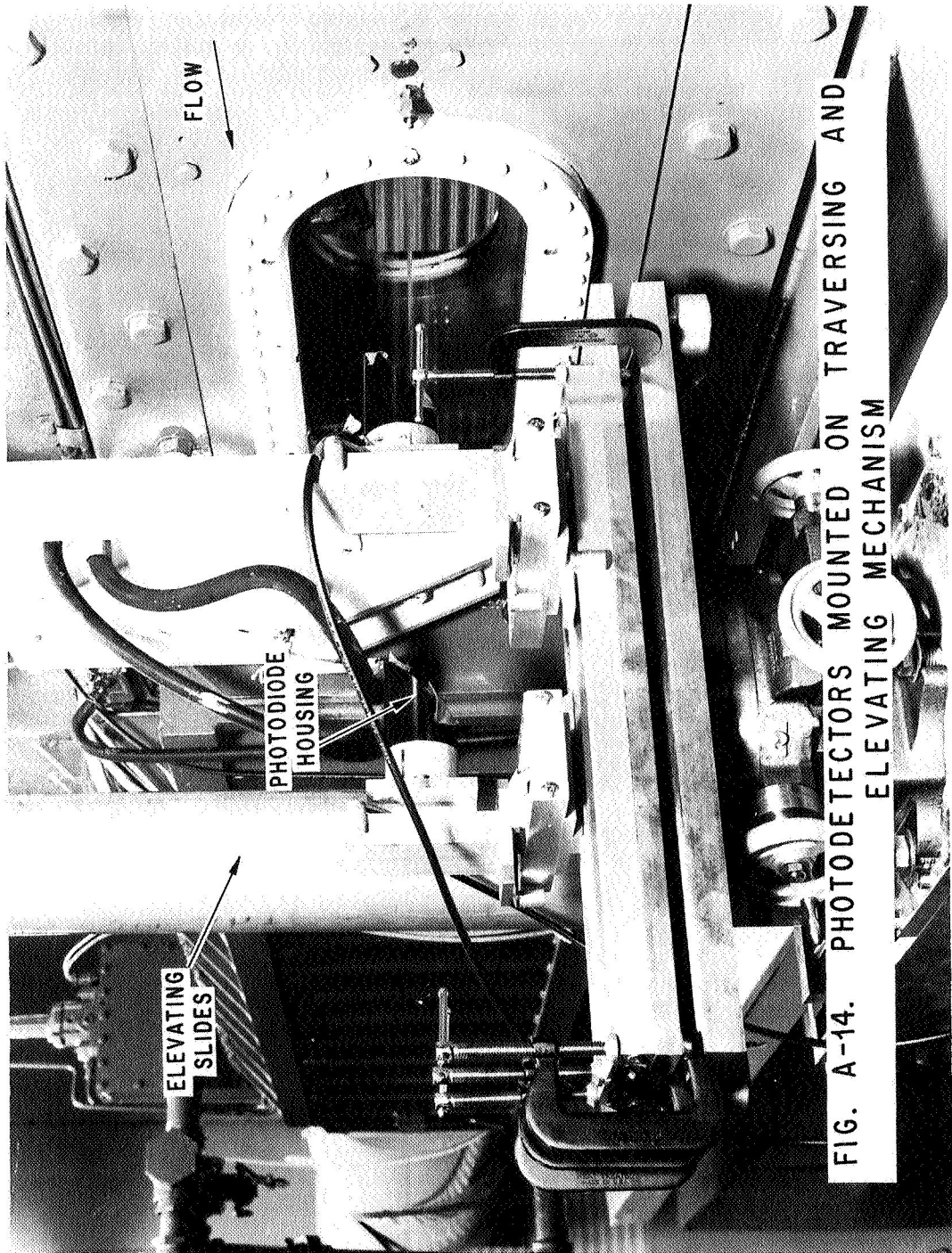


FIG. A-14. PHOTODETECTORS MOUNTED ON TRAVERSING AND ELEVATING MECHANISM

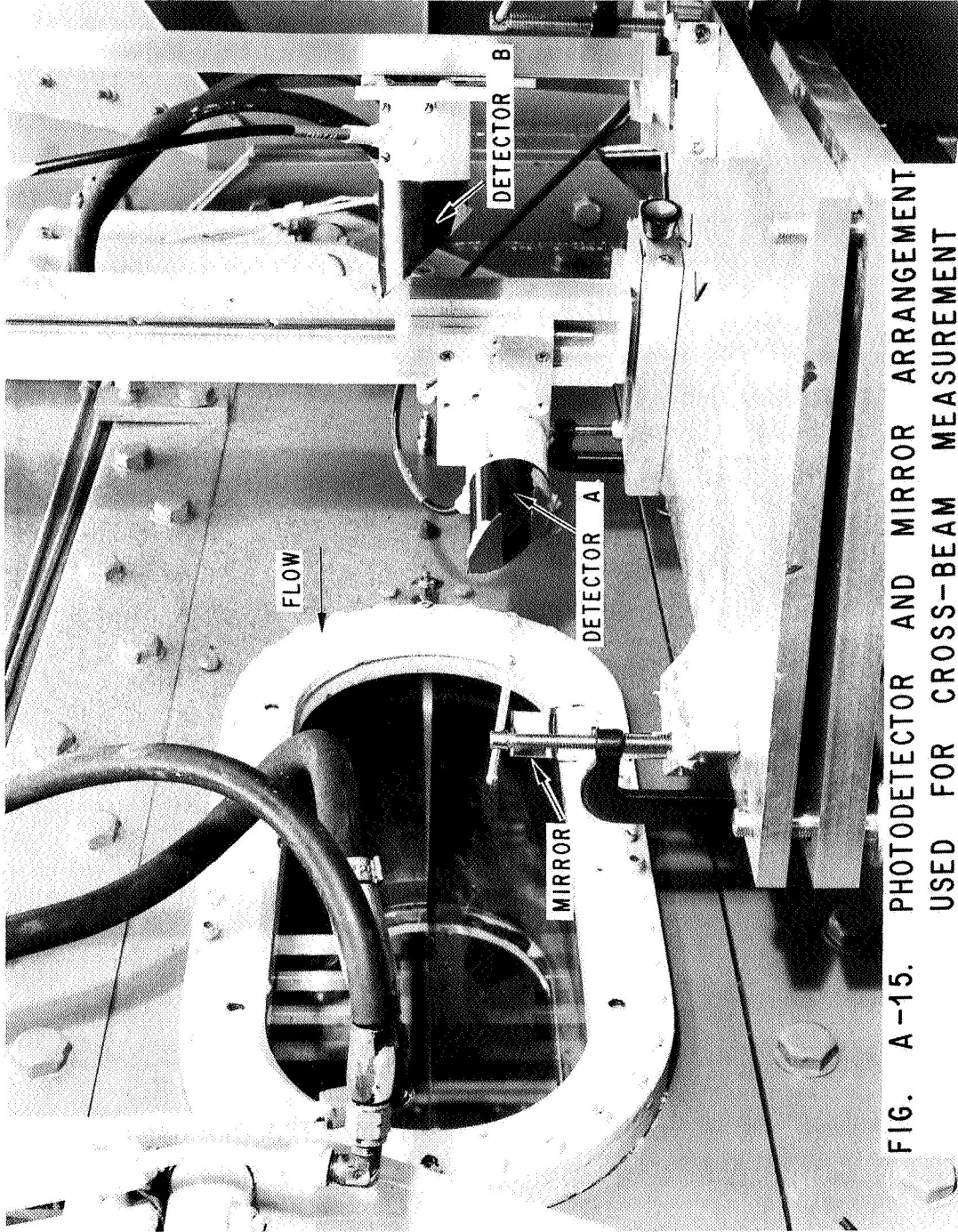


FIG. A-15. PHOTODETECTOR AND MIRROR ARRANGEMENT
USED FOR CROSS-BEAM MEASUREMENT

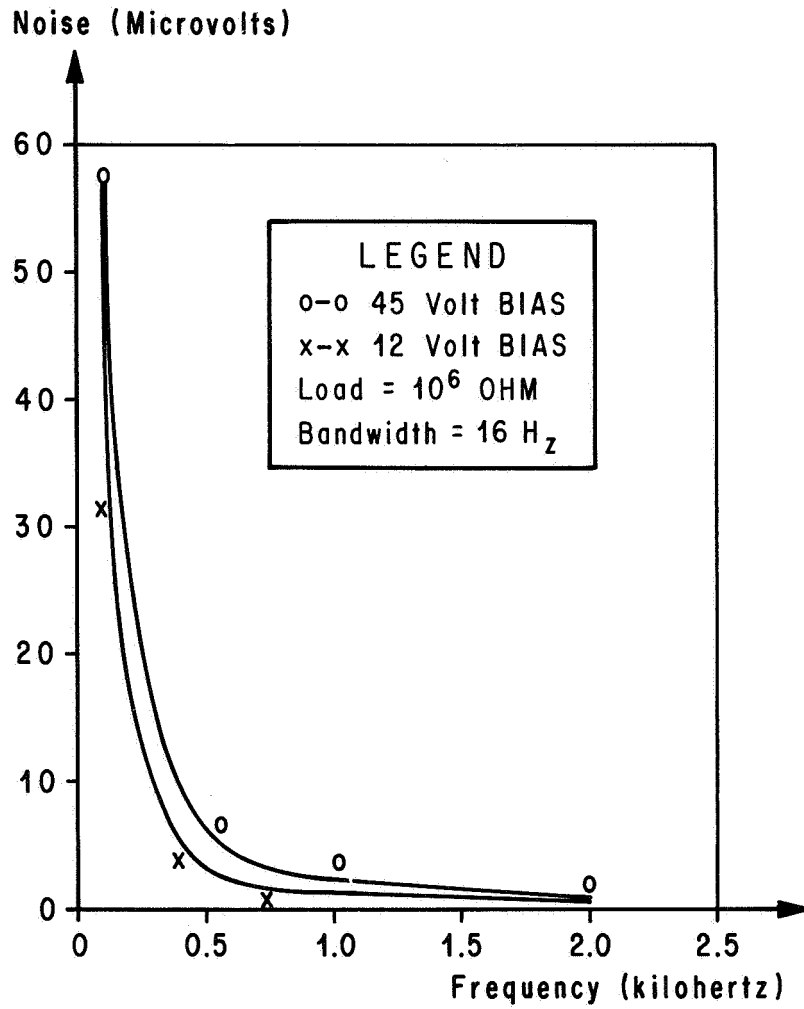
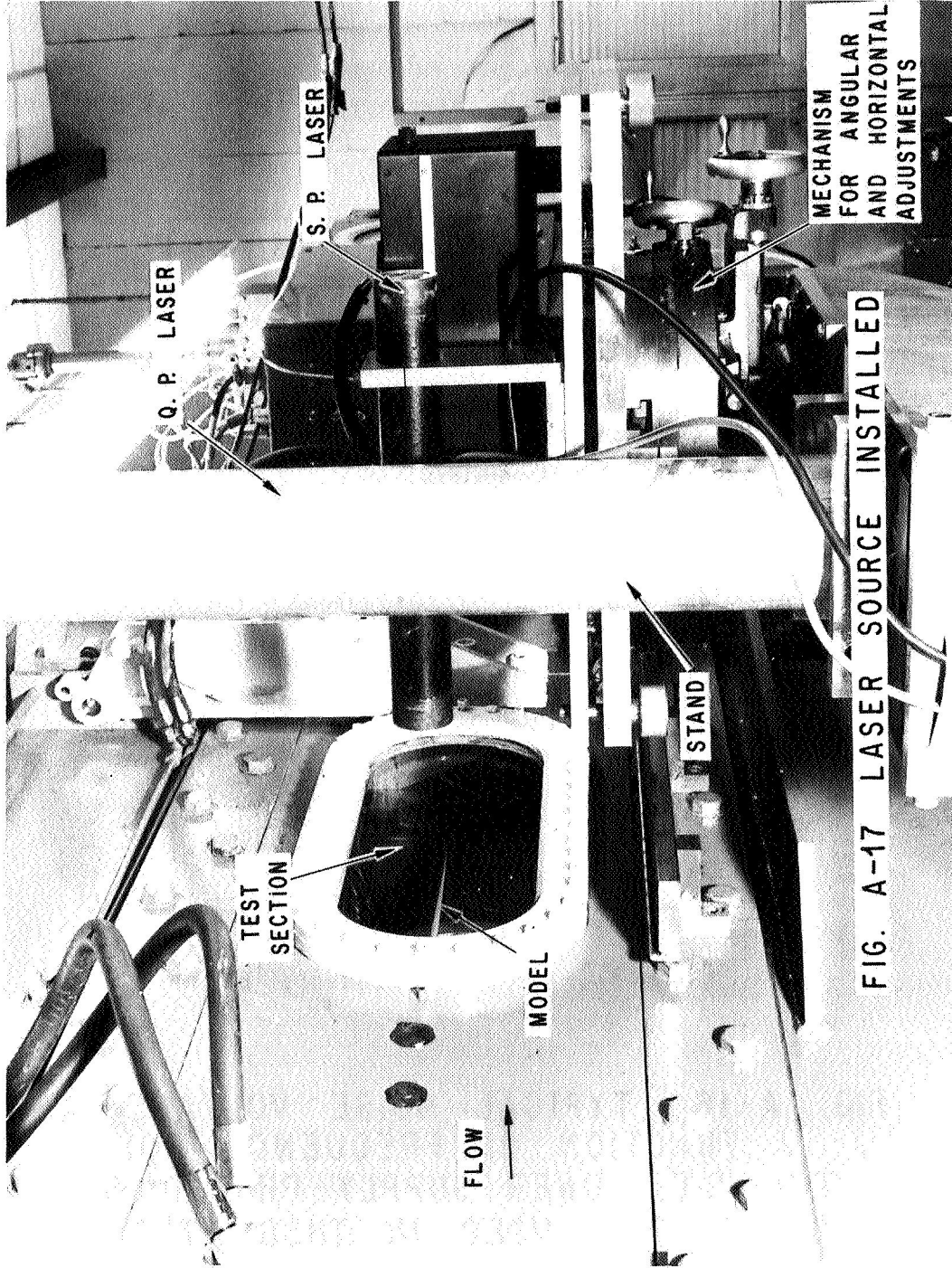


FIG. A-16. TYPICAL NOISE VOLTAGE AS A FUNCTION OF FREQUENCY FOR THE D.C. POWER SUPPLY-PHOTODIODE COMBINATION USED IN THESE TESTS



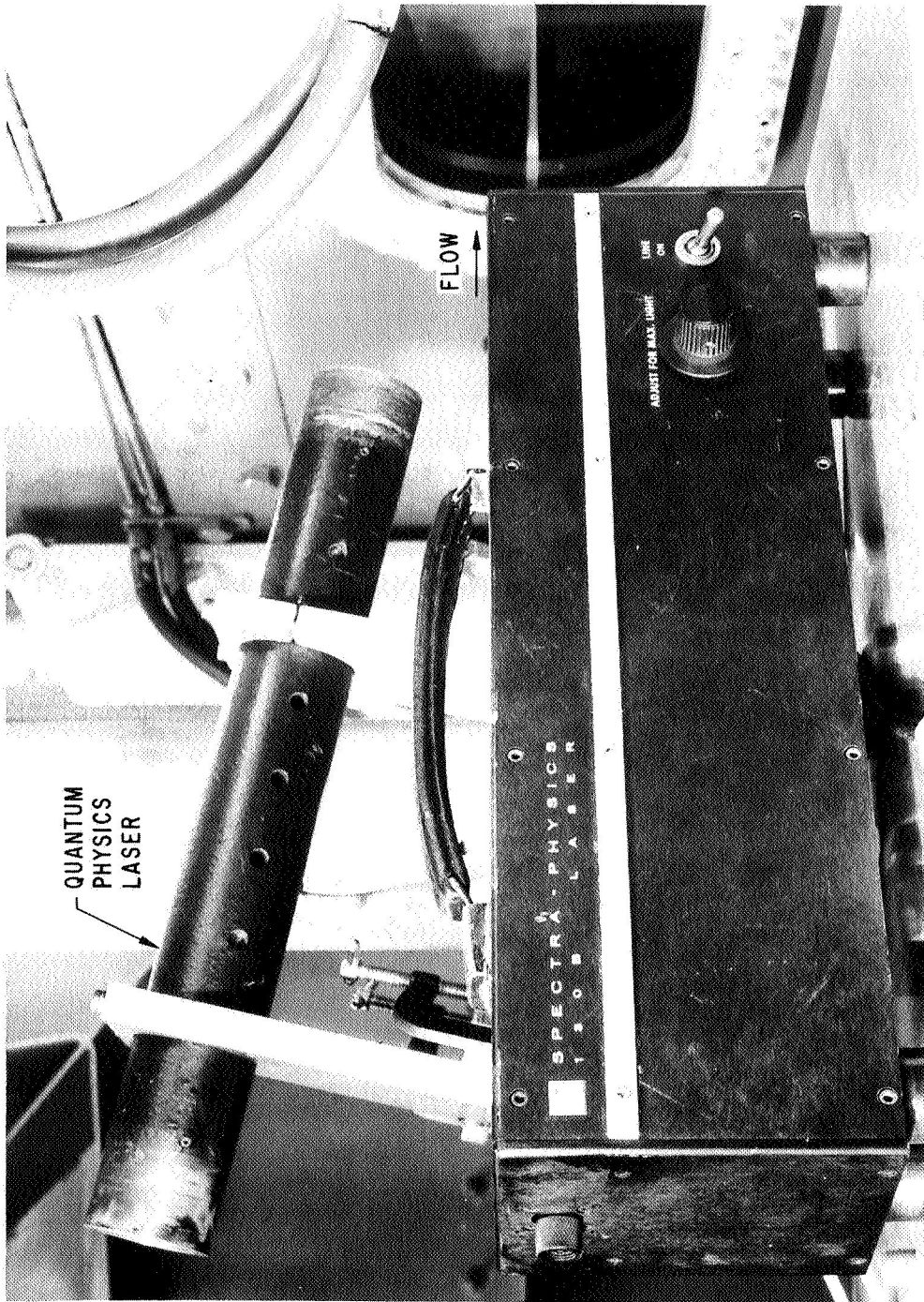


FIG. A-18 LASERS MOUNTED FOR TURBULENT FLOW MEASUREMENTS IN THE BWT BY THE CROSS-BEAM METHOD

APPENDIX B

COMMENTS ON THE EXPERIMENTAL NOISE STUDY IN MSFC'S 14-INCH TRISONIC WIND TUNNEL (TEST # TWT 395)

The experimental investigation presented in this report originated with the objective of conducting remote-sensing cross-beam experiments in MSFC's 14 x 14-Inch Trisonic Wind Tunnel to demonstrate the capability of measuring supersonic turbulence parameters using a laser source. The Trisonic Wind Tunnel cross-beam tests were conducted in the 14-inch tunnel special test section which is basically an annular nozzle with provisions for attaching an axisymmetric blunt-base body or a nozzle and vertical and horizontal windows for cross-beam access. Subsequent analysis of these cross-beam data showed essentially negative results because of an unsteady flow field in the Trisonic facility.

The major problem of the Trisonic facility was the almost complete domination of the data by facility-induced noise. This appendix was written to support the contention that excessive facility-induced mechanical and acoustic noise dominated the data and thus precluded fruitful cross-beam tests in the facility (at least until the remote-sensing system has been further developed). The reasons why the 14-inch tunnel was not satisfactory for remotely sensed measurements are discussed in the following paragraphs.

Figure B-1 shows fifty-seven qualitative correlations of various beams and accelerometers which were located both inside and outside the turbulent flow field of interest. The first three rows across the top depict the autocorrelation of the individual horizontal and vertical beams and horizontally and vertically oriented accelerometers which were mounted on the outer wall of the STS. Sixty percent of these show definite periodic trends which are detrimental to the extraction of useful turbulent flow information.

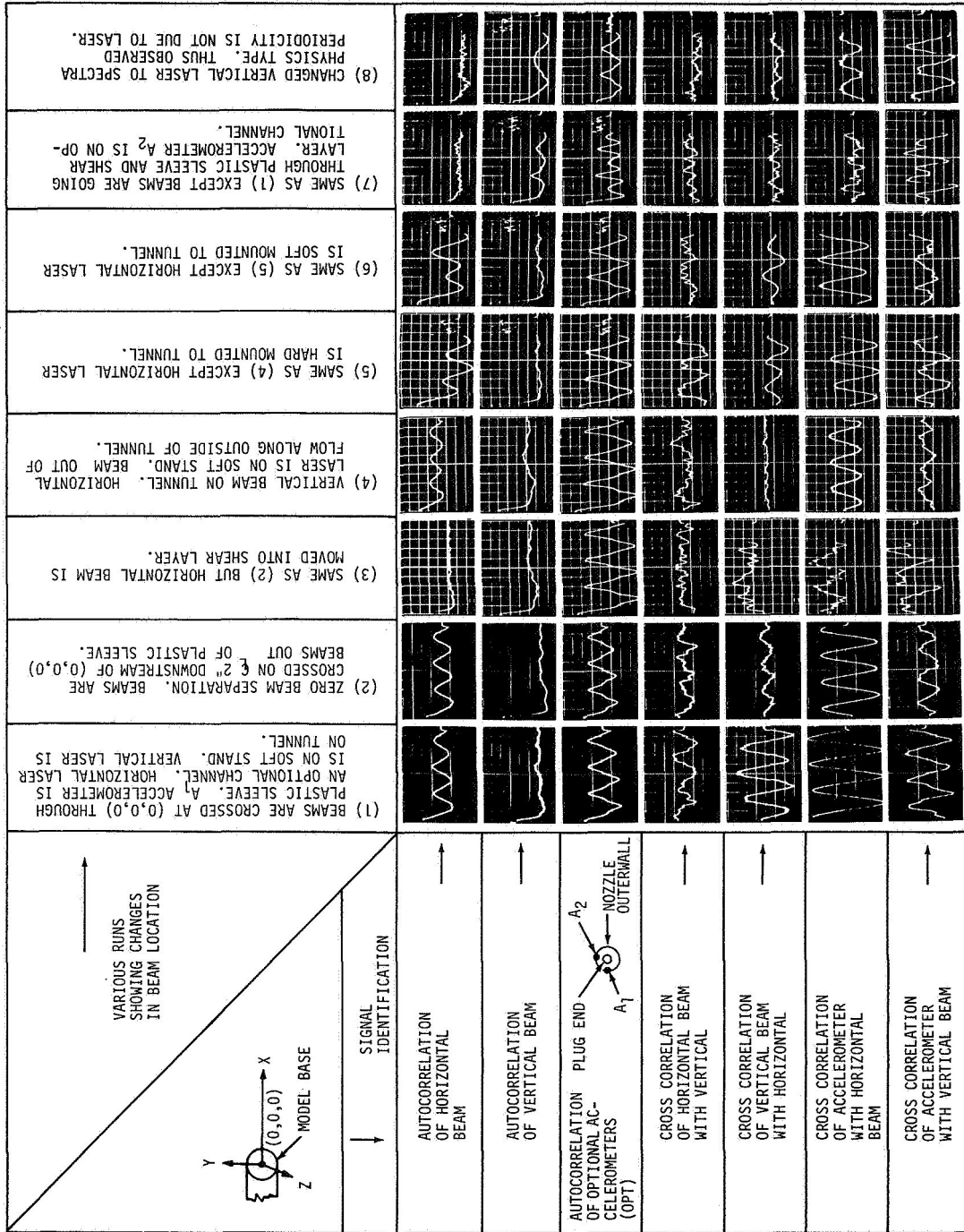
The four remaining rows across the bottom depict cross-correlation of the horizontal and vertical beams and cross-correlation of the single beam signals with the signal from the individual accelerometers. This latter device gives a qualitative indication of the relative magnitude and frequency of noise common between the flow field and structure. As for the autocorrelations, these cross-correlations are dominated by an extraneous periodic noise. Attempts to filter these data were not successful because of an adverse signal-to-noise ratio.

Figure B-1, Column (1), shows an attempt to obtain an intensity traverse. This should have resulted in a correlation function with a minor peak at zero time lag since the beams are crossed in a region of low turbulence. However, the peak was masked by a periodic signal of 1380 cps. A great deal of this noise can be attributed to structural vibration. This is indicated by the cross-correlation of the accelerometer with each individual beam, since definite periodic correlations of significant magnitudes apparently exist between them. Also it may be noticed that these beams were going through a plastic sleeve extension of the nozzle outer wall which probably contributed to the correlation. Moving the beams downstream two inches (out of the plastic sleeve) apparently did not improve the situation significantly (see Column 2). The flow conditions and coordinates of column 3 are the same as (1) and (2) except a dominant peak should have been obtained at zero time lag, since the correlation volume is located in a dense shear layer. In Column (4) the correlation showed a definite mechanical or acoustical vibration between beams because one beam was completely removed from the flow and directed along side of the tunnel wall. Furthermore, Columns 4, 6, 7 and 8 depict various attempts to soft-mount the lasers and stands, but this apparently did not eliminate the vibrations.

Upon analysis of these data, the following conclusions and recommendations were made:

- ° The flow field, structure and surrounding environment in the 14-inch TWT (STS) facility were dominated by an extraneous periodic noise which precluded ascertaining useful data at the time of the test.
- ° Attempts at filtering these raw data signals and various methods of soft-mounting the lasers and detectors did not alleviate the situation so that flow related correlation could be obtained.
- ° Remote sensing measurements in the 14 x 14-inch wind tunnel might be possible after (1) more analysis of the 14-inch TWT noise problem, and (2) development of techniques to improve signal-to-noise ratio of the remote sensing system.
- ° A different facility was needed with a lower facility-induced noise level.

These results essentially led to the selection of the 7 x 7-inch BWT facility for the immediate future development of the remote-sensing tool. This approach appeared to offer the most economical method of expediting development of the remote-sensing system for measuring supersonic turbulence.



ORDINATES NOT TO SCALE, ABSCISSA 2.5 MILLISEC. FULL SCALE.

Figure B-1. CROSS BEAM TEST IN MSFC'S 14" TRISONIC WIND TUNNEL

APPENDIX C

UNKNOWN ANOMALIES IN DATA ACQUISITION SYSTEM

Unknown anomalies should be expected in any research work; the research involves identifying and resolving them. The anomalies in the system were (1) low-pass filters set too low, thus blocking significant amounts of data; (2) use of attenuation after amplification, which, combined with low maximum amplifier input voltage, probably resulted in clipping of signals; (3) high-pass filter set too low, thus allowing undesirable flow noise and facility-induced noise in the signals; (4) filtering low frequencies (e.g., 60 cyc/sec) with large amplitudes before the run, probably causing clipping of signals during the run, which was not detected after the clipped signal was filtered; and (5) photodetectors and other possible points of contact between grounds were not isolated (not always a source of trouble).

As can be seen, the problem areas were associated with the amplifiers (i.e., clipping) and filtering methods.

REFERENCES

1. Cambel, A. B. and B. H. Jennings, Gas Dynamics, McGraw-Hill Book Co., Inc., New York, 1958.
2. Weinberg, F. J., Optics of Flames, Butterworth and Co., Washington, D. C., 1963.
3. Liepmann and Roshko, Elements of Gas Dynamics, John Wiley & Son, Inc., 1957.
4. Bendat, J. S. and A. G. Piersol, Measurement and Analysis of Random Data, John Wiley, New York, 1966.
5. Funk, B. H., Jr., "Theoretical Application of the 'One-Shot' Auto-correlation Technique to the Determination of Atmospheric Ground Wind Speed and Direction," MSFC Memo No. R-AERO-A-68-37, December 11, 1968.
6. Su, M. Y., "Statistical Error and Required Averaging Time for Evaluating Cross-Correlation of Crossed-Beam Data," Nortronics-Huntsville Memo No. M-794-8-362, May 24, 1968.
7. Holderer, O. C., "The Redstone Arsenal 7" x 7" Supersonic Wind Tunnel," Ordnance Missile Laboratory, Redstone Arsenal, Huntsville, Alabama, Report No. IR7, July 1955.
8. Fisher, M. J. and R. J. Damkevala, "Fundamental Considerations of the Crossed-Beam Correlation Technique (Final Report)," IIT Research Institute, January 1969.

OPTICAL PROBING OF SUPERSONIC AERODYNAMIC TURBULENCE
WITH STATISTICAL CORRELATIONS

PHASE I: FEASIBILITY

by B. H. Funk, Jr. and H. A. Cikanek, Jr.

The information in this report has been reviewed for security classification. Review of any information concerning Department of Defense or Atomic Energy Commission programs has been made by the MSFC Security Classification Officer. This report, in its entirety, has been determined to be unclassified.

This document has also been reviewed and approved for technical accuracy.



W. K. Dahm
Chief, Aerophysics Division



E. D. Geissler
Director, Aero-Astrodynamic Laboratory

DISTRIBUTION

DIR

Dr. von Braun
Mr. Shepherd

S& E-ASTR

Mr. Hoberg
Dr. Decher
Dr. Randall

S& E-COMP

Mr. E. Hopper
Mr. J. Jones

S& E-SSL

Mr. Heller
Mr. Snoddy
Mr. Shelton

S& E-AS

Mr. Williams
Mr. Thomae

S& E-R

Dr. W. G. Johnson
Mr. Attaya
Mr. Miles
Mr. Hopper

S& E-ASTN-PTD

Mr. Hopson

PM-DIR

PM-AA

Mr. Belew

MS-IP

MS-IL (6)

I-CO-CH

Col. Hirsch

R-AERO

Dr. Geissler
Mr. Dahm
Mr. Wilson
Mr. Linsley
Mr. Felix
Mr. Reed
Mr. Lindberg
Mr. W. Vaughan
Mr. Turner
Mr. Kaufman
Dr. F. Krause
Mr. Holderer
Mr. Heaman
Mr. Simon
Mr. Huffaker
Mr. Ellner
Mr. Schutzenhofer
Mr. Forney
Mr. Kadrmas
Mr. Thomison
Mr. Pickelner
Dr. Heybey
Mr. I. Jones
Mr. Johnston
Mr. Funk (25)
Mr. Cummings
Mr. Murphree
Mr. Lavender
Mr. Jandebeur

Mr. Brewer
Mr. Greenwood
Mr. H. Bush
Mr. Neighbors
Mr. W. Davis
Mr. J. Carter
Mr. Wilhold
Mr. J. Jones
Mr. J. Sims
Mr. Struck

RSIC

AST-U

Col. Mohlere

A& TS-TU (6)

A& TS-MS-H

PM-PR-M

A& TS-PAT

Mr. L. D. Wofford, Jr.

AD-S

DEP-T

EXTERNAL DISTRIBUTION

Technical & Sci. Info. Facility (25)
 Box 33
 College Park, Md.
 Attn: NASA Rep. (S-AK/RKT)

IITRI (Continued)
 Attn: Mr. Norman
 Mr. Wachowski
 Mr. Cann

NASA Headquarters (2)
 NASA
 Washington, D. C. 20546

Nortronics-Huntsville
 Technology Dr.
 Huntsville, Ala. 35805

NASA - Langley Research Center (2)
 Langley Field,
 Hampton, Virginia 23365

Attn: Mr. Ryan
 Mr. Bennett
 Dr. Su
 Mr. Barnett
 Mr. Cikanek
 Mr. Pooley
 Mr. Tidmore
 Mr. Lindstrom
 Gen. Barclay
 Mr. Miller

NASA - Goddard Space Flight Center (2)
 Greenbelt, Md. 20771

NASA - Flight Research Center (2)
 Edwards, Calif. 93523

NASA - Ames Research Center (2)
 Moffett Field
 Mountain View, Calif. 94035

ESSA
 National Bureau of Standards Bldg.
 Boulder, Colorado 80302

NASA - Lewis Research Center (2)
 21000 Brookpark Rd.
 Cleveland, Ohio 44135

Attn: Dr. B. Bean
 Mr. McGavin
 Dr. G. Little
 Mr. Abshire
 Mr. Sweecy
 Dr. Derr

NASA - JFK Space Center (2)
 Kennedy Space Center, Fla. 32899

Jet Propulsion Lab. (2)
 Calif. Inst. of Tech.
 4800 Oak Grove Dr.
 Pasadena, Calif. 91103

FAA - NO-10
 800 Independence Ave. SW
 Washington, D. C. 20590
 Attn: Dr. K. Power
 Dr. J. Powers

IITRI
 10 W. 35th St.
 Chicago, Ill. 60616
 Attn: Dr. Damkevala
 Dr. Wilson
 Col. Ferrell

NASA Headquarters
 Director of OART
 RAO, Mr. McGowan
 RV-I, Mr. Cerreta
 SAB, Mr. George
 REI, Dr. Menzel
 RV-2, Mr. Michel
 RAA, Mr. Parkinson
 RAP, Mr. Rekos
 RRF, Mr. Schwartz
 3M, Mr. Badgley

Rocketdyne
 6630 Canoga Avenue
 Canoga Park, California 91304
 Attn: R. L. Proffit
 G. L. Cline

EXTERNAL DISTRIBUTION (Continued)

NASA Headquarters (Cont'd)

SM, Mr. Brockman
SV, Mr. Salmanson
SFM, Mr. Spreen
SF, Mr. Tepper
RVI, Mr. DeMeritt
RVI, Mr. Green
MA, Mr. Reiffel
RV-2, Mr. Rosche
RR, Dr. Kurzweg
RRP, Mr. Danberg
MTP, Mr. Peil
RVA, Mr. Underwood
REI, Mr. Vacca

A&M College

Normal, Ala. 35762
Attn: Prof. H. Foster
Mr. J. Shipman

University of Oklahoma
College of Engineering
Norman, Okla. 73069
Attn: Dean F. Block
Dr. Canfield
Dr. Fowler

Dr. Lin
University of Wisconsin
Madison, Wisconsin

Mr. Ajit Kumar Ray
Univ. of Ottawa
Dept. of Math.
Ottawa 2, Canada

Mr. A. S. Mujumdar
Pulp & Paper Res. Inst. of Canada
570 St. John's Rd.
Pointe-Claire, P.Q.
Canada

Mr. T. W. Kao
Dept. of Space Sci. & Appl. Phys.
The Catholic Univ. of America
Washington, D. C. 20017

Dr. J. E. Mitchell
Esso Res. & Eng. Co.
P. O. Box 45
Linden, N. J. 07036

Mr. Philemon Baw
Bureau of Engr. Res.
Rutgers - The State Univ.
College of Engineering
New Brunswick, N. J. 08903

Mr. Robert Torrest
Chem. Engr. Dept.
Univ. of Minnesota
Minneapolis, Minnesota 55455

Mr. G. R. Verma
Dept. of Math.
Univ. of Rhode Island
Kingston, R. I. 02881

Dr. M. A. Badri
Dept. of Aeronautical Engr.
Indian Inst. of Science
Bangalore-12, India

Mr. R. Antonia
The University of Sydney
Dept. of Mech. Engr.
Sydney, N.S.W.
Australia

Mr. H. W. Thomas
Nat. Inst. for Res. in Dairying
Shinfield, Reading
England

EXTERNAL DISTRIBUTION (Continued)

Dr. H. P. Pao
Dept. of Space Sci. & Appl. Phys.
The Catholic Univ. of America
Washington, D. C. 20017

Mr. E. A. Trabko
Cornell Aeronautical Lab., Inc.
P. O. Box 235
Buffalo, N. Y. 14221

Mr. Ta-jin Kuo
The Pa. State Univ.
Dept. of Aeronautical Engr.
233 Hammond Bldg.
Univ. Park, Pennsylvania

Mr. Fritz Bien
Univ. of Calif. San Diego
Dept. of Aerospace & Mech. Engr. Sci.
P. O. Box 109
La Jolla, Calif. 92038

Lt. T. M. Weeks, FDME
Wright-Patterson AFB, Ohio 45433

Mr. Earl Logan, Jr.
Assoc. Prof. of Engr.
Arizona State Univ.
Tempe, Arizona

Prof. Geo. F. Carrier
Div. of Engr. & Appl. Phys.
Harvard Univ.
Pierce Hall
Cambridge, Mass. 02138

Dr. Cohen
United Aircraft Res. Lab.
Silverlane East
Hartford, Conn.

Mr. D. Heckman
CARDE
P. O. 1427
Quebec, Canada

Mr. D. Ellington
CARDE
P. O. 1427
Quebec, Canada

U. S. Dept. of Interior
Bureau of Mines
Dr. Joseph M. Singer
Explosives Res. Center
4800 Forbes Ave.
Pittsburgh, Pa. 15213

Mr. J. L. Richardson
Manager, Appl. Chem.
Aeroneutronic Div.
Philco Corp.
Ford Road
Newport Beach, Calif.

Dr. Srbslav Zivanovi
Senior Res. Engr.
Aerospace Operator
Defense Systems Div.
General Motors Corp.
6767 Hollister Ave.
Goleta, Calif.

Mr. S. Molder
McGill Univ.
805 Sherbrooke West
Montreal 2, Canada

Madame G. Comte-Bellot
Laboratoires de Mecanique
des Fluides
Universite de Grenoble
44-46 Avenue Felix-Viallet
Grenoble, France

Mr. Roland E. Lee
Aerophysics Div.
U. S. Naval Ordnance Lab.
White Oak
Silver Spring, Md.

EXTERNAL DISTRIBUTION (Continued)

Mr. W. G. Tiederman
Shell Developments
Emeryville, Calif.

Mr. Pat Harney
AFCRL/CRES
Bedford, Mass. 01730

Mr. Nicholas Trentacoste
Polytechnic Inst. of Brooklyn
Aerospace Engr.
527 Atlantic Ave.
Freeport, N. Y.

Mr. D. Fultz
Hydrody Lab.
Univ. of Chicago
Chicago, Ill. 60637

Dr. I. T. Osgerby
Hypervelocity Br.
Von Karman Facility
ARO, Inc.
Arnold Air Force Station, Tenn.

Mr. N. Engler
Univ. of Dayton
Res. Inst.
300 College Park Ave.
Dayton, Ohio 45409

Mr. Charles I. Beard
Geo-Astrophysics Lab.
Boeing Sci. Res. Labs.
P. O. Box 3981
Seattle, Washington 98124

Mr. W. Mermagen
U. S. Army
Ballistic Res. Lab.
Aberdeen Proving Gd., Md. 21005

Mr. Jay Fox
TRW Systems
One Space Park
Redondo Beach, Calif. 90278

Mr. F. Badgley
Travelers Res. Center
250 Constitution Plaza
Hartford, Conn. 06103

Mr. H. F. Lewis
5 MC Arc Heater Section
LORHO-TRIPLtee Branch
Arnold Research Organization
Ames Div.
Moffett Field, Calif. 94035

Mr. G. Warnecke
NASA/GSFC, Code 622
Greenbelt, Md. 20771

Mr. I. Katz
Applied Physics Lab.
Johns Hopkins Univ.
Silver Spring, Md. 21218

Mr. J. D. Rogers
Univ. of Calif.
Los Alamos Sci. Lab.
P. O. Box 1663
Los Alamos, N. M. 87544

Mr. J. Stackpole
NMC Weather Bureau
Washington, D. C. 20546

Mr. Louis Galbiati
Mitre Corp.
Bedford, Mass. 01730

Mr. J. F. King
GCA Corp.
Bedford, Mass. 01730

EXTERNAL DISTRIBUTION (Continued)

Mr. E. R. Walker
Frozen Sci. Res. Group
Dept. of Energy, Mines & Resources
825 Devonshire Road
Esquismalt, B. C., Canada

Dr. Philip S. Kelbonoff
U. S. Dept. of Commerce
National Bureau of Standards
Washington, D. C. 20234

Prof. H. B. Nottage
Univ. of Calif.
Dept. of Engr.
405 Hilgard Ave.
Los Angeles, Calif. 90024

Mr. Wilbur Paulsen
Air Force Cambridge Res. Lab.
L. G. Hanscom Field
Bedford, Mass. 01730

Dr. R. B. Gray
Ga. Inst. of Tech.
School of Aerospace Engr.
Atlanta, Ga.

E. Summerscales
Mech. Engr. Dept.
Rensselaer Polytechnic Inst.
Troy, New York 12181

Dr. R. M. White, Adm.
Environmental Sci. Services Adm.
Washington Science Center
Rockville, Md. 20852

Prof. J. R. Weske
Univ. of Md.
College Park, Md. 20746

National Environ. Satellite Center
Federal Ofc. Bldg. No. 4
Suitland, Md. 20852
Attn: Dr. David S. Johnson, Dir.
Dr. J. P. Kuettner

M. V. Morkovin
1104 Linden Ave.
Oak Park, Ill. 60302

Dr. Lester Machta, Act. Dir.
Inst. for Atmos. Sci.
Boulder, Colorado 80302

Prof. Stanley Corrsin
Dept. of Mech.
Johns Hopkins Univ.
Charles and 34th St.
Baltimore, Md. 21218

Mr. H. K. Weiekmann
National Physics and Chem. Lab.
Boulder, Colorado 80302

Prof. L. S. G. Kovaszny
Dept. of Mech.
Johns Hopkins Univ.
Charles and 34th St.
Baltimore, Md. 21218

Mr. B. Horn
National Center for Atmospheric Res.
Facilities Div.
Boulder, Colorado 80302

Dr. Carl H. Gibson
Univ. of San Diego
Alcala Park
San Diego, Calif. 92110

Dr. James H. Leonard, Dir.
Nuclear Sci. & Engr.
Univ. of Cincinnati
Cincinnati, Ohio 45221

William J. Yanta
U. S. Naval Ordnance Lab.
Bldg. 90, Rm. 201G
Silver Springs, Md. 20901

EXTERNAL DISTRIBUTION (Continued)

Mr. David L. Brott
U. S. Naval Ordnance Lab.
Bldg. 90, Rm. 201G
Silver Springs, Md. 20901

Dr. S. Kavipurapu
Dept. of Nuclear Engr.
Univ. of Cincinnati
Cincinnati, Ohio 4522

Langley Res. Center
Hampton, Va. 23365
Attn: S. L. Seaton, Mail Stop 235
A. C. Holup, Mail Stop 235
Mr. Fedziuk, Mail Stop 117
Mr. Boswinkle, Mail Stop 117
Mr. Bertram, Mail Stop 130
Mr. Hubbard, Mail Stop 239
Mr. Runyan, Mail Stop 242
Mr. Donely, Mail Stop 246

Univ. of Alabama
Res. Inst.
Attn: Dr. R. Hermann
Dr. Shi

Smithsonian Inst. Astro. Observatory
Cambridge, Mass.
Attn: Dr. Charles Lundquist

U. S. Army Missile Command
Redstone Arsenal
Attn: O. M. Essenwanger, R&D
S. H. Lehnigk, R&D
B. Steverding, R&D

Colorado State Univ.
Ft. Collins, Colorado
Dept. Atmos. Service
Attn: E. R. Reiter
W. R. Green
Dept. Civil Engr.
V. H. Sandborn
Dept. Math. & Statistics
M. M. Siddigui

University of South Hampton S09 5NH
South Hampton, England
Attn: Prof. M. J. Fisher
Prof. P. O. A. L. Davies
Inst. of Sound and
Vibration Research

Prof. H. Ribner
University of Toronto
Toronto, Canada

Prof. J. E. Ffouics Williams
Dept. of Math.
Prince Consort Rd. (Exhibition Rd)
Imperial College
London S. W. 7, England

Dr. Kurzweg
Director Research Div.
NASA Hdqs. Code RR
Washington, D. C. 20546

Dr. B. H. Goethert
University of Tenn. Space Inst.
Tullahoma, Tenn.

Prof. Wallace D. Hayes
Princeton University
Princeton, N. J.

Dr. L. H. Caveney
Ferrestal Campus
Princeton University
Princeton, N. J.

Dr. Lester Lees
Princeton Univ.
Princeton, N. J.

Dr. W. C. Meechem
Univ. of Calif.
LaJolla, Calif. 92038

EXTERNAL DISTRIBUTION (Continued)

Dr. Ben Zins
Dept. of Aerospace Engineering
The Georgia Inst. of Tech.
Atlanta, Ga.

Dr. H. Plumblee
Lockheed Georgia Co.
Marietta, Georgia

Dr. P. J. Westernelt
Brown Univ.
Providence, Rhode Island

Dr. Martin Summerfield
Princeton Univ.
Princeton, N. J.

Dr. Hans Liepmann
Calif. Inst. of Tech.
4800 Oak Grove Dr.
Pasadena, Calif. 91103